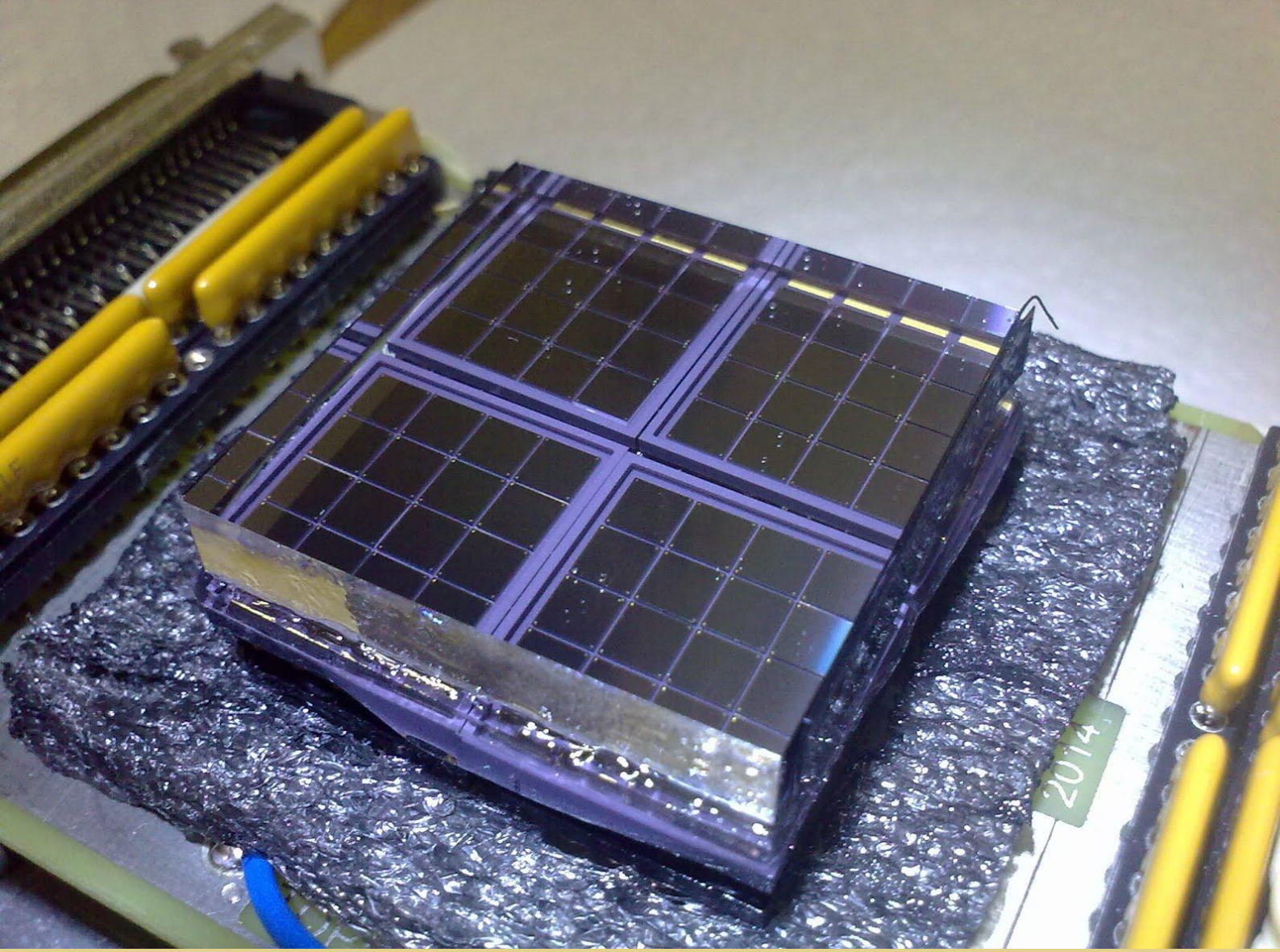


Raimundo Miguel Oliveira Martins

# Optimization of a Compact Medical Gamma Camera

Thesis submitted to the Physics Department at University of Coimbra to obtain the Master's degree in Physics

July 2016


UNIVERSIDADE DE COIMBRA

• U C •

FCTUC FACULDADE DE CIÊNCIAS
E TECNOLOGIA
UNIVERSIDADE DE COIMBRA

Raimundo Miguel Oliveira Martins

# Optimization of a compact medical gamma camera

Thesis submitted to

University of Coimbra

in the fulfillment of the requirements for the degree of

Master of Science
in Physics

Supervised by:
PhD Andrey Morozov
PhD Vladimir Solovov

July 2016

# Abstract

A detailed model of a compact gamma camera for applications in small animal SPECT has been developed using the ANTS2 simulation package. The predictive power of this model was demonstrated by comparing the simulated and experimentally determined light response functions (LRFs) of the prototype of the camera, which demonstrated remarkable similarity. Additionally, the validity of the model was confirmed by a very accurate reconstruction of the experimental event positions using the LRFs calculated from the simulated data.

An optimization study was performed on the lightguide thickness for several configurations. It was shown that the optimal configuration of the detector has a diffuse reflector coupled to the back plane of the scintillator. It was also shown that it is beneficial to cover the side walls of the scintillator and the lightguide with an optical grease and a light absorbing layer. For this configuration, the optimal thickness of the lightguide was found to be 0.5 mm. The optimized camera spatial resolution was shown to be close to 0.5 mm, the maximum position reconstruction bias of 0.5 mm and the useful field of view of 28 mm × 28 mm (87 % of the crystal area).

# Resumo

Foi desenvolvido um modelo detalhado duma câmera gama compacta, para uso em SPECT para pequenos animais, através do uso do pacote de simulações ANTS2. O poder preditivo deste modelo foi demonstrado, comparando as funções de resposta de luz (LRF) simuladas e as determinadas experimentalmente, que mostraram uma semelhança notável. Mais ainda, a validade do modelo foi confirmada por uma reconstrução muito precisa das posições dos eventos experimentais, usando as LRFs calculadas através das simulações.

Um estudo de otimização foi realizado sobre a espessura do guia de luz para várias configurações. Mostrou-se que a configuração ótima do detetor tem um refletor difuso acoplado ao plano inferior do cintilador. Também se mostrou que é benéfico cobrir os lados do cintilador e do guia de luz com óleo para acoplamento ótico, e uma camada que absorve luz. Para esta configuração, a espessura ótima do guia de luz encontrada foi 0.5 mm. A resolução espacial da câmera gama otimizada está próxima de 0.5 mm, e o campo de visão útil é de 28 mm × 28 mm (87 % da área do cristal).

# Acknowledgements

First, a very special thanks to my advisors Doctor Andrey Morozov and Doctor Vladimir Solovov, for always believing in me and my work, which was a source of great inspiration and motivation; for making me (not just feel, but to actually be) a part of the team; for the wisdom of senior researchers, transmitted with benevolence; and especially for the insights, tolerance, and support during my (lengthy) learning process of the writing of a dissertation, which, I believe, have gone far beyond what most advisors would be willing to sacrifice, in both time and effort. You have my deepest gratitude, for your friendship, and for being someone I can rely on, in this new academic world!

I would also like to thank LIP-Coimbra for introducing me to this work group, and for providing the materials for the experimental part of this study.

Many thanks to all my friends from Coimbra, especially Henrique Miranda, Marco Pinto, Gonçalo da Cruz, Afonso Sousa, Johnny Araújo, Joana Pestana, Andreia Galiano, Rafaela Carvalho, and my house mates at "nº 10 da Padre António Vieira".

I must also thank my parents, for without their love care and support throughout my entire life, this work would have never been achieved.

Finally, I would like to thank my other half, Carla Duarte. Thank you for everything you've been to me, and for making me a better person. For your love, affection, sweetness and kindness, even when I am being the most difficult person on Earth. I hope it lasts for the rest of our lives.

# Contents

# List of Figures

# List of Tables

# Chapter 1

# Introduction

## 1.1 Gamma cameras in molecular imaging

There are several diagnostic techniques in nuclear medicine, the main ones being scintigraphy, SPECT and PET. In scintigraphy, two-dimensional projections are recorded using gamma cameras. SPECT (single-photon emission computed tomography) is a three-dimensional tomographic technique that uses projections recorded by a gamma camera from different angles. PET (positron emission tomography) uses a coincidence detection technique to reconstruct the 3D density map of the radiopharmaceutical density. Gamma cameras are less expensive than PET, because they do not need to locally produce the radionuclides (in PET these typically have a very short half-life time), and consequently the radiopharmaceuticals. They can also use wider range of radiotracers.

Compared to the morphological imaging techniques, such as CAT (computer assisted tomography) and nuclear MRI (magnetic resonance imaging), the molecular imaging is functional, i.e. it shows functional activity of the body organs. Therefore, it can be used for diagnostic purposes, looking for lack of normal activity, or traces of abnormal activity. For instance, in cancer diagnostics, the radiotracer is typically a sugar. Since cancer cells multiply rapidly, and have a higher metabolic rate, they consume much more energy than normal cells. Such energy is in the form of sugar, and so the radionuclide becomes more concentrated on the cancer cells. It can be also used in drug discovery.

Small animals, especially mice, play a crucial role as test subjects in drug development. Before a new pharmaceutical reaches the stage of human trials, an extended study must be performed to verify its metabolic pathways, organ uptake and elimination, toxicity and long term effects. Recent advances in molecular imaging techniques allow to study migration of the drug through the animal body, verifying if it reaches the target organ in sufficient concentration, and whether it reaches undesirable sites where it can produce toxic effects. Also, detailed information on the dynamics of the pharmaceutical uptake and elimination can be obtained.

While gamma cameras are mostly used in drug development and nuclear medical imaging, there are other areas of use which also benefit from advancements in the gamma camera technology. For example, contamination visualization in radioactive cleanup operations (including deactivation of nuclear reactors), non-invasive container scanning of radioactive materials, industry (see [17] for a case study of the dynamics of slurry transport), and academic research (see [7] for gamma imaging of $^{99m}$Tc transport for radioactive waste disposal).

In a SPECT system, a rotating position sensitive gamma-ray detector coupled to a collimator is used to take several projections at different angles from which 3D distribution of the radiotracer in the test subject is reconstructed. In small

animal SPECT, due to the size of the test subjects, high spatial resolution (better than 1 mm) is required for both the detector and the collimator. Such a high-resolution detector is currently under development jointly by the Biomedical Applications Group of LIP-Coimbra and the Physics Department of the University of Coimbra with promising results. This master studies constitutes an important part of this development.

## 1.2 Objectives and methods

The research group for which I have performed my master studies is developing a compact gamma camera suitable for pre-clinical and clinical applications, such as small animal imaging and radioisotope guided surgery. These applications impose a set of requirements on the camera performance: the camera should have sub-millimeter spatial resolution and a low level of image distortions. These properties strongly depend on the geometry and design of the camera. While the general design of the camera has already been fixed, several features which can significantly affect the performance of the camera still had to be optimized.

In this study my task was to optimize the lightguide thickness and to define whether the following two options are beneficial: to use a reflector coupled to the back plane of the scintillator and to apply optical grease and light absorption layers on the side walls of the scintillator and the lightguide to reduce light reflections from these walls.

The optimization was performed using Monte Carlo simulations. For this, a model of the camera was created using the ANTS2 software package developed in the group. The model was successfully validated by comparing simulation results with those obtained experimentally with a prototype of the gamma camera. Then a set of simulations was performed for all design options which had to be investigated. The results were compared and the configuration resulting in the best combination of the camera performance parameters was selected.

In order to speed up the search for the best design, I developed multi-threading capabilities for the simulation module of the ANTS2 package. Moreover, in order to ensure consistency of the tests done with multiple designs, avoid performing multiple similar tasks, allow for easy reproducibility, and allow for easy adaptation of this study to different camera designs, I have also developed the first scripting tools in ANTS2, along with the necessary scripts to perform all the simulations required for this study. Furthermore, to ensure consistency of the analysed data, a small custom software package was developed to generate, from the results of the simulations, the tables and the graphs presented in this work. This package can easily be embedded in the ANTS2 scripting tools, if deemed necessary. With these developments,

and without taking into account the time required for the experimental validation, this study can now be performed in less than 24 h, on a high-end consumer grade computer. Finally, I have also developed graphical analysis tools for ANTS2, and improved the usability of the LRF module by adding support to LRF history and its navigation.

For the experimental part of this work, I have developed LULAS, the data acquisition software, which features: configuration of the MAROC3 frontend electronics board, automatic gain equalization optimized for uniformity, and data acquisition and visualization.

During the course of this work I have also contributed to three related publications: [20], [21], and [24].

## 1.3 Thesis structure

In this section, a short description of each chapter of this thesis is provided:

**Chapter 1** is this introductory chapter.

**Chapter 2** briefly describes the physical phenomena relevant for the operation of gamma cameras.

**Chapter 3** gives an overview of the operation and general design of a gamma camera. A summary of the most important properties of each of the gamma camera components is presented. Also, a description is given of two of the most broadly used image reconstruction techniques.

**Chapter 4** provides a description of ANTS2, the software package used to perform Monte Carlo simulations and reconstruct experimental events.

**Chapter 5** describes the gamma camera prototype. It also provides details on the simulation model and describes the model validation using experimental data.

**Chapter 6** contains the results of the simulations, used in camera optimizations. It also presents the discussion of the results leading to selection of the optimal configuration of the camera.

**Chapter 7** contains a short summary of what was achieved in this study and summarizes my other contributions to the work conducted by the group.

Chapter 2

# Physics of a gamma camera

## 2.1 Gamma radiation

Gamma radiation is composed of high energy photons which are typically emitted as a product of nuclear decays, or pair annihilation. Gamma radiation used in nuclear medicine is typically in the range of 50 keV to 1 MeV, as it can travel across human tissue with low interaction probability while not creating excessive background due to multiple scattering and pair production.

### 2.1.1 Production

Atomic nuclei have well-defined quantized energy states. Transitions from higher to lower energy states result in the emission of electromagnetic radiation with an energy equal to the difference between the energy of the involved states. Since nucleons have a high bonding energy, their transitions involve energy levels anywhere from a few tens of keV to several MeV. Gamma particles are emitted as a result of a transition from a higher energy excited state to either a lower energy excited state or the ground state. Typically, these states are populated as a by-product of nuclear reactions, such as fission, fusion, electronic capture, and $\alpha$, $\beta^-$ or $\beta^+$ decays.

After the nuclear reaction, the excited nucleus usually has a very short half-life time, of the order of ps. However, for some isotopes certain transitions are "forbidden", usually because they involve a large change in the nuclear spin. Such excited states are called metastable states, and can have a long half-life time. For instance, the $^{99m}$Tc isotope has a half-life of 6 hours.

### 2.1.2 Interaction with matter

When gamma radiation passes through matter, it transfers energy due to different interaction processes. The parallel beam flux attenuation is given by the Beer-Lambert law. For uniform attenuation, it can be expressed as:

$$I(x) = I_0 e^{-\mu x} \tag{2.1}$$

where $I_0$ is the initial beam flux, $x$ is the distance, and $\mu$ is the attenuation coefficient.

In the photoelectric effect, a gamma particle transfers all of its energy to an atomic electron, ejecting it from the atom with a kinetic energy equal to $E = h\nu - E_b$, where $h\nu$ is the gamma particle energy and $E_b$ is the electron binding energy. Typically, it is the dominant process for energies under 100 keV. An approximation of its cross section is given by [8]:

$$\sigma = k\frac{Z^n}{(h\nu)^3} \tag{2.2}$$

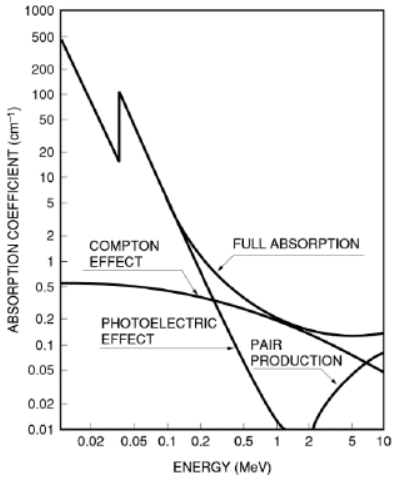


Figure 2.1: NaI(Ti) absorption coefficients, for gamma particles up to 10 MeV.

where $k$ is a constant, $Z$ is the atomic number, and $n$ has a value in the range between 4 and 5. This shows that materials with higher $Z$ have a higher cross section. See [26] for tables of photoelectric cross sections.

In Compton scattering, a gamma particle transfers a part of its energy to an atomic electron, ejecting it, and then changing direction. Typically, it is the dominant effect for energies between 100 keV and 10 MeV. The energy transferred to the electron corresponds to the wavelength shift of the gamma particle:

$$\lambda' - \lambda = \frac{h}{m_e c}(1 - \cos\theta) \tag{2.3}$$

where $\lambda = c/\nu$ is the initial wavelength, $h$ is Planck's constant, $m_e$ is the mass of the electron, $c$ is the speed of light in vacuum, and $\theta$ is the scattering angle of the gamma particle.

The differential cross-section, per electron, of the Compton scattering is given by the Klein-Nishina formula [16]:

$$\frac{d\sigma}{d\Omega} = \frac{1}{2}\left(\frac{\alpha h}{m_e c}\right)\frac{1}{[1+\gamma(1-\cos\theta)]^2}\left(1+\cos^2\theta+\frac{\gamma^2(1-\cos\theta)^2}{1+\gamma(1-\cos\theta)}\right) \tag{2.4}$$

where $\alpha$ is the fine-structure constant ($\approx 1/137$), and $\gamma = h\nu/m_e c^2$.

In pair production, a gamma particle is converted into an electron-positron pair with total kinetic energy of $K = E_\gamma - 2m_e$ in the strong electric field of the atomic nucleus. This means that the interaction is only possible with energies above $2m_e \approx 1.02$ MeV. Thus, this process is irrelevant for the gamma camera operation and is not discussed here.

## 2.2 Scintillation process

After a gamma particle deposits some energy in the scintillator, by means of photoelectric effect or Compton scattering, a high energy electron is ejected. Such electron excites and ionizes multiple atoms (or molecules) along its trajectory. When returning to the ground state, the atoms emit optical photons. This process is called scintillation, and a brief discussion on its properties, relevant to the gamma camera operation, is given in this section.

Light yield is the amount of photons produced by unit energy deposited in the scintillator, by the incident gamma particle, and is one of the most important parameters as it determines the amount of light produced by a detected gamma particle. This, in turn, determines statistical fluctuations in the recorded signal and consequently spatial and energy resolution of the detector. For this reason, the scintillators used in nuclear medicine (NaI(Tl), BGO, LSO) tend to have relatively high light yield, of the order of several tens of photons per keV of deposited energy.

Decay time characterizes the decay rate of the excited atoms. Assuming exponential decay, $N = N_0 \exp \lambda t$, decay time is the exponential time constant, $\lambda$. For the most commonly used scintillation materials, the decay time is between several tens of nanoseconds to several microseconds.

Another important characteristic of the scintillator is the emission spectrum. For practical reasons, for a gamma camera, it is preferable to have a scintillator with a narrow (in the order of tens of nanometers) emission in the visible range to effectively match the emission with the sensitivity range of high sensitivity photosensors, such as PMTs (photomultiplier tubes), or SiPMs (silicon photomultipliers).

Finally, the scintillator is also characterized by its intrinsic energy resolution, which describes the fluctuations in the number of photons for a fixed amount of deposited energy. It is typically given as the ratio between the FWHM of the number of emitted photons and the average number of emitted photons, and ranges from several percent to a few tens of percent.

## 2.3 Light propagation

Photons emitted by the scintillator propagate through the detector. When they reach the photosensors a fraction of them are detected, and from the set of signals of all photosensors, the event position can be calculated. In this section, the physical processes on the interface of two media is described

As figure 2.2 suggests, refractive indices for the first and second media are, respectively, $n_i$ and $n_t$. For convenience, $n_{it} = n_i/n_t$ is also defined. $\hat{k_i}$, $\hat{k_t}$, and $\hat{k_r}$ are, respectively, the incident, trasmitted, and reflected light direction vectors,

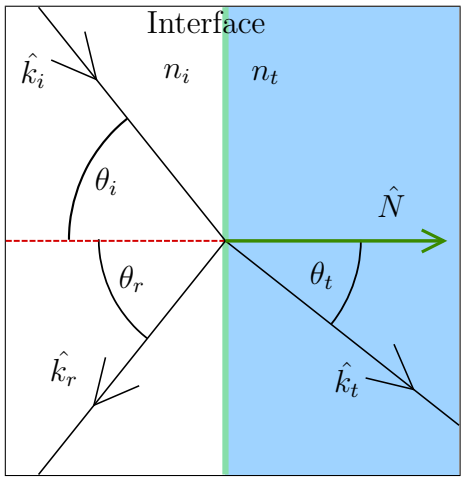


Figure 2.2: Light refraction.

all of them normalized to unity. $\hat{N}$ is the normal of the interface between the two media, at the position where the ray of light intersects it. By definition, $\hat{N}$ always points from the first to the second medium. $\theta_i$ is the angle between $\hat{k}_i$ and $\hat{N}$, and analogously with $\theta_t$ and $\theta_r$, so that

$$\cos\theta_i = \hat{N} \cdot \hat{k}_i \tag{2.5}$$

$$\cos\theta_t = \hat{N} \cdot \hat{k}_t \tag{2.6}$$

$$\cos\theta_r = \hat{N} \cdot \hat{k}_r \tag{2.7}$$

### 2.3.1 Fresnel equations

When a ray of light encounters an interface between two media with different refractive indices, it can be reflected or transmitted (refracted) to the next medium. The probability of reflection can be determined using the Fresnel equations. Assuming linear, isotropic, homogeneous, dielectric media, and unpolarized light, the probability of reflection $R$ is:

$$R = \frac{R_\perp + R_\parallel}{2} \tag{2.8}$$

where $R_\perp$ and $R_\parallel$ are the perpendicular and parallel components of polarized light (see [13], section 4.6) respectively, given by:

$$R_\perp = \left| \frac{n_i \cos\theta_i - n_t \cos\theta_t}{n_i \cos\theta_i + n_t \cos\theta_t} \right|^2 \tag{2.9}$$

$$R_\parallel = \left| \frac{n_i \cos\theta_t - n_t \cos\theta_i}{n_i \cos\theta_t + n_t \cos\theta_i} \right|^2 \tag{2.10}$$

The probability of transmission is simply $T = 1 - R$.

### 2.3.2 Refraction

When a ray of light is trasmitted to a medium with a different refractive index, its direction changes. This change is described by Snell's law (see [13], section 4.4), and can be written as

$$\sin\theta_t = n_{it}\sin\theta_i = n_{it}\sqrt{1-\left(\hat{N}\cdot\hat{k}_i\right)^2} \tag{2.11}$$

which leads to

$$\cos\theta_t = \sqrt{1-n_{it}^2\left(1-\left(\hat{N}\cdot\hat{k}_i\right)^2\right)} \tag{2.12}$$

and so, the reflected and refracted direction vectors of light are, respectively, given by (see [13], sections 4.3 and 4.4):

$$\hat{k_r} = \hat{k} - 2\cos\theta_i\hat{N} \tag{2.13}$$

$$= \hat{k} - 2\left(\hat{N}\cdot\hat{k}_i\right)\hat{N} \tag{2.14}$$

$$\hat{k_t} = n_{it}\hat{k} - \left(n_{it}\cos\theta_i - \cos\theta_t\right)\hat{N} \tag{2.15}$$

$$= n_{it}\hat{k} - \left(n_{it}\hat{N}\cdot\hat{k}_i - \sqrt{1-n_{it}^2\left(1-\left(\hat{N}\cdot\hat{k}_i\right)^2\right)}\right)\hat{N} \tag{2.16}$$

### 2.3.3 Total internal reflection

When light travels to a medium with a lower refractive index ($n_{it} > 1$), it is possible that at some incident angles solutions to eq. 2.11 require that $\sin\theta_i > 1$. Alternatively, when

$$n_{it}^2\left(1-\left(\hat{N}\cdot\hat{k}_i\right)^2\right) > 1 \tag{2.17}$$

eq. 2.12 contains a negative square root, which has no physical meaning. The critical angle is the largest incidence angle to which eq. 2.11 has a valid solution, and can be written as

$$\theta_{crit} = \arcsin\left(\frac{n_t}{n_i}\right) \tag{2.18}$$

At this incident angle, the direction of light is perpendicular to the normal of the interface. When $\theta_i > \theta_{crit}$, total internal reflection takes place, and all incident light is reflected.

### 2.3.4 Diffuse reflection

Diffuse reflection occurs when light is reflected on irregular surfaces, due to multiple reflections, possibly in the first few layers of the material. A very good approximation

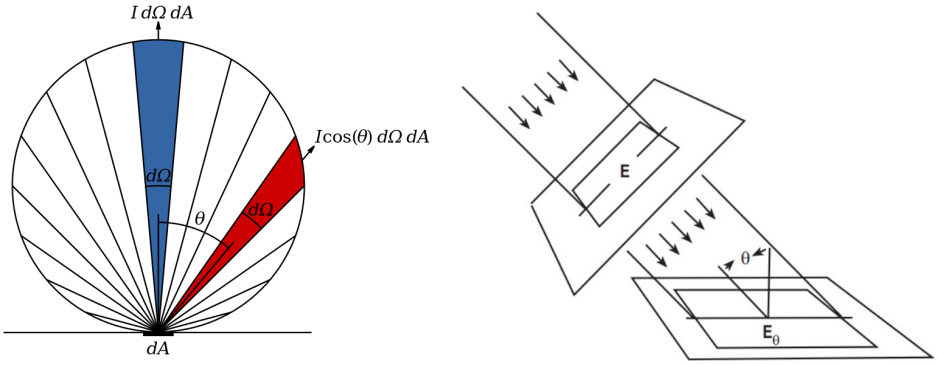


Figure 2.3: **Left**: The emission rate of a Lambertian surface. **Right**: Apparent area of a surface viewed from an angle $\theta$.

for this phenomenon is Lambert's law, which states that a photon scattering from such surface has the probability to be emitted at an angle $\theta$ proportional to $\cos\theta$:

$$\hat{k}_t = \cos\theta \hat{k}_i = \hat{N} \cdot \hat{k}_i \hat{k}_i \tag{2.19}$$

It should be noted that, even though the re-emission probability depends on the angle, so is the apparent surface area $E$ dependent on the source surface area $E_0$ by the same factor (see figure 2.3):

$$E = E_0 \cos\theta \tag{2.20}$$

The end result is that the perceived light flux is independent of the angle of observation.

Chapter 3

# Principles of the gamma camera operation

## 3.1 Design of a Gamma camera

A gamma camera is a device which images gamma radiation sources. It is mostly used in drug development and nuclear medical imaging, by allowing to view the distribution of gamma-emitting radionuclides.

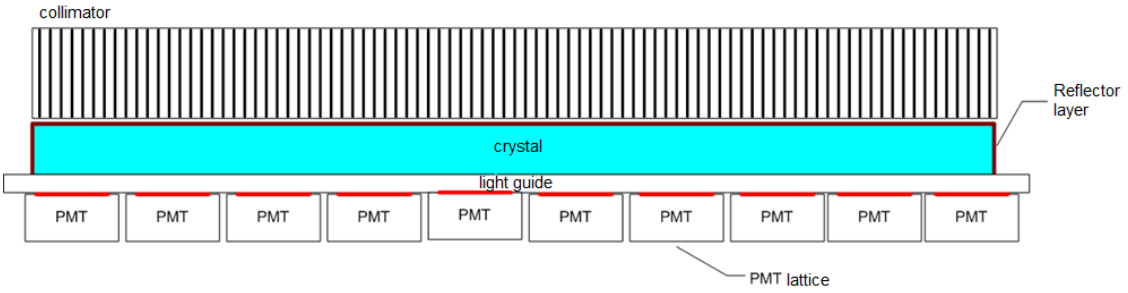


Figure 3.1: Schematic design of a gamma camera.

Gamma cameras reconstruct the position and energy of the interactions of non-simultaneous and independent gamma particles with the camera. First, the collimator projects the gamma activity distribution on the scintillator plane. Then, the gamma particles interact with the camera scintillator producing optical photons. Afterwards, these photons are detected by a set of photosensors (e.g. PMTs) and produce electronic response signals. Finally, the signals are processed, and the final image is a density map of the reconstructed positions of the events.

### 3.1.1 Collimator

Before reaching the scintillator, gamma particles from the radioactive source must be collimated, so that the source image is projected onto the camera. A collimator is the first part of a gamma camera to interact with gamma particles. It imposes an acceptance angle for the gamma particles that reach the scintillator, but it also reduces the overall efficiency of the detector.

When a gamma particle reaches the collimator (see figure 3.2) it can: a) pass through it, leading to a scintillation event well correlated with the source image; b) be blocked by the septa (and not result in a detected event); c) penetrate the septa, a case in which the collimator was not effective, leading to an incorrect calculation of the source position.

The collimator performance can be characterized by four parameters:

**Resolution:** it is described by the FWHM of the projected radiation profile of a point source. For parallel-hole collimators (see below), it increases linearly with the distance between the source and the collimator.

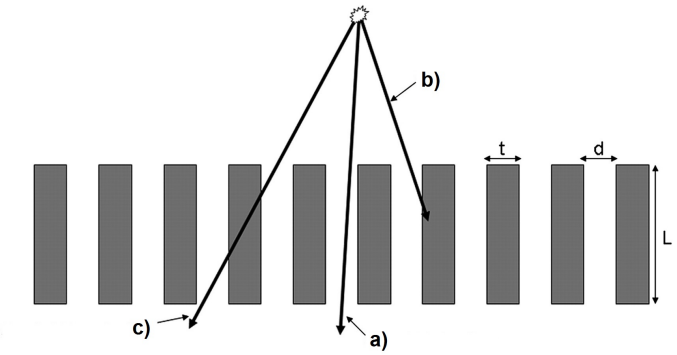


Figure 3.2: Example of a parallel-hole collimator, with a $t$ septal thickness, a $d$ septal separation, and an $L$ collimator thickness. When a gamma particle reaches the collimator it can **a)** pass through it **b)** be blocked by the septa **c)** penetrate the septa.

**Sensitivity:** it is the fraction of gamma particles emitted by the source that pass through the collimator. It is proportional to the fraction of collimator surface not occupied by the septa, and inversely proportional to the thickness of the collimator.

**Septal penetration probability:** it decreases with the increase of septal thickness.

**Field of view:** it is the area that is projected onto the camera.

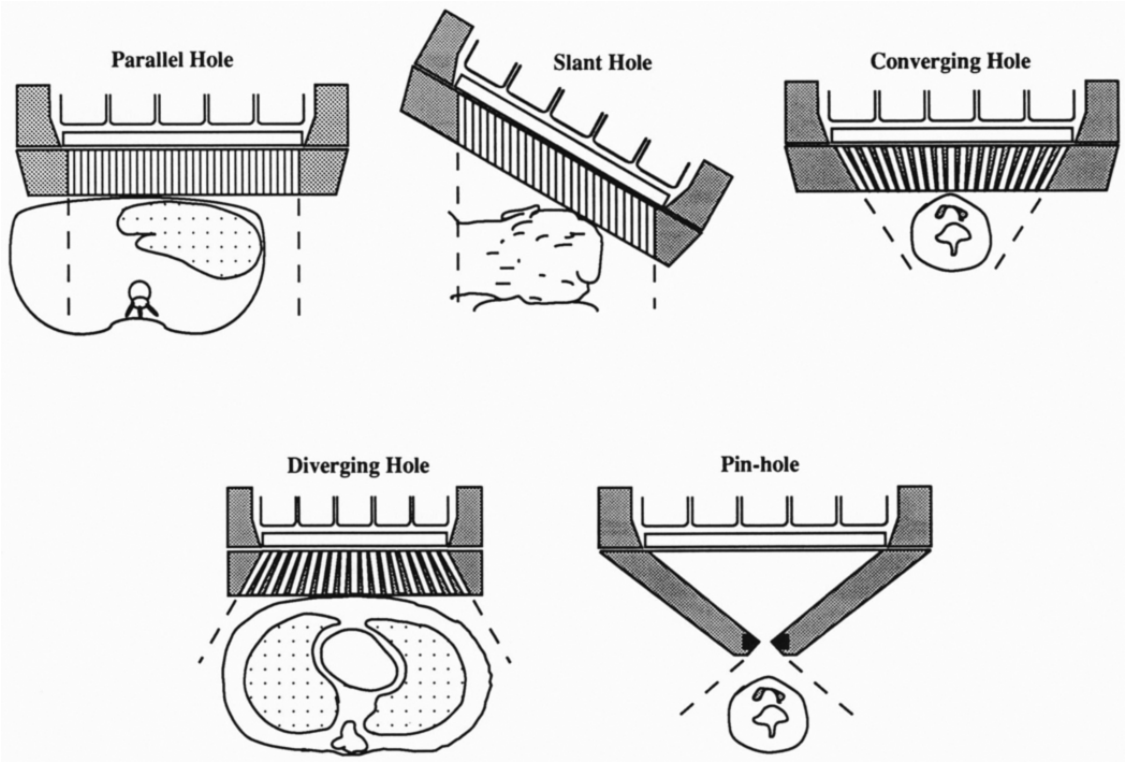


Figure 3.3: Collimators commonly used in gamma cameras. See also [28].

There are five types of collimators used in gamma cameras (see figure 3.3), classified by the type of focusing:

**Parallel-hole collimators:** they are the most commonly used collimators, and have little distortion compared to other collimators.

**Parallel slant-hole collimators:** they were initially used for limited angle tomography. These are useful to position the camera closer to the organ being studied when part of the body impedes the usage of parallel-hole collimators, e.g. when imaging the brain while avoiding the shoulders. Although sensitivity is higher than in parallel-hole collimators, it presents linear distortions on the tilted dimension.

**Converging collimators:** they are used to magnify the organ image.

**Diverging collimators:** they are used to increase the camera field of view, e.g. in full-body scans.

**Pinhole collimators:** they contain a single small aperture, and are used mostly for imaging small organs, like the thyroid. Images taken with pinhole collimators have much lower sensitivity, much higher resolution, and much more distortions than those of multi-hole collimators. As the pinhole gets smaller, image resolution increases and sensitivity decreases. The same pinhole collimator can also be used at higher energies without significant increase in septal penetration, as opposed to multi-hole collimators.

### 3.1.2 Scintillator

The scintillator (see [15], chapter 8) converts part of the energy of gamma particles into optical photons, whose amount is measured by photosensors. Its main properties are:

**Light yield:** Photosensors register the amount of incident photons, and so, the higher the yield, the smaller the relative statistical fluctuations, and, potentially, the better the spatial and energy reconstruction of the detector.

**Decay time:** The shorter the decay time, the higher the maximum possible event acquisition rate, and, potentially, the better the signal to noise ratio.

**Emission spectrum:** It is the wavelength spectrum of the photons emitted by the scintillator. It should be narrow, as photomultipliers typically have a limited wavelength range of detection.

| Material | Density ($g\,cm^{-3}$) | $\lambda_{max}$ (nm) | Refractive index | Decay time (ns) | Light yield ($keV^{-1}$) |
|---|---|---|---|---|---|
| NaI(Tl) | 3.67 | 415 | 1.85 | 230 | 38 |
| CsI(Tl) | 4.51 | 540 | 1.80 | 800 | 60 |
| BGO ($Bi_4Ge_3O_{12}$) | 7.13 | 480 | 2.15 | 300 | 8.2 |
| $LaBr_3$(Ce) | 3.79 | 350 | 1.9 | 27 | 49 |
| LSO ($Lu_2SiO_5$(Ce)) | 7.4 | 420 | 1.82 | 40 | 27 |
| LYSO | 7.4 | 420 | 1.81 | 40 | 32 |

Table 3.1: Examples of some widely used inorganic scintillators.

**Energy resolution:** The higher it is, the more efficient is the discrimination of background events. See also [22].

**Refractive index:** Typically, lightguide and photosensor window materials have a refractive index of ≈1.5. In order to minimize reflections on the material interfaces, the closer the refractive index of the scintillator is to this value, the better.

**Detection efficiency:** It is the fraction of incoming gamma particles that deposit energy in the scintillator. Detection efficiency is related to the material density, and the atomic numbers of the element composition of the scintillator, and increases with the thickness of the scintillator. However, the scintillator cannot be arbitrarily thick, as that would reduce the spatial and energy resolutions of the camera (see discussion on the effects of a thick lightguide in section 3.1.3).

Table 3.1 lists some inorganic scintillators, often used in gamma cameras. Inorganic scintillators are widely used for medical imaging, due to their high density and high atomic number (resulting in a high attenuation coefficient), as well as their high light yield.

Thallium-doped sodium iodide is the most widely used scintillator, even though it is very hygroscopic and needs to be encased in an air-tight enclosure. Bismuth germanate is not hygroscopic, and has a higher attenuation coefficient than sodium iodide, but it also has a much lower light yield. Lutetium-Yttrium Silicon Oxide (LYSO) is also non-hygroscopic, has a high attenuation coefficient, a short decay time, and high light output. As a downside, it has intrinsic background radiation due to the $\beta^-$ decay of natural $^{176}$Lu.

### 3.1.3 Lightguide

A lightguide is a slab of non-scintillating transparent material, placed between the scintillator and the photosensors, whose main function is to spread scintillation light.

A gamma camera is not required to have a lightguide to operate, but by distributing the light emitted by the scintillator over a larger number of photosensors, it typically improves spatial resolution and decreases distortions of the reconstructed images.

Ideally, the refractive index of the lightguide should be the mean value of the refractive indices of the scintillator and the entrance window of the photosensors, in order to minimize reflections (similar considerations can be applied to the choice of optical grease). Consider a beam of light, parallel to the normal of such interface. With the insertion of a third medium, the total reflection probability $R_{total}$ (see section 2.3.1) is:

$$R_{total} = \left( \frac{x(n_i - n_t)}{n_i + n_t - (1-x)(n_i - n_t)} \right)^2 + \left( \frac{(1-x)(n_i - n_t)}{n_i + n_t - x(n_i - n_t)} \right)^2 \tag{3.1}$$

where $x(n_i - n_t) + n_t$ is the refractive index of the third medium, and $x$ is between 0 and 1. In order to minimize reflections, one must solve:

$$\frac{dR_{total}}{dx} = 0 \tag{3.2}$$

For $-5n_t < n_i < 3n_t$ (this is well within the typical regime of gamma cameras), the solution is $x = 1/2$, which means that the refractive index of the third medium should be $(n_i - n_t)/2 + n_t = (n_i + n_t)/2$, half of the refractive index of the other two media. With this, the total reflection probability is:

$$R_{total} = 2 \left( \frac{n_i - n_t}{n_i + 3n_t} \right)^2 = 2 \left( \frac{n_i + n_t}{n_i + 3n_t} \right)^2 R \tag{3.3}$$

### 3.1.4 Photodetection

A fraction of the scintillation photons, after crossing the scintillator and lightguide, reach the photosensors. A low number of photons emitted per event (e.g. ≈1000, see [20]) requires photosensors with a very high signal to noise ratio. Therefore, the photosensor needs to have a high internal gain.

Typically, photosensors found in gamma cameras are PMTs or SiPMs. However some applications (like compact gamma cameras) benefit from SiPMs, due to their low-voltage, compactness, and indifference to magnetic fields.

For gamma cameras, the most relevant properties of the photosensor are:

**Gain:** it is the signal amplification factor for a single photoelectron. In order to optimize signal to noise ratio, this value should be an order of magnitude higher than the input noise of the electronic processing chain (typically $10^4$ to $10^5$ electrons r.m.s). PMTs and SiPMs with gains in the range of $10^5$ and $10^7$ are particularly suitable for gamma camera applications.

**Photodetection efficiency:** it is the probability that an incident photon triggers the photosensor signal output. It depends on several parameters such as the incident photon wavelength, position and angle, the power source voltage, and the temperature. When choosing a photosensor for a given scintillator, one should to maximize $\int_\lambda S_{emi}(\lambda)P_{det}(\lambda)d\lambda$, where $S_{emi}(\lambda)$ is the scintillator emission spectrum, $P_{det}(\lambda)$ is the photosensor detection efficiency, and $\lambda$ is the wavelength of the emitted photon.

**Dark current:** it is the sensor output signal without any input light, due to the thermal emission of photoelectrons (for PMTs) or due to the thermal production of electron-hole pairs (for SiPMs). Typically, it depends on temperature and power source voltage. For SiPMs, the equivalent property is the dark count rate.

### 3.1.5 Electronics

The electrical signals of the photodetectors need to be processed, in order to reconstruct the position and energy of the scintillation event. Frontend electronics amplify and filter the output signal of the photosensors in order to maximize signal-to-noise ratio. The trigger circuit provides the start signal to the data acquisition system when the signal in one or several channels rise above a predefined threshold. The data acquisition system digitizes the signals and transfers them to a computer, which performs the scintillation event position reconstruction.

## 3.2 Scintillation event reconstruction

The output signals of the photosensors must be processed in order to determine the position and energy of the projected scintillation events. The final image is a density map of the reconstructed positions of the (ideally only "good") events.

A good event is defined by being within the right energy range (which depends on the radioactive source), and having all of its energy deposited in a single point within the scintillator. Examples of bad events are scintillations caused by other sources of radioactivity than the intended one, energy deposition by a gamma particle that suffered Compton scattering in the patient's body before detection, and multiple events (a gamma particle deposits energy in more than one point, or multiple gamma particles interact with the scintillator in an overlapping time-window).

The two most commonly used approaches to reconstruct the position and energy of an event are:

- Centroid method

- Reconstruction methods based on statistical algorithms

### 3.2.1 Centroid

The centroid (or center of gravity) method calculates the (two-dimensional) position of the scintillation event by averaging the position of the sensors weighted by the amplitude of their respective signals, according to the following equation:

$$\vec{R} = \frac{\sum_{i=0}^{N} S_i \vec{r_i}}{\sum_{i=0}^{N} S_i} \tag{3.4}$$

where $\vec{R}$ is the estimated scintillation event position, $N$ is the number of sensors, and $\vec{r_i}$ and $S_i$ are the position and signal of the $i$-th sensor, respectively. The calculations in eq. 3.4 can be easily implemented in analog or digital electronics. The method requires only the positions of the sensors.

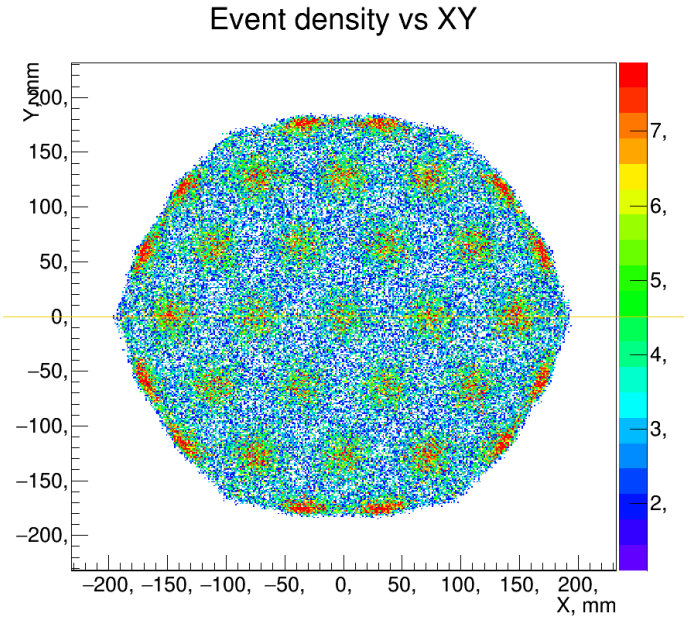


Figure 3.4: Example of image reconstruction using the centroid algorithm, of a uniformly irradiated detector with 37 photosensors in a regular hexagonal distribution. Since it was uniformly irradiated the image should have very small density gradients, only due to signal noise. However "hotspots" can be seen under each photosensor, an effect which is aggravated at the edges of the detector.

The centroid algorithm works best if there is a linear dependence of the photosensor signal output with the distance between the event position and the center of the photosensor. However, this assumption is not valid in most cases, and as can be seen in figure 3.4, simply applying the above algorithm results in a highly distorted image.

Solutions to this problem involve creating a look-up table that maps the centroid-reconstructed position to the true one. The creation of such table is a costly, and

time-consuming calibration procedure. In addition to that, the gains of the photosensors drift with both time and temperature, therefore the calibration procedure has to be performed regularly, which results in additional costs and down-times in medical practice.

### 3.2.2 Statistical algorithms

Reconstruction methods based on statistical algorithms calculate the position of the scintillation event by finding the position for which the vector of expected signals $a_i$, best matches the vector of measured signals $A_i$ (see figure 3.5). Although this requires more than just the positions of the photosensors, and has a higher computational cost, its results are potentially far better than those of the uncorrected centroid method.

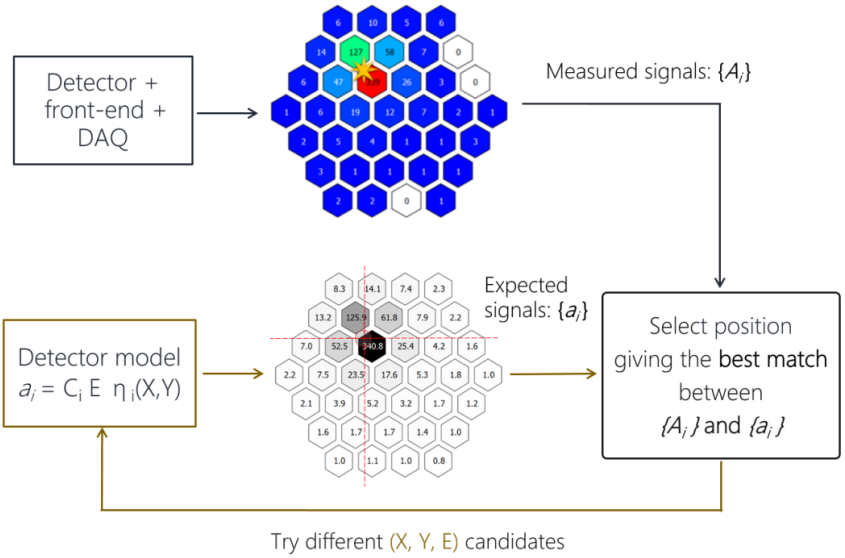


Figure 3.5: Flowchart of the reconstruction method based on statistical algorithms.

There are three main causes for fluctuations of the output signal from a photosensor irradiated by a fixed source of constant intensity:

- Statistical fluctuations (of both detected light and dark current)
- Fluctuations of single photoelectron response
- Electronic noise.

The match between the expected and the measured signals can be characterized using methods such as least squares or maximum likelihood. Both methods require an a priori knowledge of the expected signals as a function of the scintillation event position (detector model), as well as an assumption on the shape of the distribution.

In the least squares method, the match $S$ is characterized by the sum of the squared differences between the measured and expected signals, weighted by the squared uncertainty of the measurement $\sigma$. The position and energy of the event can be found by minimizing it:

$$S = \sum_i \frac{(A_i - a_i)^2}{\sigma_i^2} \tag{3.5}$$

In the maximum likelihood method (first described in [12]), the likelihood of the match is characterized by $L$, the product of the probabilities of each sensor to read $n_i$ photons:

$$L = \prod_i P(n_i|\mu_i(x,y)) \tag{3.6}$$

where $\mu_i$ is the expected number of photons of the $i$-th photosensor, as a function of the position of the scintillation event. The position and energy of the event can be found by maximizing $L$. If it is assumed that the probabilities follow the Poisson distribution of average $\mu_i(x,y)$, this is also equivalent to maximizing $M_L$ given by:

$$M_L = \sum_i n_i ln(\mu_i) - \mu_i \tag{3.7}$$

In the limit of a high number of photons, this method is equivalent to least squares.

The best match position can be found using algorithms such as brute force, (searching for the minimum over a dense grid covering the whole field of view of the detector), Newton's method (finding the roots of the first-order derivative of a function, using an iterative procedure involving the calculation of the second-order derivative), gradient descent (starting from a given initial position, move slowly in the direction that minimizes the gradient of a function), contracting grids (iteratively divide the search area in a grid and find the node with minimum value, see [14]), and simplex or migrad (both found in the Minuit2 minimization library [19]).

There are two forms of detector model storage: non-parameterized, and parameterized. In the non-parameterized form, a map of the signal response of all photosensors is stored as a of a table. In the parameterized form, a function or spline is adjusted to best characterize the detector response, which can be obtained by scanning the field of view of the detector with a pencil beam, from simulations, or by using an adaptive approach (see section 4.6 and [20]).

Chapter 4

# ANTS2: Simulation toolkit

## 4.1 Overview

All of the simulations performed in this study were conducted using the ANTS2 [21] package. In this chapter a general description of the configuration, simulation, and image reconstruction procedures, as well as approximations and assumptions that are made in ANTS2, are presented. However, the description will be mostly limited to the scope of this study. For a complete ANTS2 user guide, see [2].

ANTS2 is a simulation and data processing package developed for position sensitive detectors with Anger camera type readout. It is capable of simulating events in this type of detectors, including interactions of gamma particles with a scintillator material, generation and tracing of optical photons, and generation of the corresponding output signals. The reconstruction module can process both simulated and imported experimental data containing photosensor signals, using one of several position reconstruction methods based on statistical reconstruction algorithms, artificial neural networks, k-NN searches, or the traditional centroid. The package is also developed for both rapid prototyping and detailed studies of complex real detectors. A detector model can be developed from a proof of concept to the final design by gradually adjusting the configuration, aided by scripting facilities.

Storage of detector geometry and all 3D navigation, such as determining the volume where the particle is currently located, finding the next material interface, or calculating the normal vector is performed using the TGeoManager class of the ROOT package [4, 5].

## 4.2 Detector configuration

The detector configuration module allows to create or modify a model of an Anger camera type detector (see [21] chapter 3).

### 4.2.1 Geometry definition

In the simplest case, the detector geometry can be represented by a stack of parallel slabs, with the same cross section, but with individually adjustable thickness, placed on top of each other along the Z axis. The stack is placed inside the *World* object, which is filled with a chosen material. In a more advanced case, the individual size and cross-section shape of the individual slabs can be adjusted. Additionally, it is possible to add individual objects of a given shape (one of box, cylinder, cone, sphere, or custom defined 8 vertices), size, position, and orientation. Each object volume has a material associated with it.

It is also possible to import an object from GDML [6] files. The configuration

process may be scripted, and ANTS2 automatically verifies if any objects overlap, warning the user.

### 4.2.2 Materials and particles

Material configuration falls under two categories: particle interaction properties, and optical properties.

In ANTS2, particles are generated by "particle sources", which are characterized by its shape, size, position, and orientation, as well as its collimation cone with a given orientation and opening angle. Particle sources may be composed of multiple particles, and each particle has its own energy (or energy spectrum) and emission probability. It is also possible to have multiple simultaneous particle sources, each with its relative activity.

#### Particle interaction properties

The configurable particle interaction properties of the material depend on the type of the particle. In ANTS2 there are three types of particles that can be simulated: gamma particles, neutrons, and charged particles. Electrons (despite being charged particles) are assumed to deposit their energy locally, which is generally a good approximation for the ANTS2 target detector types.

The energy range of gamma particles of interest to medical imaging is of the order of tens to hundreds of keV. Therefore, pair production is not considered, and only photoelectric absorption and Compton scattering effects are simulated. The required properties, for gamma particles, are the material density (used in all particle interactions), and the mass attenuation coefficient as a function of energy, for each of the two effects. These values are used to calculate the mean free path of the particles. The attenuation coefficients may be imported from NIST XCOM database [3].

In addition to that, materials may also be set as either "transparent" or "opaque" for a given particle type. In transparent materials, particles move without interacting. If a particle enters an opaque material, tracking of the particle ends. By default, materials are transparent for all particle types.

A material may also be a scintillator, which triggers the emission of photons when particles interact with it, depositing energy. For such materials, the photon yield (see section 3.1.2) for each relevant material-particle pair has to be defined.

#### Optical properties

The configurable optical properties are the refractive index, the bulk absorption coefficient and the reemission probability, as well as the mean free path of Rayleigh

scattering.

If the material is a scintillator, the emission spectrum and the decay time properties have to be defined for wavelength-resolved simulations. ANTS2 also provides a tool to estimate the average quantum efficiency of a photosensor, based on the photosensor detection efficiency vs wavelength and the emission spectrum of the scintillator material.

By default, the behavior of an optical photon at the interface of two materials is defined solely by their refractive index and the angle between the photon and the normal of the interface, using the Fresnel equations (see chapter 2.3.1) and Snell's law (see chapter 2.3.2). In addition, ANTS2 provides three other possible processes, which may occur in any interface: absorption, specular reflection, and diffuse scattering. It is possible to configure their probabilities for any pair of materials and, for scattering, one of Lambertian (see chapter 2.3.4) or isotropic profiles may be chosen. These processes are described in chapter 4.3.3.

### 4.2.3 Photosensors

Photosensors have four sets of configurable parameters: geometrical, optical, photoelectric conversion, and electronics. They behave like regular objects, but cannot be scintillators, and have additional properties used to convert the number of photons triggering them, into electrical signals.

The configurable photoelectric conversion properties are the photon detection probability (optionally with wavelength, position and angular dependence), the gain, and the dark current. For SiPM type photosensors, dark current takes the form of dark count rate, for which the number of pixels, their recovery time, and the time interval of one measurement are also configurable.

The configurable electronic properties are: electronic noise, single photoelectron response, and signal digitization.

## 4.3 Simulation

There are two modes of simulation in ANTS2 (see [21], chapter 4): particle source mode, and photon source mode. In the former, the user defines one or multiple sources of particles. Each particle is tracked, and may generate a number of photons proportional to the energy they deposited in the detector. In the latter, the coordinates of the emission points and the number of generated photons are defined in configuration.

Particle source mode simulations are capable of providing a more realistic output, which can be directly compared with the experimental data acquired from the

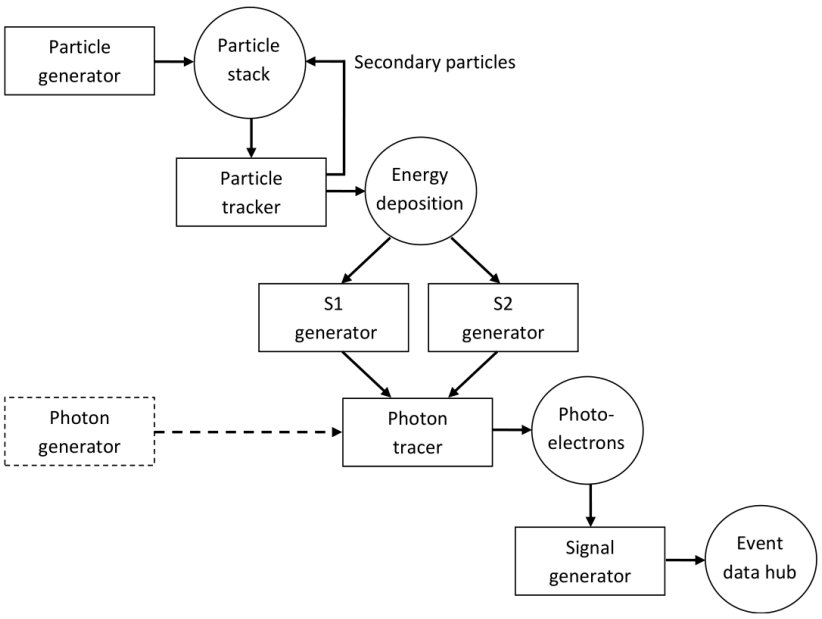


Figure 4.1: Flowchart of the simulation module operation in the particle sources mode. S1 and S2 are primary and secondary scintillation, respectively. Secondary scintillation is not relevant for the detector type in this study. The photon source simulation mode uses an alternative method of photon generation. Starting from the photon tracing phase, the operation is the same for both modes. [21]

corresponding detector. They also require a bigger effort to configure. Simulations in photon source mode are usually sufficient to generate data necessary for high precision reconstruction of the detector spatial response.

Simulation processes each event independently. An event is defined as the sequence of the processes triggered by the interactions of a particle with the detector (in the case of particle source simulation mode), followed by tracing of the emitted optical photons, and the generation of the respective signal response in the photosensors. Figure 4.1 presents a flowchart of the simulation process.

### 4.3.1 Particle tracking

In particle source mode, the processing of an event begins by generating a stack of particles to track:

1. The **source** is chosen randomly, based on the relative activity of all possible sources.

2. A **particle** is randomly selected from the chosen source, based on its generation probability.

3. The particle **position** is determined, by randomly choosing a position from the source volume, using an uniform distribution.

4. The particle **energy** is determined, by sampling the configured spectrum (if available), or using the configured constant value.

5. The particle **direction** is chosen randomly, from an isotropic distribution of the configured collimation cone.

Afterwards, each particle on the stack is tracked, one by one, independently. When the tracking of a particle is finished, it is removed from the stack. If during the tracking of a particle, a new particle is generated, it is appended to the stack. The processing of the event is finished when the stack is empty.

For neutral particles, tracking is done by finding the next volume along the path of the particle, and calculating the distance from the current position. Then, for each interaction process, the corresponding ranges are randomly generated using its mean free path for the current material. If the shortest traveling distance is less than the distance to the next volume interface, the interaction is triggered. Otherwise the particle is transported to the next volume. If the volume is outside the detector geometry, tracking of the particle ends. For gamma particles, there are two possible interaction processes:

**Photoelectric effect** in which all of the particle energy is deposited in the location of interaction. For this study this is a sufficiently good approximation.

**Compton effect** in which the energy loss and the new direction of the particle are randomly generated according to the Klein-Nishina formula. It is also assumed that the energy is deposited in the location of the interaction.

### 4.3.2 Scintillation

For scintillation, each energy deposition triggers isotropic emission of optical photons from the position where it took place. The number of emitted photons is the product of the deposited energy and the photon yield for the corresponding particle and volume material at the emission position. The generated photons are processed independently, one at a time, in the photon tracer.

For wavelength-resolved simulations, a random wavelength is assigned to each generated photon, sampled from the defined scintillation spectrum.

### 4.3.3 Optical photons tracing

Photon tracing begins at an emission position defined by the position where a particle deposited its energy, or the configured position of a photon source simulation.

For photon tracing, the distance to the intersection of the photon with the next interface is calculated, based on the emission position of the photon, and its direction. Ranges for both Rayleigh scattering and absorption processes are randomly generated from the scattering mean free path and the absorption coefficient of the current material, respectively. If the distance to the shortest range is less than the distance to the next material interface, the process is triggered:

- For **Rayleigh scattering**, a new photon direction is generated, and the tracing process restarts.
- For **absorption**, tracing of the photon ends.

If neither process is triggered, the photon reaches the interface of the two materials. If the photon leaves the detector geometry, tracing of the photon also ends.

If custom interface options (see chapter 4.2.2) are defined for the current pair of materials, one of the processes is randomly selected, based on its probability.

- For **loss**, tracing of the photon ends.
- For **specular reflection**, the photon direction changes according to equation 2.14, and the tracing process restarts.
- For **scattering**, the photon direction is randomized in either $2\pi$ (forward or backward) according to Lambert's law or isotropically, depending on user configuration. The tracing process restarts.

If custom interface options are not defined, Fresnel equations (see eq. 2.8) are used to determine if the photon is reflected back (according to eq. 2.14), or refracted into the next material, in which case, Snell's law (see eq. 2.16) is used to calculate the new direction of the photon.

The process restarts until absorption or loss are triggered, a maximum number (defined by the user) of photon tracing cycles is reached (due to full internal reflections, some photons are trapped in infinite trajectories), or a sensor is reached, in which case the photon detection procedure is triggered.

### 4.3.4 Photon detection

Detection probability of a sensor is calculated as the product of three factors:

$$P_{det} = Q(\lambda)P_t(\Theta)P_A(x, y) \tag{4.1}$$

where $Q(\lambda)$ is the quantum efficiency of the sensor at the photon wavelength, $P_t(\Theta)$ is the relative angular dependence of the detection probability as a function of the angle

of incidence (unity at normal incidence), and $P_A(x, y)$ is the relative dependence of the detection probability across the sensor surface.

It is randomly chosen if the photon is detected or not, according to the detection probability.

### 4.3.5 Conversion into output signal

By default, the signal generated by each sensor is equal to the amount of photons it detected. However, it is also possible to simulate the signals generated by the photosensors, taking into account: single photoelectron response, dark current/counts, electronic noise, and signal digitization noise, depending on the configuration.

SiPM dark counts are simulated using the configured dark count rate and the time interval of one measurement. Their product is the average number of dark counts. Dark triggering probability is calculated by dividing the average number of dark counts by the number of pixels of the photosensor. For low dark triggering probability (such as the one in this study), the number of dark counts is sampled from a Poisson distribution, and that number of pixels are triggered, randomly and uniformly distributed over the whole photosensor area.

## 4.4 Reconstruction methods

There are four groups of reconstruction methods implemented in ANTS2: centroid method, statistical algorithms based reconstruction, artificial neural networks, and k-NN. As discussed in chapter 3.2.1, the centroid reconstruction typically has low accuracy but is very useful to make an approximate estimate of event positions. If experimental calibration data is available, image reconstruction may be based on artificial neural networks or k-NN. As these were not used in this study, they will not be discussed. When a mathematical model of the detector response is known, image reconstruction can be performed based on statistical algorithms. This was the chosen method to reconstruct images from simulation and experimental data in this study.

When using experimental data, it is often the case that photosensors have different relative gains. It is possible to evaluate these gains in ANTS2, using flood field[1] experimental data, or using the LRF module. A preprocessing procedure can be applied to the imported experimental data to take into account the evaluated gain values. After such correction, all operations within the reconstruction module can be done assuming equal gains for all photosensors.

[1]Events uniformly distributed over the field of view of the detector.

### 4.4.1 Centroid method

Similar to eq. 3.4, ANTS2 implements the centroid method as follows:

$$x = \frac{\sum_i X_i S_i / g_i}{\sum_i S_i / g_i}, \qquad y = \frac{\sum_i Y_i S_i / g_i}{\sum_i S_i / g_i} \tag{4.2}$$

where $x$ and $y$ are the reconstructed positions, and $(X_i, Y_i)$, $S_i$ and $g_i$ are the position, signal and relative gain, of the $i$-th sensor, respectively.

To solve the compression effect that typically results from the centroid method, reconstructed coordinates may be multiplied by a given factor, independently in each direction. In addition, photosensors with a signal lower than a given value, and/or situated farther than a given distance from the position of the sensor with the highest signal, can be ignored during the reconstruction. This can improve accuracy of the position reconstruction, by removing the contribution of photosensors with output signals dominated by noise, as well as reducing the compression effect, by removing the contribution of photosensors far from the scintillation position.

### 4.4.2 Statistical algorithms

For each event, statistical methods search for the position and (optionally) the event energy, which results in the best match between the photosensor signals and those provided by the mathematical model of the detector.

The statistical methods implemented in ANTS2 can use either the Maximum Likelihood or the Least Squares approach to evaluate the match between the sets of the photosensor signals. The best match position is found using either the algorithms provided in the Minuit2 [19] minimization library or by a modified contracting grids method (described below). The contracting grids method has higher chances of converging to the global minimum, and may be run on a GPU platform, which is typically faster than the CPU-based reconstruction. Therefore, it was the method used in this work.

In the contracting grids algorithm of ANTS2, for each event, a regular grid of nodes is defined, centered at the initial search position (e.g. reconstructed position using centroid method).

For each node, the position which best matches the photosensor signals and the expected signals, given by the LRFs (Light Response Functions) for this node position, is chosen. This position is used as the center of a finer grid, with the same number of nodes, and the procedure is repeated for a configured number of iterations. The event energy, evaluated at each node, is the ratio between the sum of the signals of the photosensors and the sum of the LRF values.

As in the centroid reconstruction method, photosensors with a signal lower than

a given value, or situated farther than a given distance from the position of the sensor with the highest signal, can be ignored during the reconstruction.

## 4.5 Light response function

As mentioned above, statistical reconstruction requires a mathematical model of the detector response. In ANTS2, this model is represented by a set of LRFs (Light Response Functions). An LRF describes the average signal of a photosensor as a function of the position of a point light source emitting a constant number of photons (see [21], chapter 6). They are parameterized based on a custom B-spline library [24]. The LRF module calculates the LRFs based on the signals of the photosensors and the corresponding event positions.

For gamma cameras in this study, only the X and Y coordinates of an event have to be reconstructed, so the Z dependency of the LRFs may be ignored. Furthermore, we intend to build a detector for which it is possible to apply iterative reconstruction [20] of its response. For that, LRFs of *Axial* type must be used. This choice also allows to significantly reduce the required number of parameters, as well as provide sufficient regularization to ensure convergence even with low photon statistics. The validity of this choice of LRF type, for reconstructions in this study, will be verified in chapter 5.

ANTS2 allows to arrange photosensors in groups, exploiting the symmetry of the detector (see [21] chapter 6.2, and [24] chapter 3.4). Photosensors in the same group share the same LRF, scaled individually by a factor to compensate for their different gains. When calculating a group LRF, the size of the set of photosensors signals (dataset), used for fitting the LRFs (see section 3.2.2, effectively increases. This reduces the amount of experimental data required to calculate the detector LRFs. This technique is also advantageous when applying iterative LRF reconstruction (see section 4.6).

Another useful technique available in ANTS2, is the use of compressed LRFs (see [24], chapter 3.2). It reduces the number of parameters the LRF requires to store the model of the detector response. If the dataset is not large enough, an inadequate parameterization scheme may also be the cause of LRF overfitting, resulting in artifacts in the reconstructed image.

## 4.6 Iterative LRF reconstruction

The method of iterative reconstruction of the spatial response of an Anger camera-type detector was first described in [25]. This procedure was heavily used in this study. Briefly put, it consists in starting with an initial guess of LRFs, and using

it to reconstruct the positions of a flood field irradiation by means of a statistical reconstruction technique. From the newly reconstructed positions and the signals of the photosensors, a new set of LRFs is calculated. The process is repeated iteratively, until the LRFs converge.

LRFs can be initially estimated using simulation data, in which case both the photosensors signals and the exact corresponding event positions are known, or estimated from experimental data reconstructed with the centroid method. While the procedure is quite tolerant to the initial estimation, it requires adjustments for each particular detector [21].

The first few iterations are especially sensitive, and a poor choice of parameters may easily increase the required number of iterations for convergence, or even stagnate the process. At this stage, sensor grouping can be particularly helpful to define the general LRF profile for the photosensors. Later on, grouping can be disabled to allow the LRFs to be adjusted to each particular photosensor. Small random shifts to reconstructed positions, applied after each iteration, may also improve LRF calculation [20]. In ANTS2, this is called blurring.

Typically, there will be a fraction of the events which is reconstructed with large errors due to, for example, the inadequacy of LRFs, or energy deposition in multiple positions, which may occur with the Compton effect. This can cause significant distortions on the LRF profiles, resulting in failure of the iterative procedure. For that, ANTS2 provides tools to filter out those events during the iterative procedure. For example, filters may select any combination of photosensor output signal, energy, position, or chi2 ranges. For more advanced cases, a custom script may also be used to filter events.

Chapter 5

# Simulation model validation

## 5.1 Gamma camera prototype & model

Before beginning the optimization procedure, a prototype of a compact gamma camera is needed, both as starting point of the optimization procedure and to test the validity of the model and the simulation package.

There is an interest, first and foremost, in the intrinsic properties of the detector, hence the prototype was designed without a collimator. All other components mentioned in chapter 3 are present.

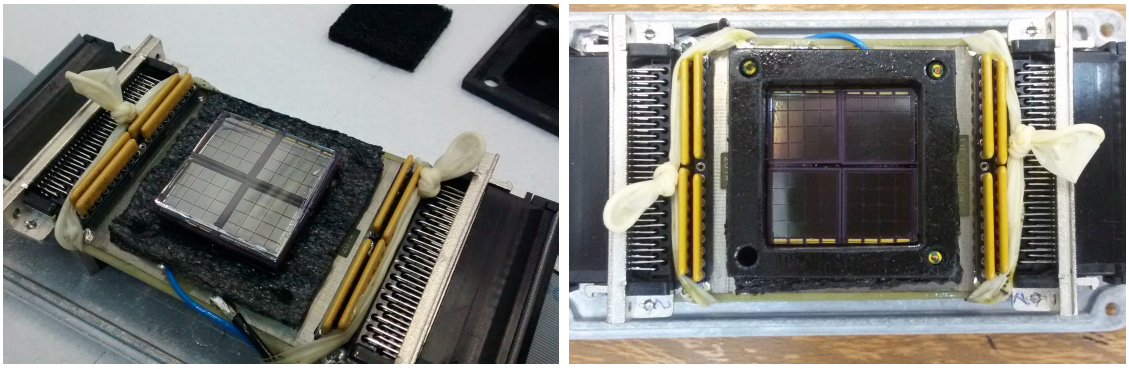

Figure 5.1: The compact gamma camera prototype, with the lid off: **Left**: without the light tight box nor the PTFE backplate; **Right**: with light tight box.

### 5.1.1 Geometry

The detector is composed of three layers, described in table 5.1, each optically coupled by a thin layer of optical grease. The sides are covered with a patch of black paper, also coupled with optical grease. This is expected to reduce reflections from the side, and thus to improve axial symmetry of the detector. The black paper was simulated by using optical grease as the world object material, since light entering such material would not be detected.

The photosensors of the designed prototype were the MicroSB-30035 model SiPMs from SensL, due to their high photodetection efficiency, low dark count rate,

| Layer | Material | Thickness/mm | Area/mm × mm |
|---|---|---|---|
| SiPM packages | Ceramics | 0.6 | 32.0 × 34.0 |
| Optical coupling | Optical grease | 0.1 | 31.0 × 32.5 |
| Lightguide | Acrylic | 1.5 | 31.0 × 32.5 |
| Optical coupling | Optical grease | 0.1 | 30.0 × 30.0 |
| Scintillation crystal | LYSO [10] | 2.0 | 30.0 × 30.0 |
| Optical coupling | Optical grease | 0.1 | 30.0 × 30.0 |
| PTFE backplate | PTFE | 1.0 | 30.0 × 30.0 |

Table 5.1: The layers of the compact gamma camera. All layers are of rectangular shape.

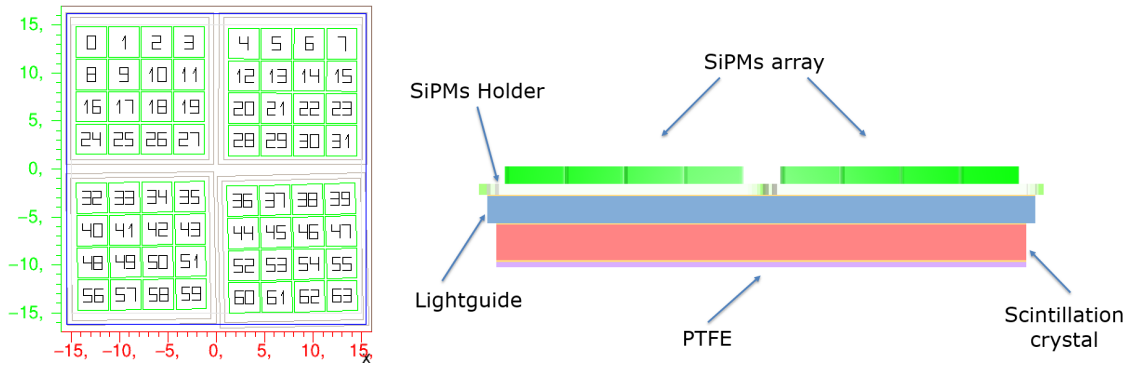


Figure 5.2: Simulation detector model. **Left**: a top-view showing SiPM index numbers; **Right**: a perspective side-view.

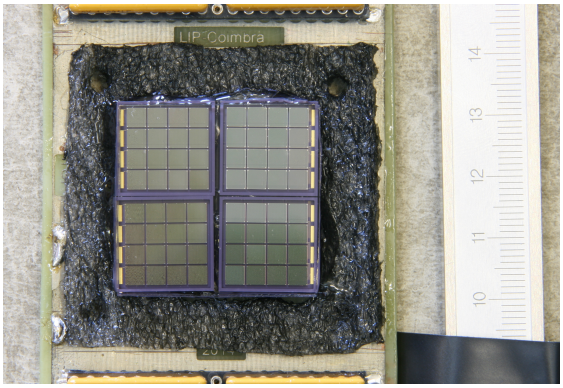


Figure 5.3: Image used to analyze real positions of SiPMs in detector.

and affordable price. The SiPMs are arranged in arrays of $4 \times 4$ sensors mounted inside a ceramic holder. Each sensor has a size of 3.16 mm × 3.16 mm and contains 4774 pixels. The material of its optical interface is Epoxy [23].

The manufacturer has mounted the SiPMs ≈0.6 mm below the level of the ceramic holder borders for surface protection. This gap was filled with optical grease, which effectively increases lightguide thickness by 0.6 mm. Note however, that from now on the term "lightguide thickness" refers only to the thickness of the lightguide layer in table 5.1.

The ceramic packages of the photosensor array have large tolerances that resulted in an inexact placement of the individual photosensors. For this reason, figure 5.3 was analyzed to determine the position and orientation of the photosensors. These positions, shown in table 5.2, were imported into the simulation model.

### 5.1.2 Material descriptions

#### Gamma interaction properties

All imported mass attenuation coefficients were obtained from the XCOM database, which provides coefficients for coherent and incoherent scattering, photoelectric ef-

| SiPM package | X/mm | Y/mm | Angle |
|---|---|---|---|
| Top left | −2.83 | +3.11 | 0° |
| Top right | +2.83 | +2.97 | −0.16° |
| Bottom left | −2.76 | −2.90 | 0.8° |
| Bottom right | +2.69 | −3.32 | 1.17° |

Table 5.2: SiPM package positions, estimated by analyzing figure 5.3

| Material | Element composition |
|---|---|
| LYSO [10] | $Lu_{1.9}Y_{0.1}SiO_5$(99.5 %), Ce(0.5 %) |
| Lead | Pb |
| Cerrosafe | Bi(42.5 %), Pb(37.7 %), Sn(11.3 %), Cd(8.5 %) |

Table 5.3: Materials element compositions. Materials not present in this table are considered to be fully transparent to gamma particles.

fect, pair production, and total attenuation coefficients, for gamma particles in the energy range of 1 keV to 100 GeV, interacting with any element, compound, or mixture. Table 5.3 contains the list of materials for which the total mass attenuation coefficients were imported into ANTS2, and the respective element compositions used in the XCOM database query. Other materials are considered to not interact with gamma particles, since their probability of interactions is negligible compared to that of the scintillator, as shown in figure 5.4.

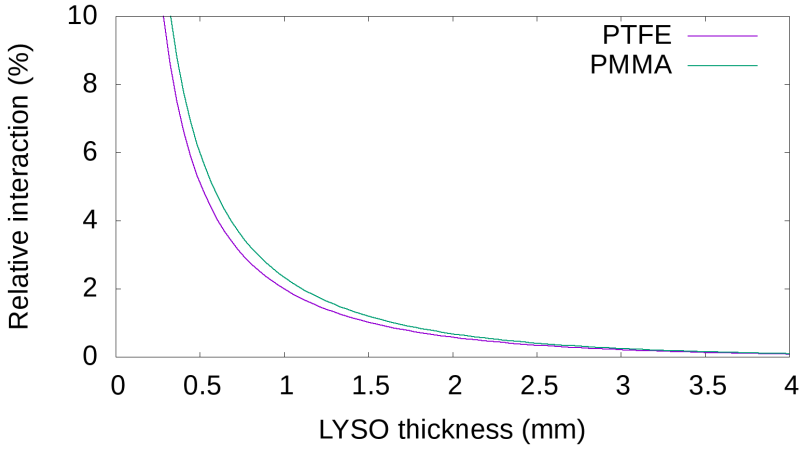


Figure 5.4: PTFE (1.0 mm thick) and lightguide (PMMA, 2 mm thick) relative (to that of LYSO) photoelectric absorption probability vs LYSO thickness. At 2 mm of scintillator thickness, the total probability is less than 1.3 %.

The scintillator emission spectrum is shown in figure 5.5. The scintillation properties were provided by the manufacturer, Epic Crystals [10]:

- Decay time: 40 ns
- Wavelength of the emission peak: 430 nm

- Photon yield: $25\,\mathrm{keV}^{-1}$

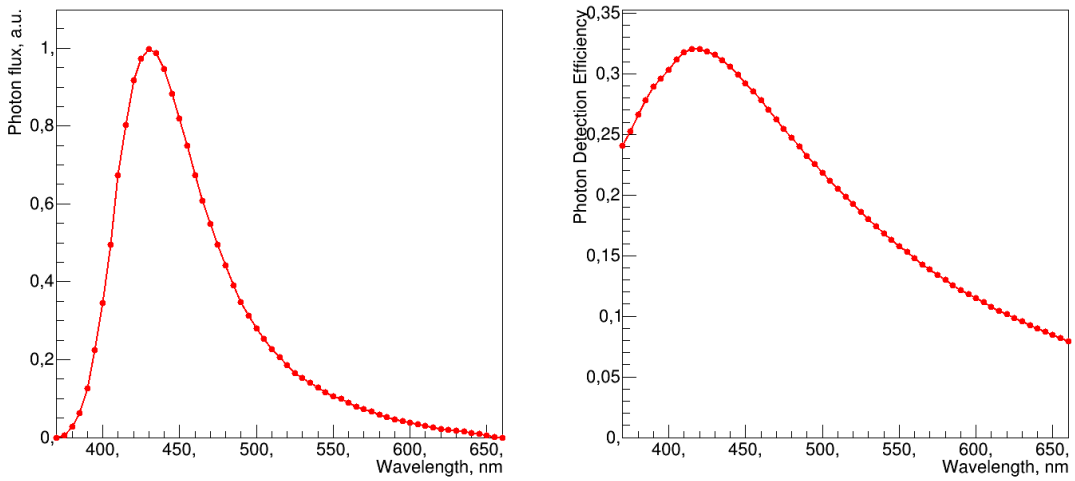


Figure 5.5: **Left**: LYSO wavelength emission spectrum, with peak at 430 nm [18]; **Right**: SiPMs detection efficiency spectrum, with a peak at 415 nm [23].

### Optical properties

Table 5.4 lists the wavelength-independent optical properties considered in this model, for all materials. Figure 5.6 presents refractive index vs wavelength. Of the materials where light is transported, I was unable to obtain the refractive index vs wavelength of the optical grease.

| Material | Density/g cm$^{-3}$ | Refractive index | Attenuation coefficient/mm$^{-1}$ |
|---|---|---|---|
| Air | $1.20 \times 10^{-3}$ | 1.00 | 0.0 |
| Acrylic | 1.19 | 1.50 | 0.0 |
| LYSO | 7.2 | 1.83 | $4.8 \times 10^{-3}$ |
| Epoxy | 1.3 | 1.59 | 0.0 |
| Optical Grease | 1.3 | 1.46 | 0.0 |
| Ceramics | 3.89 | 1.00 | $1.0 \times 10^{10}$ |
| Lead | 11.34 | 1.00 | $1.0 \times 10^{10}$ |
| Cerrosafe | 9.4 | 1.00 | $1.0 \times 10^{10}$ |
| PTFE | 2.2 | 1.50 | 0.0 |

Table 5.4: List of materials wavelength-independent optical properties. For attenuation coefficient, $1.0 \times 10^{10}$ is an arbitrarily large value that means that the material is fully opaque. The PTFE surface is modeled as an ideal diffusive reflector, and so light is never propagated into the material.

The photosensors detection efficiency was 27 %[1], and its wavelength dependency is presented in figure 5.5. Data was obtained from the manufacturer datasheet.

[1]Estimated using ANTS2, based on the photosensor detection efficiency vs wavelength at +2.5 V overvoltage and the emission spectrum of LYSO. See section 4.2.2

| Wavelength/nm | Refractive index |
|---|---|
| 325 | 1.632 |
| 450 | 1.585 |
| 550 | 1.570 |
| 642 | 1.560 |

Table 5.5: Epoxy refractive index vs wavelength used in the simulation model, as provided by the manufacturer by request.

LYSO manufacturer did not provide refractive index vs wavelength data, so approximations were made for this parameter. Although the material is birefrigent (due to its anisotropy), the effect is insignificant [9]. Furthermore, the ANTS2 package does not support birefrigent materials. Therefore, the refractive index vs wavelength of the material was considered to be the average of the Sellmeier dispersion equation of the three crystallographic axis, with the parameters obtained from results[2] in [11].

Acrylic refractive index vs wavelength was considered to follow the Sellmeier dispersion equation, with the parameters in [1]:

$$n(\lambda) = \sqrt{1 + \frac{1.1819\lambda^2}{\lambda^2 - 0.0113}} \tag{5.1}$$

which resulted from data reported in [27]. The data had to be extrapolated because the reported wavelength range was from 436.8 nm to 1052 nm.

Epoxy refractive index vs wavelength is presented in table 5.5, and figure 5.6. It was provided by the manufacturer, and imported as-is into ANTS2.

PTFE can be considered an ideal diffuse reflector. For the simulations in this study, it scatters back 95 % of incident photons, according to Lambert's emission law.

For materials of the optical components introduced above, refractive index changes by not more than 2 % between 400 nm and 500 nm (the region of most emission), so the values corresponding to the wavelength of peak emission (430 nm) were used. Since the manufacturer of the optical grease could only provide a typical value for the refractive index somewhere in range of visible light, this was the value used in the model.

[2]Although the LYSO formula in that work is $Lu_{1.6}Y_{0.4}SiO_5$ (Ce:0.2 %), note that in this study a slightly different composition of LYSO has been used. See table 5.3

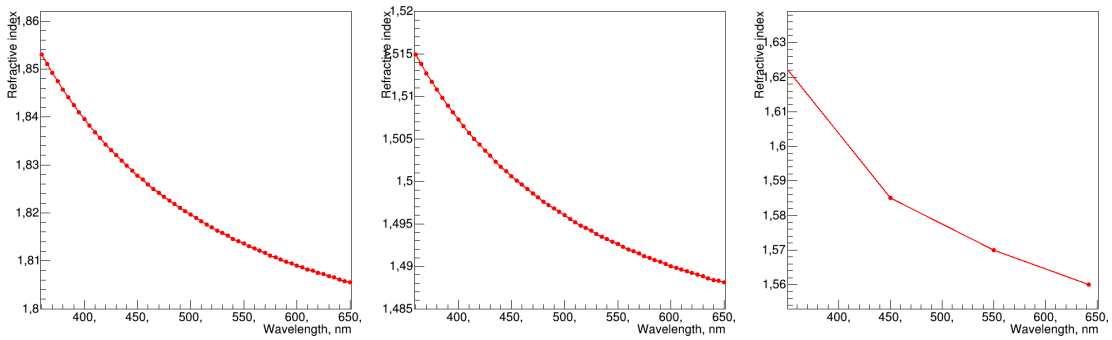


Figure 5.6: Materials refractive index vs wavelength: **Left**: LYSO; **Center**: acrylic; **Right**: epoxy.

## 5.2 Irradiation: experimental & simulation conditions

Before an image can be reconstructed using a statistical reconstruction technique, photosensor LRFs must be created, for which flood field irradiation data is needed. For both experiment and simulation, radiation was produced by a $^{99m}$Tc source, a cylinder of 3 mm diameter and 30 mm length. For the model, emission of gamma rays was considered to be isotropic and uniformly distributed over this volume. It was also considered that $^{99m}$Tc decays through gamma emission: either with an energy of 142.6 keV and a probability of 98.6 %, or with an energy of 140.5 keV and a probability of 1.4 %.

After LRFs were created, it was possible to reconstruct our choice of projected images: a grid, a slit, and an image of a phantom. The simulation configuration, which was intended to reproduce the experimental setup as close as possible, is described below. The differences between experimental setup and simulation configurations are specifically noted.

For the **Flood**, $5 \times 10^5$ uniformly distributed events were acquired. The source was positioned 1 m below the scintillator, to guarantee uniformity of irradiation.

The **Grid** was formed out of many identical source projections (nodes), arranged in a rectangular array, with a 2.1 mm pitch in both directions. To project each node of the grid, a collimator consisting of two 2 mm thick lead plates, parallel to the camera plane, were used, each with a hole in the center. Both plates were extended past the surface of the crystal. One plate was positioned 10 mm away from scintillator, with a hole diameter of 1 mm. The other plate was 50 mm away from the scintillator, with a hole diameter of 2 mm. The source was positioned 100 mm below the scintillator. This resulted in a projection with 1.1 mm diameter when entering the scintillator, and 1.2 mm when exiting.

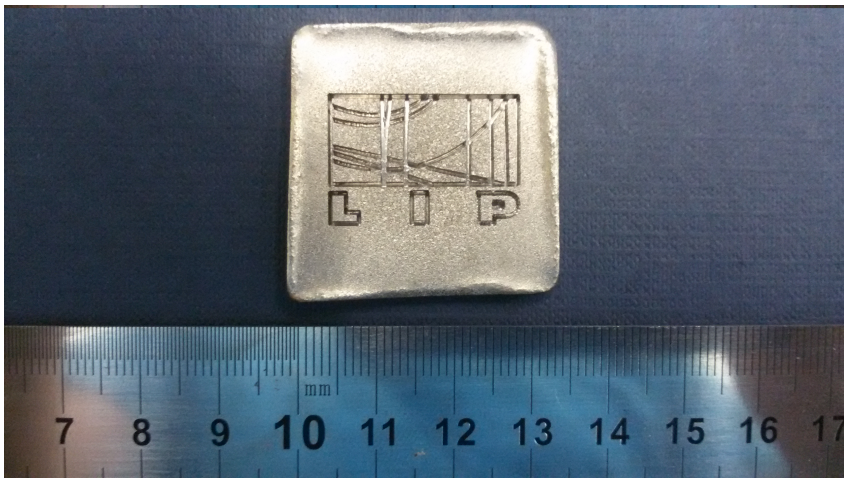


Figure 5.7: Phantom with LIP logo.

For the **Slit** projection, a 2 mm thick lead plate, with a 0.4 width slit was used. The slit was aligned with the Y axis and centered at −5.5 mm position along the X axis. For the simulation, the cut was an air object across the entire lead plate. The plate was positioned 4 mm below the scintillator, and the source 150 mm below the scintillator.

To record a **phantom image**, a 2 mm thick lead plate, with the LIP logo milled in it (with traces 0.5 mm wide and 1.5 mm deep), shown in figure 5.7, was placed between the detector, at a distance of about 4 mm from the crystal, and the source, positioned 1 m below the scintillator. This was experimental-only setup which was not simulated, as it would not add relevant information, when comparing to other irradiation methods.

## 5.3 Experimental data reconstruction

To be able to perform reconstruction with methods based on statistical algorithms, LRFs need to be calculated. Since true event positions are not know for experimental data, the calculation was performed iteratively from flood data (see section 4.6), according to the following procedure:

1. Load flood data, with electronic pedestals and channels per photoelectron taken into account (these can come from calibration procedures).
2. Apply filtering to *sum signals*, in order to remove events not within the expected energy range.
3. Reconstruct the flood data with the centroid method.
4. Apply spatial filtering to limit events to the central 28 mm × 28 mm square.

5. Create LRFs of radial type, with 10 compressed nodes, $\kappa = 5$, $r_0 = 7$, and $\lambda = 6$ (see section 4.5). A common LRF for all photosensors (with gain adjustment) should be used.

6. Reconstruct flood data using the LRFs of step 5, and recalculate LRFs.

7. Repeat steps 5 and 6 iteratively, possibly applying a modest amount (around 1 mm) of Gaussian blurring (see section 4.6), until LRFs converge.

8. From the last reconstruction, create new LRFs with the same settings as in 5, but without any grouping.

9. Reconstruct flood field data using the LRFs of step 8, and recalculate LRFs.

10. Repeat steps 8 and 9 iteratively, with a modest amount of blurring, until LRFs converge.

Figure 5.8 shows the image reconstruction of the acquired data. To get a better understanding of the overall position reconstruction bias and resolution of the reconstruction, figure 5.9 shows the grid projection image marked with the expected positions and dimensions of the radioactive source. The grid is rotated by $-0.6°$ due to some misplacement during setup.

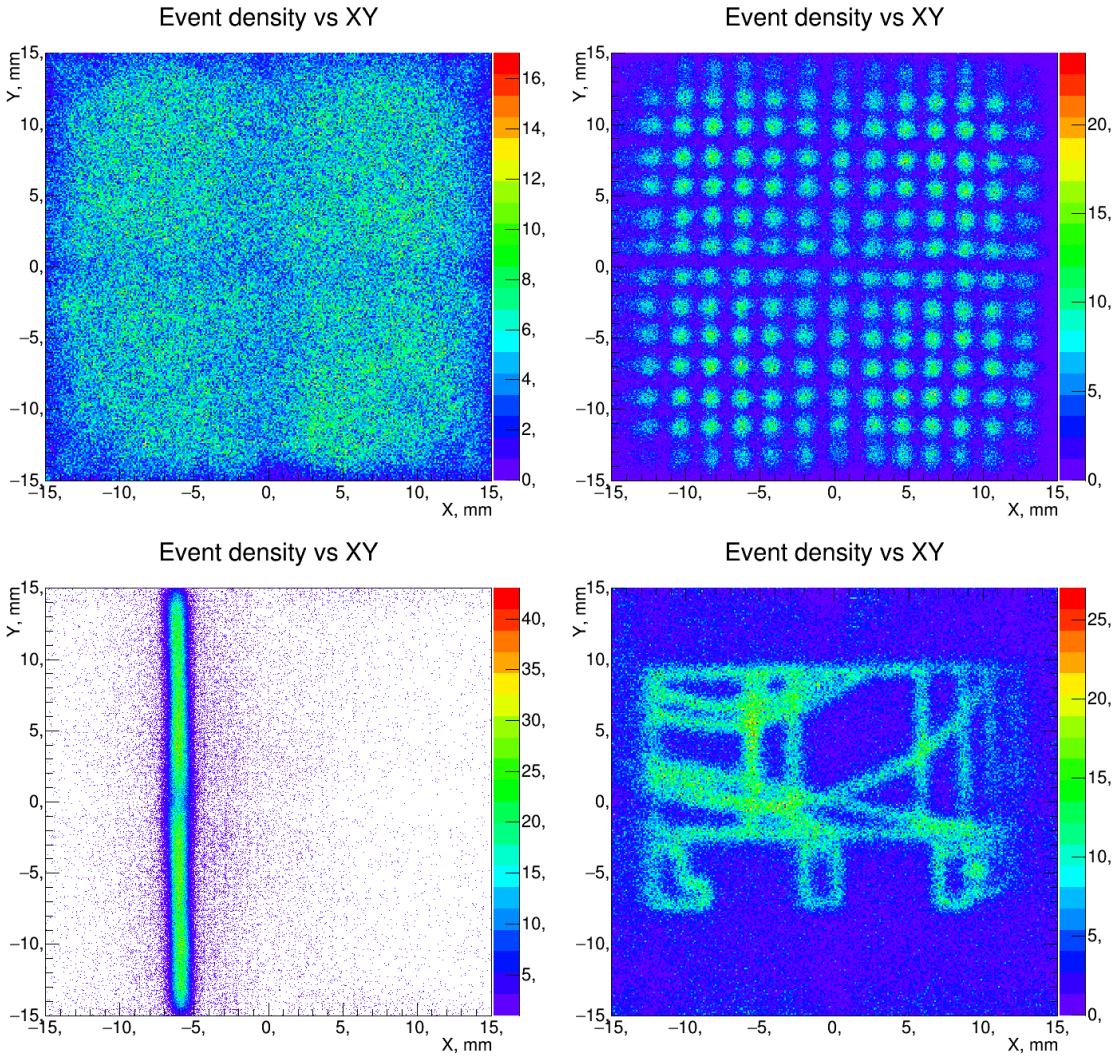


Figure 5.8: Experimental data reconstructed with LRFs obtained by means of iterative procedure (described above). **Top-left**: Flood; **Top-right**: Grid; **Bottom-right**: Slit; **Bottom-left**: Phantom with LIP logo.

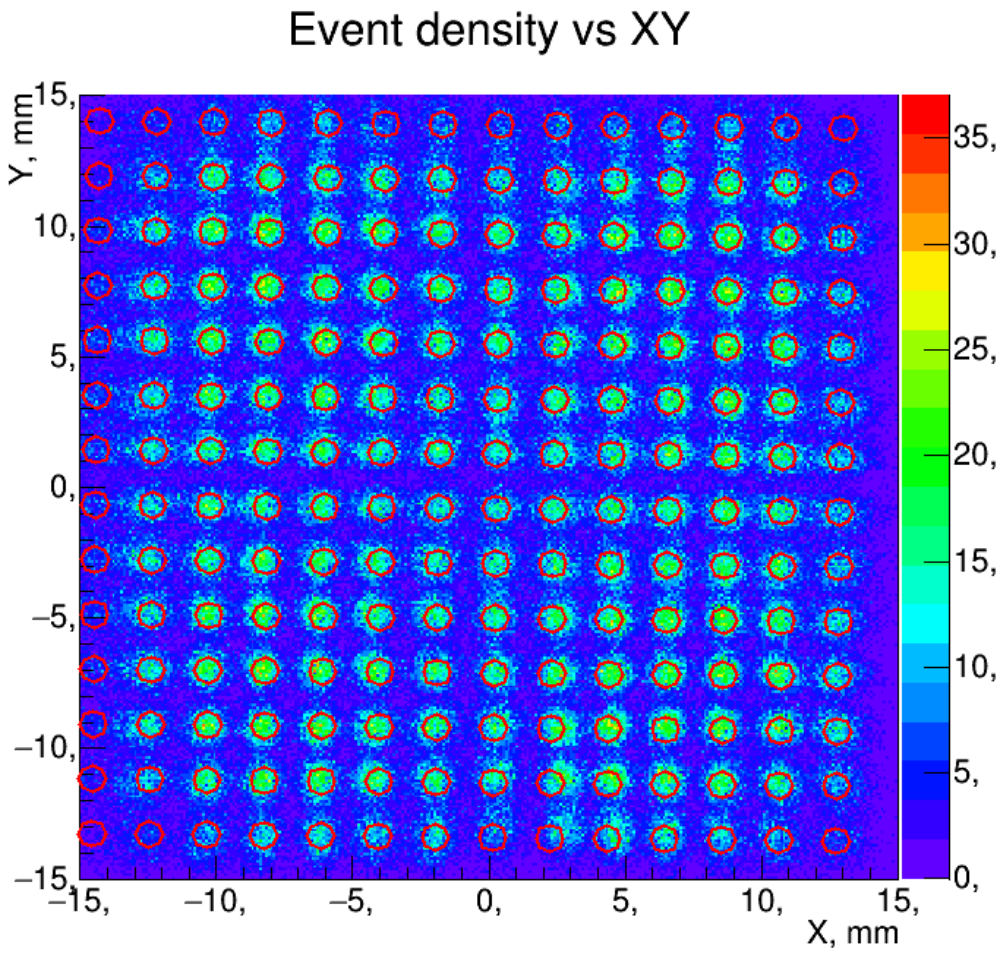


Figure 5.9: Experimental data reconstruction by means of iterative procedure, marked with expected radioactive source positions and dimensions.

## 5.4 Simulation data reconstruction

A flood simulation of $5 \times 10^5$ events was run, from which a set of LRFs was directly calculated (no iterative procedure was needed since the exact positions of events were known in simulations). The same LRF parameters as in the case of experimental data processing have been used: radial type, with 10 compressed nodes, $\kappa = 5$, $r_0 = 7$, and $\lambda = 6$. The ANTS2 script used to generate the simulation data is presented in appendix A. Figure 5.10 shows the reconstruction images of the simulation.

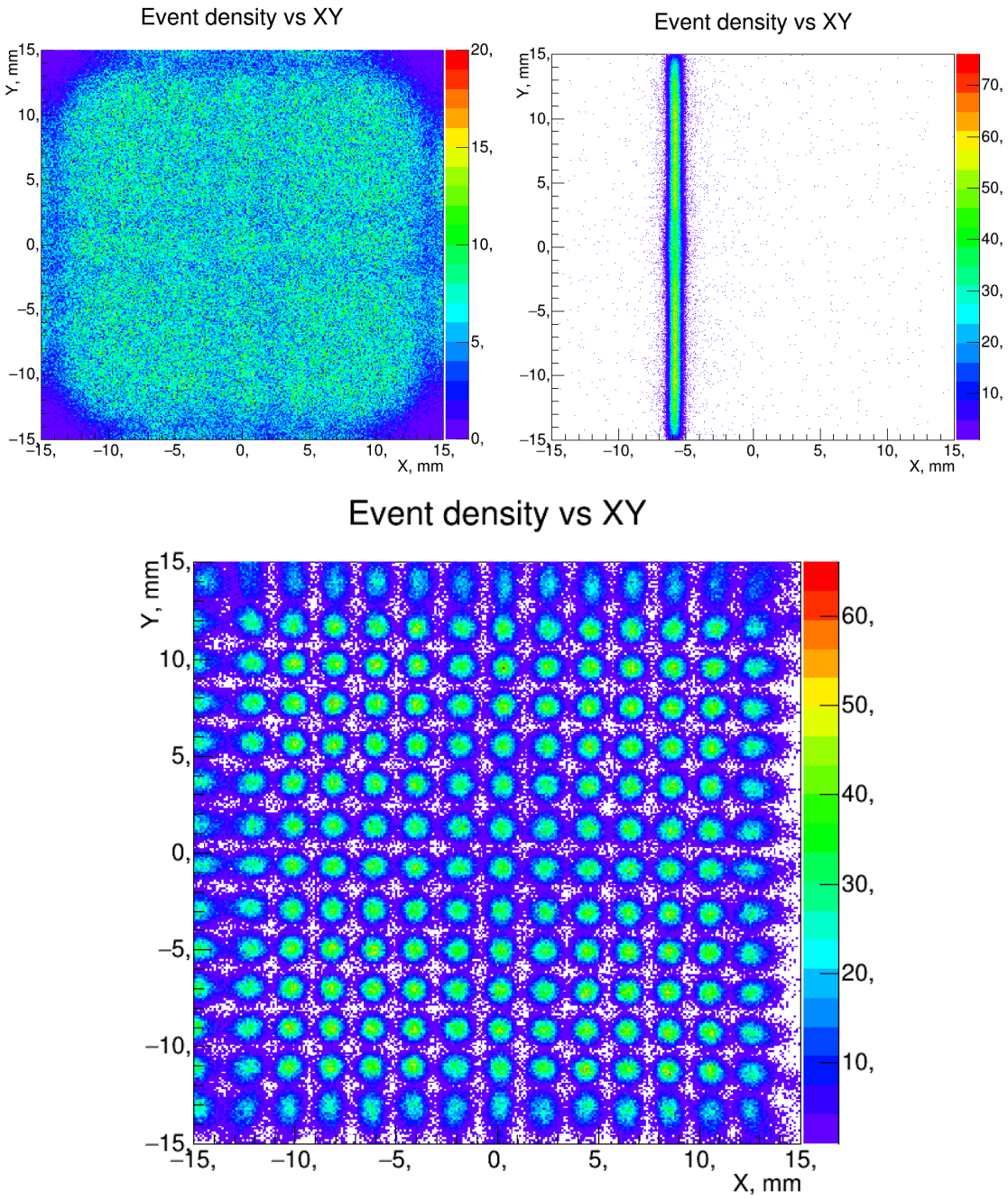


Figure 5.10: Simulated data reconstructed with LRFs obtained from a flood simulation. **Top-left**: Flood; **Top-right**: Slit; **Bottom-right**: Grid.

## 5.5 Comparison between simulation and experimental results

From figures 5.8 and 5.10, it is apparent that the simulation and the experimental reconstructions yield similar (but not identical) results. This is not unexpected, since many simplifications were made while creating the model of the camera. For instance, besides the previously stated simplifications, simulations do not account for electronic noise, excess noise factor of SiPMs, and the presence of background radiation[3], nor material inhomogeneities.

The first stage in validation was based on comparison of LRFs (profiles and absolute scales) reconstructed for simulation and experimental data. Since, in this case, LRFs are a fitted curve of signal response vs distance to event position, if two (properly fitted) LRFs are similar, the corresponding data should, in average, be similar as well. This would indicate that both the model, as well as the simulation package, are capable of predicting the relevant physics inside the real detector.

### 5.5.1 Direct LRF comparison

Figure 5.11 shows four plots, each comparing an experimental LRF with a simulation LRF. LRFs of SiPM #0, located at (−12.94 mm, 13.22 mm), have a near perfect match in the (very relevant) range of 2 mm to 9 mm. LRFs of SiPM #5, located at (6.23 mm, 13.07 mm), have a similar scale, and are, overall, quite similar, even though not as much as the others. Since the differences of quantum efficiency between individual SiPMs were not taken into account, and there are uncertainties of the order of 30 % for the relative electronic gains, LRFs of SiPMs #35, located at (−2.76 mm, −2.90 mm), and #42, located at (−6.08 mm, −6.32 mm), could be linearly scaled for a more meaningful comparison. The scaling result is presented in figure 5.12, and clearly these two pairs of LRFs are nearly indistinguishable!

The difference in the "tail" of LRFs (a section of LRFs at large distance from origin) can be easily explained, as simulation LRFs have, as a minimum value, the dark count average, and only typical dark count rate is provided by the manufacturer. However, since the reconstruction is configured to use only the range of distances up to 12 mm, differences at larger distances are irrelevant.

[3]Due to limited readout rate of the data acquisition system, used in the experiments, the fraction of recorded events that is due to background radiation varied from run to run, and is very difficult to estimate.

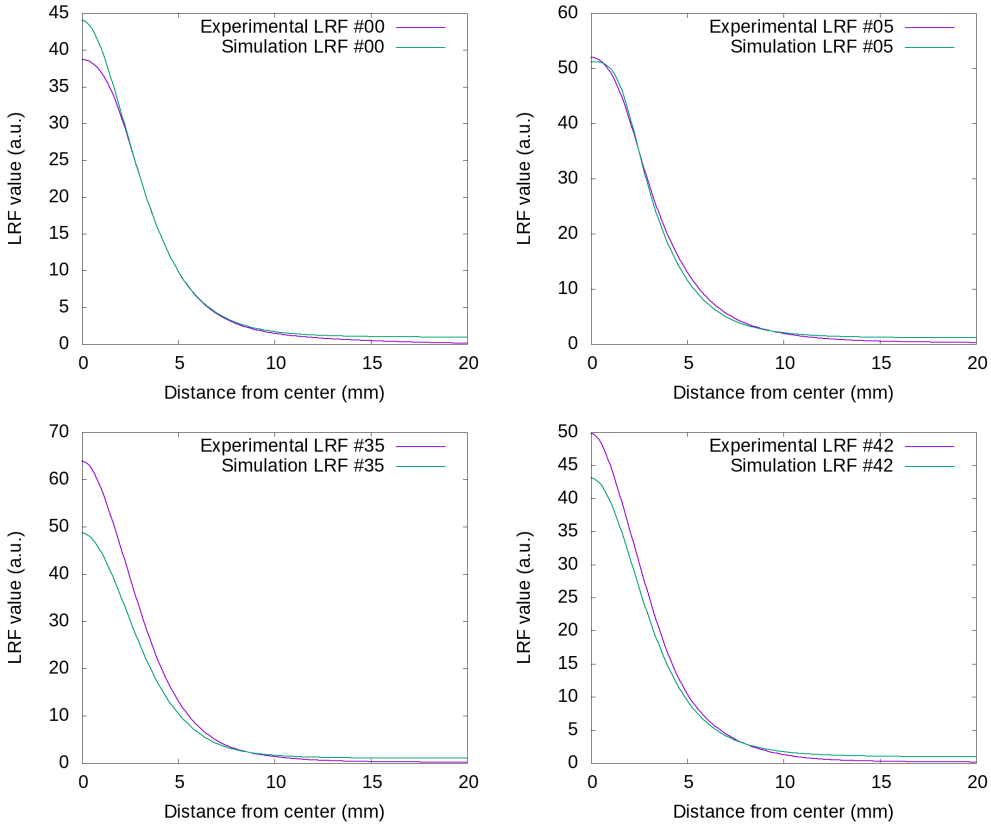


Figure 5.11: Side-by-side experimental and simulation LRF of: **Top-left**: SiPM #0; **Top-right**: SiPM #05; **Bottom-left**: SiPM #35; **Bottom-right**: SiPM #42. See figure 5.2 for SiPM numeration scheme.

### 5.5.2 Reconstruction of experimental data with simulation LRFs

While it was shown that simulation and experimental LRFs are similar, I would like to further validate the model, by using the LRFs calculated with simulated data to reconstruct the experimental data.

For that, experimental grid data was loaded taking into account the same number of channels per photoelectrons and pedestals as in 5.3.1. The data was then reconstructed using the LRFs obtained from the simulation, and the reconstruction parameters described in 5.4. The results are shown in figure 5.13.

The resulting reconstructed grid is clearly distorted. As was mentioned in the previous section, the values of channels per photoelectron are known with large uncertainties (≈30 %). Moreover, the relative gain of the photosensor is the product of the quantum efficiency and the electronic gains. Since the channels per photoelectron value only refers to the latter, while the former, in principle, can change from one SiPM to another, significant variations in the relative gains of individual sensors are expected for the experimental data. Effectively, the relative gains of the photosensors are not equalized, while the simulation was realized assuming that

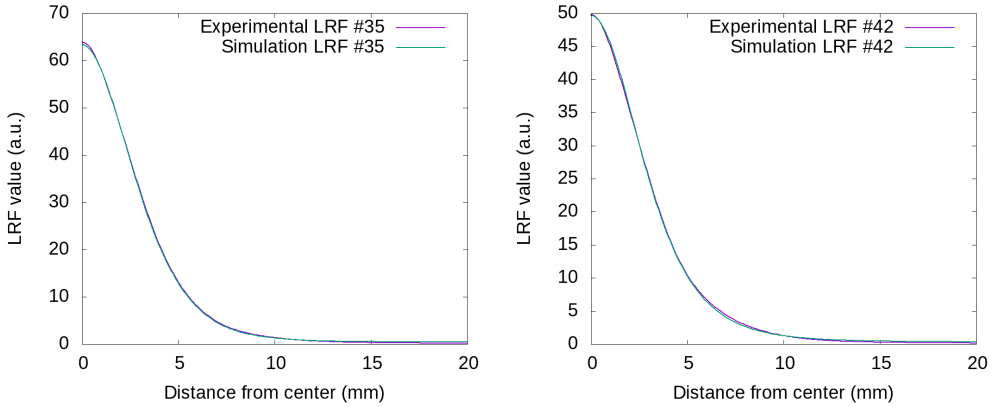


Figure 5.12: Side-by-side experimental and scaled simulation LRF of: **Left**: SiPM #35; **Right**: SiPM #42. See figure 5.2 for SiPM numeration scheme.

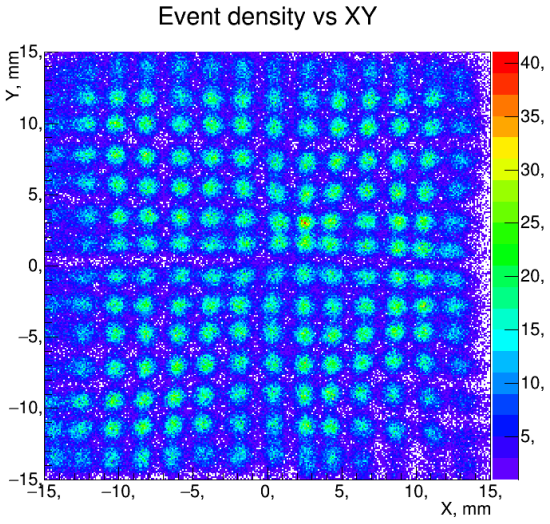


Figure 5.13: Experimental data reconstructed with simulation LRFs (without gain correction).

they were equal.

Thus, as an attempt to reduce these position reconstruction biases, a new flood simulation was made, where the gain of each photosensor was considered to be the ratio between the peaks of its respective LRFs: the one created with experimental data and the one obtained in the first simulation. A new set of LRFs was created from the new simulation and used to reconstruct the experimental data. The results are shown in figure 5.14, with figure 5.15 showing the marked grid.

Given the above results, I believe to have enough reasons to expect the simulation package and model to have an acceptable predictive power of the physics of a real camera. Thus by optimizing the simulation model of the camera I should obtain a set of optimized parameters for the real camera.

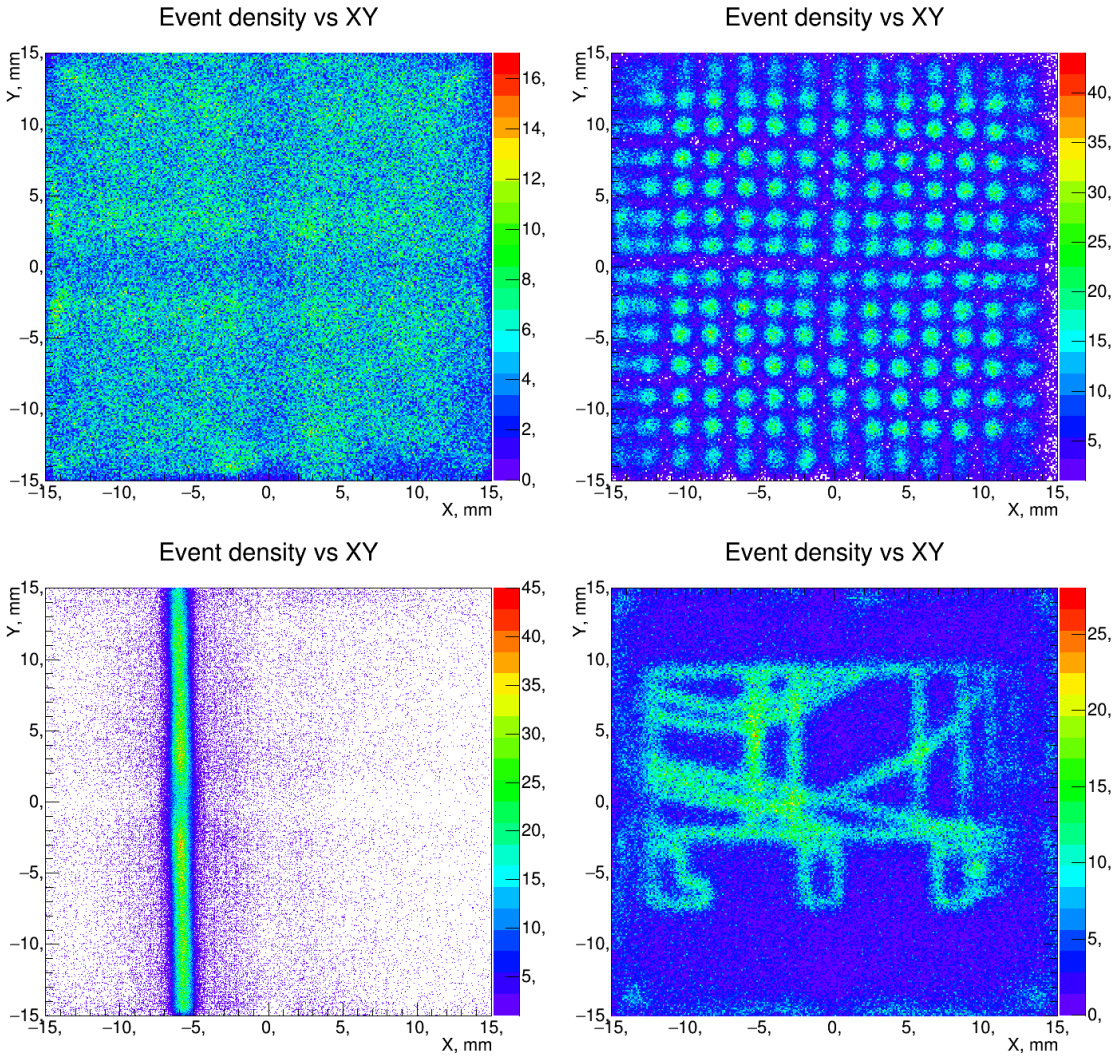


Figure 5.14: Experimental data reconstructed with LRFs obtained from a flood field simulation, where gains were scaled according to experimental LRFs peaks. **Top-right**: Flood; **Top-left**: Grid; **Bottom-right**: Slit; **Bottom-left**: Phantom with LIP logo.

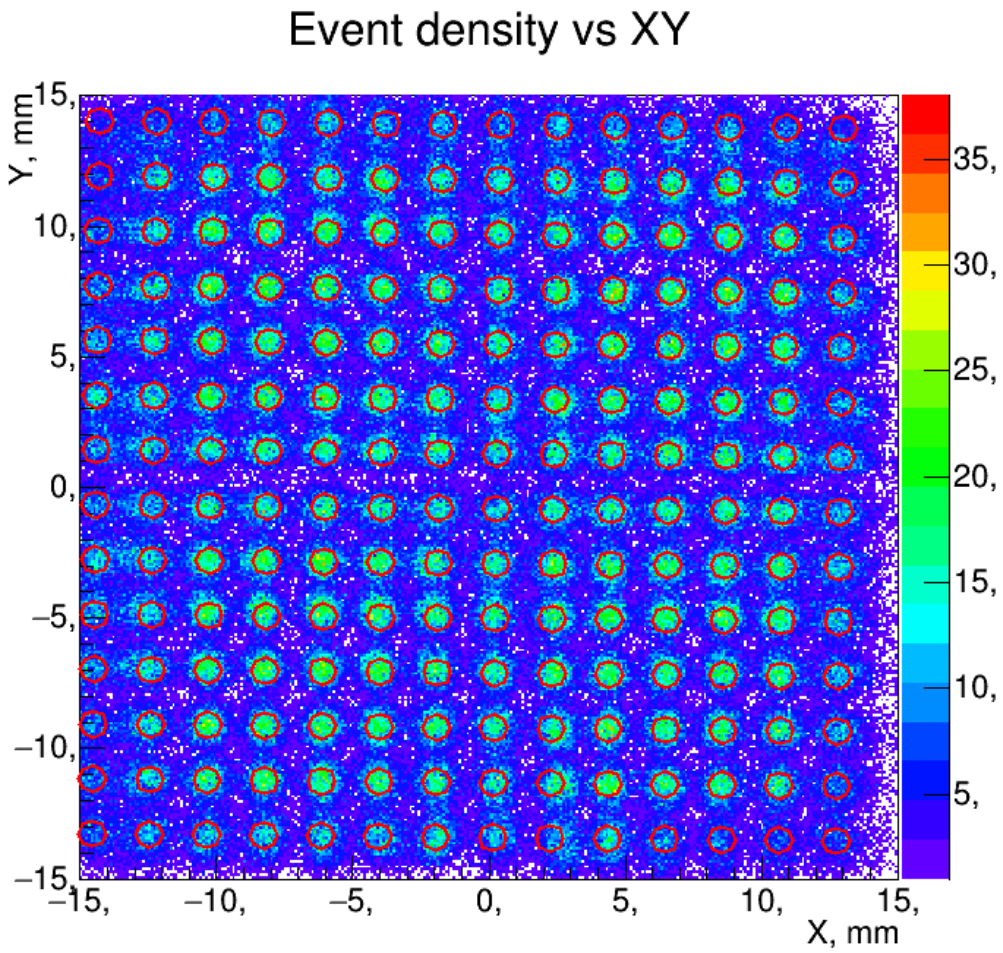


Figure 5.15: Experimental grid data, reconstructed with simulation LRFs (with gain correction), marked with radioactive source grid.

Chapter 6

# Compact gamma camera optimization

## 6.1 Overview

Before beginning the optimization procedure, it is necessary to define the desired characteristics of the compact gamma camera. The goal of this study is to:

- Achieve the highest possible spatial resolution. One of the objectives of this camera is to be useful in the inspection of small organs (for mice trials). Therefore, resolution must be better than 1.0 mm.
- Minimize position reconstruction bias (distortions), and therefore achieve acceptable linearity and uniformity. This requirement is related to the previous one, as the image blurring, due to finite resolution, masks smaller distortions. For the purpose of this study, a position reconstruction bias of up to 0.5 mm in any direction is considered acceptable.
- Maximize the useful field of view, which is considered to be the central area in which the above two conditions are fulfilled. It should be at least 75 % of the detector area.

I intend to optimize the lightguide thickness and to confirm that addition of the back reflector (PTFE layer) and application of the optical grease on the sides of the crystal and lightguide lead to improvements in the camera performance.

With a too thin lightguide, for scintillations close to the sensors (in Z axis), a minimal number of sensors is illuminated. Most have a very low signal and should be ignored in reconstruction. With less sensors contributing to reconstruction, the resulting image has a higher degree of distortions. On the other hand, for a too thick lightguide, average signals decrease so much that statistical fluctuations become very strong, which, in turn, lead to lower spatial resolution.

The scintillator should be as thin as possible, without compromising the interaction efficiency. This is both due to the intrinsic radiation of $^{176}$Lu, which produces background scintillation events, as well as the need to consider LRF dependency on the depth of interaction a negligible effect, since the ability to apply iterative reconstruction (only available for Axial type LRFs, see section 4.6) to the optimized camera is a requirement. With 2 mm, the scintillator can collect >75 % of incident gamma particles, at 140 keV (see figure 6.1), and it has been shown in chapter 5 that, for such thickness, depth of interactions are negligible for the purposes of this study.

Since resolution and distortions depend on position, the analysis was based on flood field simulations[1], and a rectangular grid with 2.0 mm pitch in both X and Y directions. Due to the camera symmetry, only one quarter of the field of view needs

[1]The events are uniformly distributed in the scintillator

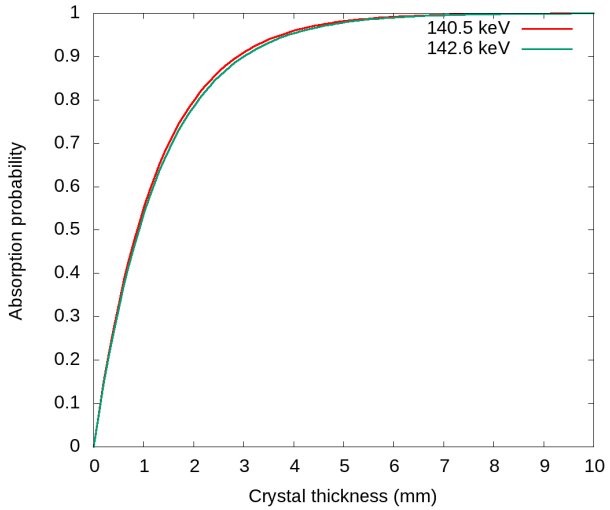


Figure 6.1: LYSO absorption probability vs thickness

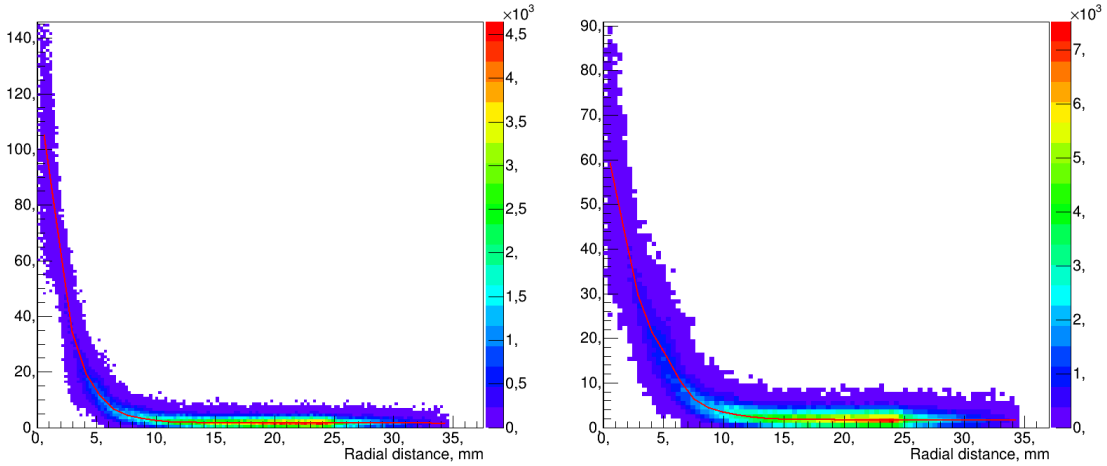


Figure 6.2: LRF fits of SiPM #14, located at (9.59 mm, 9.69 mm). **Left**: with 0.0 mm thick lightguide; **Right**: with 1.0 mm thick lightguide. Color-coded maps show the density map of events with the corresponding radial distance and the signal value.

to be analyzed. To take into account the scintillator thickness, for each node of the grid, $5 \times 10^3$ scintillation events were simulated. The events were equally distributed over five sub-nodes, from $-0.90$ mm to 0.90 mm in Z axis, with a 0.45 mm spacing. At each sub-node, 1000 events were simulated (point source, isotropic emission). Since the primary target of this study were 140 keV gamma particles, and a LYSO scintillator was used, 3500 ($25\,\text{keV}^{-1} \times 140\,\text{keV}$) optical photons were generated for each event.

LRF parameterization (see section 4.5) was of *Axial* type with 30 nodes (no compression), using *Square packing* grouping (possible, due to the camera X and Y symmetry), and were directly calculated using flood field simulation data containing $10^6$ events. The LRFs were parameterized without compression, since otherwise it would be required to adjust three additional parameters for each detector configu-

ration, leading to additional uncertainty in the final results. The number 30 is an estimation based on the LRF calculations of chapter 5: The most compressed spline nodes are 1 mm apart. Since our camera geometry is 30 mm × 30 mm, 30 nodes result in ≈1 mm spacing for most photosensors. Simulations with $2 \times 10^5$ events were also made, with no noticeable changes in results, indicating that there are enough statistics to allow for such high number of nodes. Figure 6.2 shows an example of two LRF fits: one for a detector without lightguide, and another for a detector with a 1.0 mm thick lightguide.

The ANTS2 script to generate all data in this chapter is presented in appendix B. This chapter is based purely on simulation data.

## 6.2 Basic detector

The basic detector consists of a model similar to the one simulated in chapter 5. However, it does not contain the PTFE layer, the respective optical coupling layer, and the material of the world object is air. As in the previous chapter, the term "lightguide thickness" refers to the thickness of the lightguide layer in table 5.1.

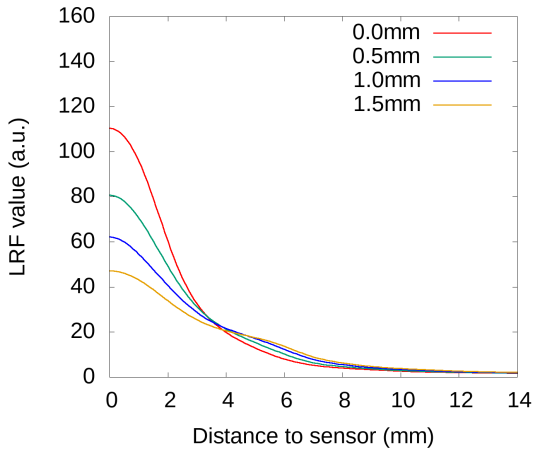


Figure 6.3: LRFs of SiPM #14, located at (9.59 mm, 9.69 mm), for detectors with lightguides of 0.0 mm, 0.5 mm, 1.0 mm, 1.5 mm, and 2.0 mm.

Figure 6.3 presents the LRFs of the sensor #14, located at (9.59 mm, 9.69 mm), for various lightguide thicknesses. As expected, the thicker the lightguide, the more scintillation light spreads across the SiPM array, resulting in wider LRFs with lower peak amplitude. Furthermore, for thicker lightguides, an additional structure appears in the LRF, near the 6 mm distance from origin, resulting in flattening of the LRF profile. In the following text I refer to this structure as the "bump". Note that the bump has negative effect on both resolution and level of distortions, as it will be apparent in the next chapter. The bump, most likely, appears due to full internal reflections on the scintillator.

Figure 6.4 shows the event density map for a detector with a 2.0 mm lightguide and table 6.5 shows the average (column "offset" – reconstruction bias) and FWHM (resolution) of a Gaussian fit to the distribution of the reconstructed events for several nodes of the grid. In them, is shown that several pairs of points (on the lower and the left sides of the figure) have to be at least 1.3 mm apart, to be distinguishable. The useful field of view is also significantly smaller (20 mm × 20 mm), since distortions approach 0.5 mm already at 10 mm from center (see figure 6.5, on the right). This does not meet our resolution nor field of view criteria, even though it contains nearly no distortions in the center. As such, only lightguide thicknesses up to 1.5 mm are presented.

Figure 6.6 shows maps of event density of the grid simulation, for lightguide of thicknesses 0.0 mm, 0.5 mm, 1.0 mm, and 1.5 mm. Tables 6.1, 6.2, 6.3, and 6.4 show the reconstruction bias and resolution for the same thicknesses, respectively. Is is shown that resolution is better for models with a thinner lightguide. However they also have larger distortions, as shown in figure 6.8, where the map of the average difference between the true and the reconstructed position is plotted vs the reconstructed position. Many of the grid nodes of the 0.5 mm lightguide are not round, an effect not present in the 1.0 mm lightguide. In fact, the level of distortions present with a lightguide of 0.5 mm thickness is unacceptable for our camera, since it is similar to the value of resolution in many central areas.

The 1.0 mm lightguide thickness is the optimum, with a **resolution** of ≈1.0 mm, and a **useful field of view** of 22 mm × 22 mm

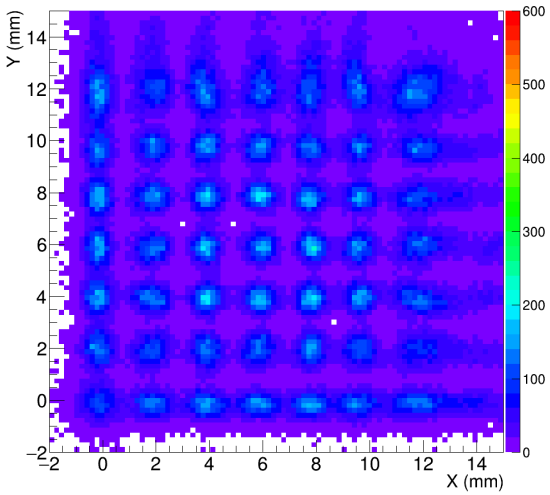


Figure 6.4: Event density for a basic detector with a 2.0 mm thick lightguide.

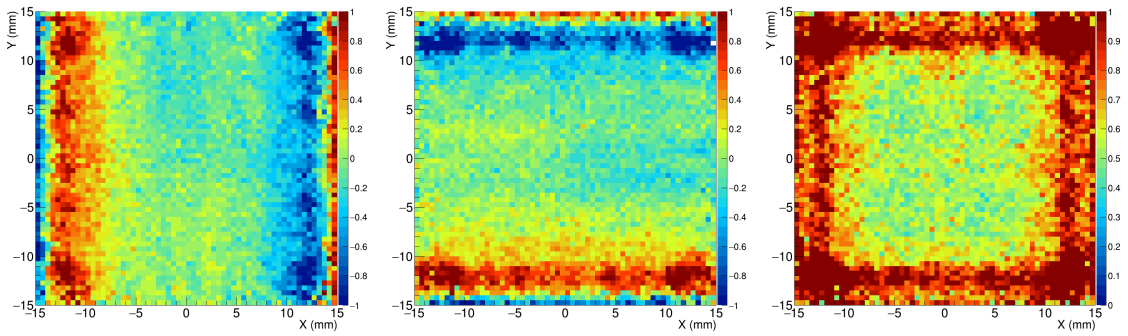


Figure 6.5: Distance between reconstructed and true position for a detector with a 2.0 mm thick lightguide. **Left**: in X axis; **Center**: in Y axis; **Right**: in both axis.

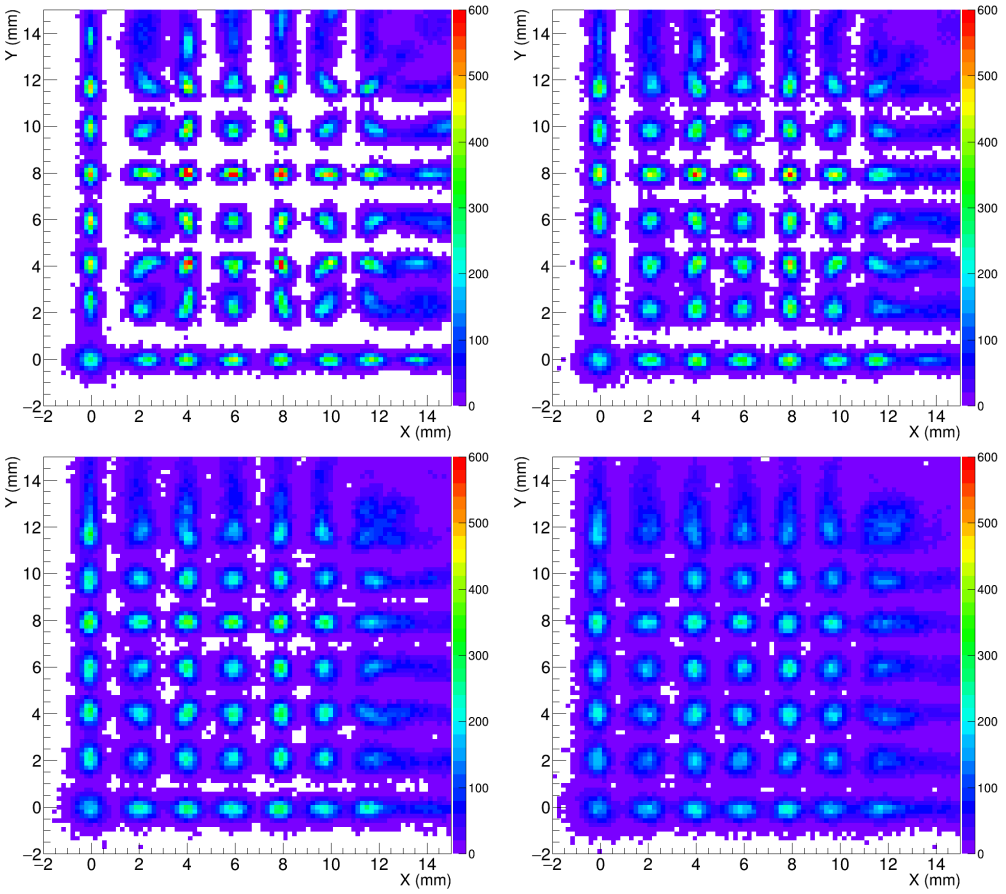


Figure 6.6: Event density maps for detectors with different lightguide thicknesses. **Top-left**: 0.00 mm; **Top-right**: 0.50 mm; **Bottom-left**: 1.00 mm; **Bottom-right**: 1.50 mm.

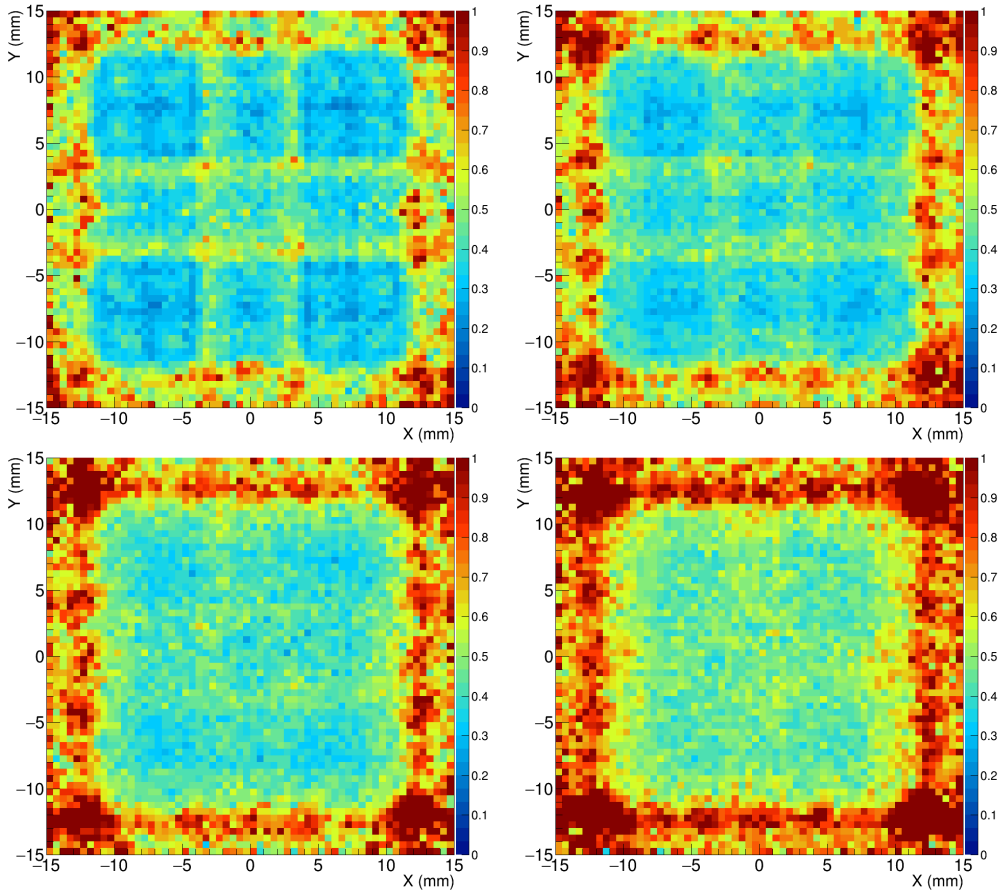


Figure 6.7: Distance between reconstructed and scintillation positions, for different lightguide thicknesses (from **Top** to **Bottom**): 0.00 mm, 0.50 mm, 1.00 mm, and 1.50 mm.

| Position | | Offset | | FWHM | |
|---|---|---|---|---|---|
| X/mm | Y/mm | X/mm | Y/mm | X/mm | Y/mm |
| 0.00 | 0.00 | −0.0351 | −0.0278 | 0.7480 | 0.6802 |
| 2.00 | 0.00 | +0.2610 | −0.0387 | 0.9363 | 0.4458 |
| 2.00 | 2.00 | +0.2664 | +0.3374 | 0.8178 | 0.8349 |
| 4.00 | 0.00 | +0.0143 | −0.0512 | 0.6846 | 0.4320 |
| 8.00 | 8.00 | −0.0674 | −0.0571 | 0.3734 | 0.3376 |
| 8.00 | 10.00 | −0.0724 | −0.1223 | 0.3922 | 0.6055 |
| 8.00 | 12.00 | −0.0643 | −0.2240 | 0.4005 | 0.5572 |

Table 6.1: Resolution of the basic detector for a 0.0 mm lightguide.

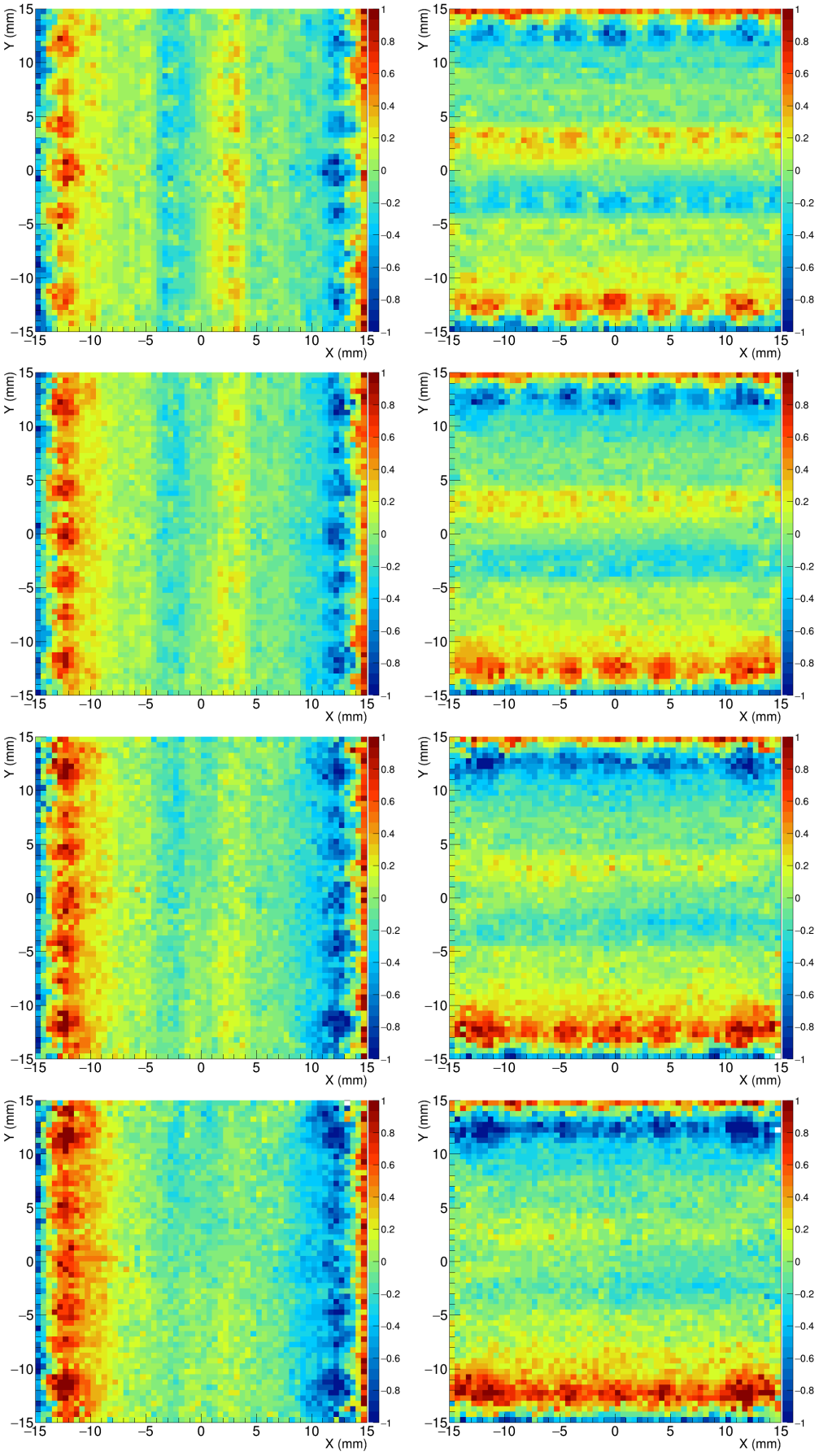


Figure 6.8: Difference between reconstructed and scintillation positions, for different lightguide thicknesses (from **Top** to **Bottom**): 0.00 mm, 0.50 mm, 1.00 mm, and 1.50 mm. **Left**: in X axis; **Right**: in Y axis.

| Position | | Offset | | FWHM | |
|---|---|---|---|---|---|
| X/mm | Y/mm | X/mm | Y/mm | X/mm | Y/mm |
| 0.00 | 0.00 | −0.0456 | −0.0442 | 0.8117 | 0.7472 |
| 2.00 | 0.00 | +0.0792 | −0.0536 | 0.9525 | 0.5088 |
| 2.00 | 2.00 | +0.0931 | +0.1537 | 0.7837 | 0.7522 |
| 4.00 | 0.00 | +0.0464 | −0.0688 | 0.7436 | 0.5126 |
| 8.00 | 8.00 | −0.0860 | −0.0729 | 0.4631 | 0.4314 |
| 8.00 | 10.00 | −0.0872 | −0.1744 | 0.4604 | 0.6395 |
| 8.00 | 12.00 | −0.0772 | −0.2095 | 0.4901 | 0.7720 |

Table 6.2: Resolution of the basic detector for a 0.5 mm lightguide.

| Position | | Offset | | FWHM | |
|---|---|---|---|---|---|
| X/mm | Y/mm | X/mm | Y/mm | X/mm | Y/mm |
| 0.00 | 0.00 | −0.0564 | −0.0429 | 0.8845 | 0.8909 |
| 2.00 | 0.00 | +0.0438 | −0.0865 | 0.9504 | 0.6198 |
| 2.00 | 2.00 | −0.0159 | +0.0402 | 0.8633 | 0.8510 |
| 4.00 | 0.00 | +0.0013 | −0.0970 | 0.8425 | 0.6154 |
| 8.00 | 8.00 | −0.1355 | −0.1192 | 0.5751 | 0.5784 |
| 8.00 | 10.00 | −0.1195 | −0.2222 | 0.5616 | 0.7435 |
| 8.00 | 12.00 | −0.1068 | −0.2167 | 0.5934 | 0.9773 |

Table 6.3: Resolution of the basic detector for a 1.0 mm lightguide.

| Position | | Offset | | FWHM | |
|---|---|---|---|---|---|
| X/mm | Y/mm | X/mm | Y/mm | X/mm | Y/mm |
| 0.00 | 0.00 | −0.0910 | −0.0564 | 1.0426 | 1.0095 |
| 2.00 | 0.00 | −0.0139 | −0.1078 | 1.0794 | 0.7590 |
| 2.00 | 2.00 | −0.1075 | −0.0420 | 1.0237 | 0.9866 |
| 4.00 | 0.00 | −0.0247 | −0.1259 | 0.9875 | 0.7150 |
| 8.00 | 8.00 | −0.1765 | −0.1642 | 0.7101 | 0.7389 |
| 8.00 | 10.00 | −0.1537 | −0.2424 | 0.7025 | 0.8880 |
| 8.00 | 12.00 | −0.1618 | −0.2470 | 0.7468 | 1.1310 |

Table 6.4: Resolution of the basic detector for a 1.5 mm lightguide.

| Position | | Offset | | FWHM | |
|---|---|---|---|---|---|
| X/mm | Y/mm | X/mm | Y/mm | X/mm | Y/mm |
| 0.00 | 0.00 | −0.1203 | −0.1077 | 1.2662 | 1.2348 |
| 2.00 | 0.00 | −0.0817 | −0.1557 | 1.2683 | 0.9255 |
| 2.00 | 2.00 | −0.1733 | −0.1061 | 1.1445 | 1.1504 |
| 4.00 | 0.00 | −0.0656 | −0.1632 | 1.1495 | 0.8666 |
| 8.00 | 8.00 | −0.2230 | −0.2145 | 0.8840 | 0.9002 |
| 8.00 | 10.00 | −0.1926 | −0.2860 | 0.9355 | 1.0787 |
| 8.00 | 12.00 | −0.1764 | −0.2694 | 0.9759 | 1.3476 |

Table 6.5: Resolution of the basic detector for a 2.0 mm lightguide.

## 6.3 Scintillator and lightguide covered in optical grease

In the previous section, the reconstruction area was effectively reduced to a range of 22 mm × 22 mm. By covering the scintillator and lightguide with optical grease, the amount of full internal reflections is reduced, due to the refractive index of optical grease being closer to that of the scintillator and lightguide, than to that of air. This should improve the axial symmetry of the detector, and consequently of the LRFs, especially at the periphery of the detector.

Note that what was simulated was not a thin layer of optical grease, but a very thick one. Specifically, the "world" object material was optical grease. The real-world equivalent is to submerge the detector in a black box filled with optical grease, or more practicaly, to do as in section 5.1.1: putting light absorbing material in the optical grease layer.

As a result of this change, the bump in the LRFs of sensor #14 (see figure 6.9) is no longer noticeable. This confirms the expectation of the previous section, that it was caused by full internal reflections from crystal surfaces.

There were significant improvements on the sides of the detector, especially in the corners, since the closest nodes to the sides are distinguishable from their neighboring nodes, as shown in figure 6.10. Furthermore, there are no $>1$ mm nor $<-1$ mm areas in figure 6.12. However, an exception to this is the 0.0 mm thick lightguide, in which case the central area, as well as the areas near coordinates (0 mm, −15 mm), (0 mm, 15 mm), (−15 mm, 0 mm), and (15 mm, 0 mm), have a very high degree of distortions. The distortions in the mentioned non-central areas are also visible for other lightguide thicknesses, but when compared to the basic model, they still show improvements. This effect suggests that the light that escaped through the lower side of the scintillator would have significantly improved the photosensors statistics of that event. Indeed, with the thinner lightguide, scintillations in the central area

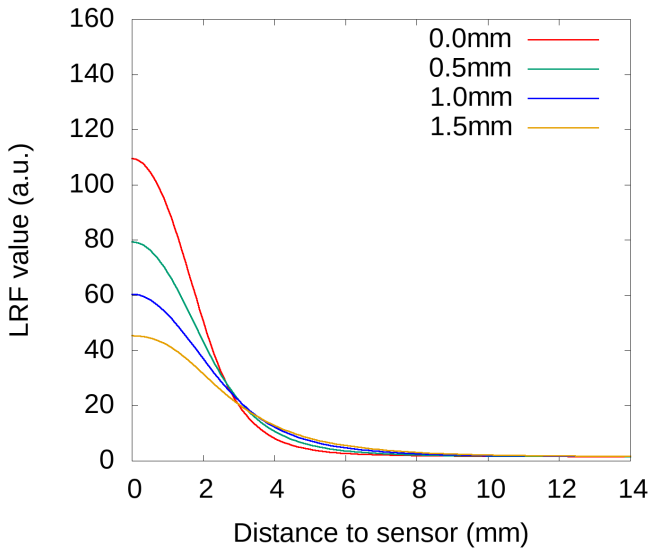


Figure 6.9: LRFs of SiPM #14 for detectors with lightguides of 0.0 mm, 0.5 mm, 1.0 mm, 1.5 mm, and 2.0 mm.

| Position | | Offset | | FWHM | |
|---|---|---|---|---|---|
| X/mm | Y/mm | X/mm | Y/mm | X/mm | Y/mm |
| 0.00 | 0.00 | −0.0208 | −0.0125 | 0.6542 | 0.6208 |
| 2.00 | 0.00 | +0.1489 | −0.7693 | 1.6541 | 0.0003 |
| 2.00 | 2.00 | +0.2597 | +0.2613 | 1.0542 | 1.1604 |
| 4.00 | 0.00 | +0.0388 | −0.0304 | 0.6671 | 0.4015 |
| 8.00 | 8.00 | +0.0128 | −0.0105 | 0.3962 | 0.2955 |
| 8.00 | 10.00 | −0.0077 | −0.0331 | 0.3617 | 0.5211 |
| 8.00 | 12.00 | +0.0354 | +0.0268 | 0.4474 | 0.7671 |

Table 6.6: Resolution of the detector with scintillator and lightguide covered in optical grease, for a 0.0 mm lightguide.

do not spread enough, and there is no photosensor directly on top. This will be considered in the next section.

For this section, a lightguide thickness of 1.0 mm is still the most balanced choice, with a **resolution** of ≈0.8 mm, and a **useful field of view** of 23 mm × 23 mm. Reducing full internal reflections on the edges of the detector does enhance the useful field of view of the detector.

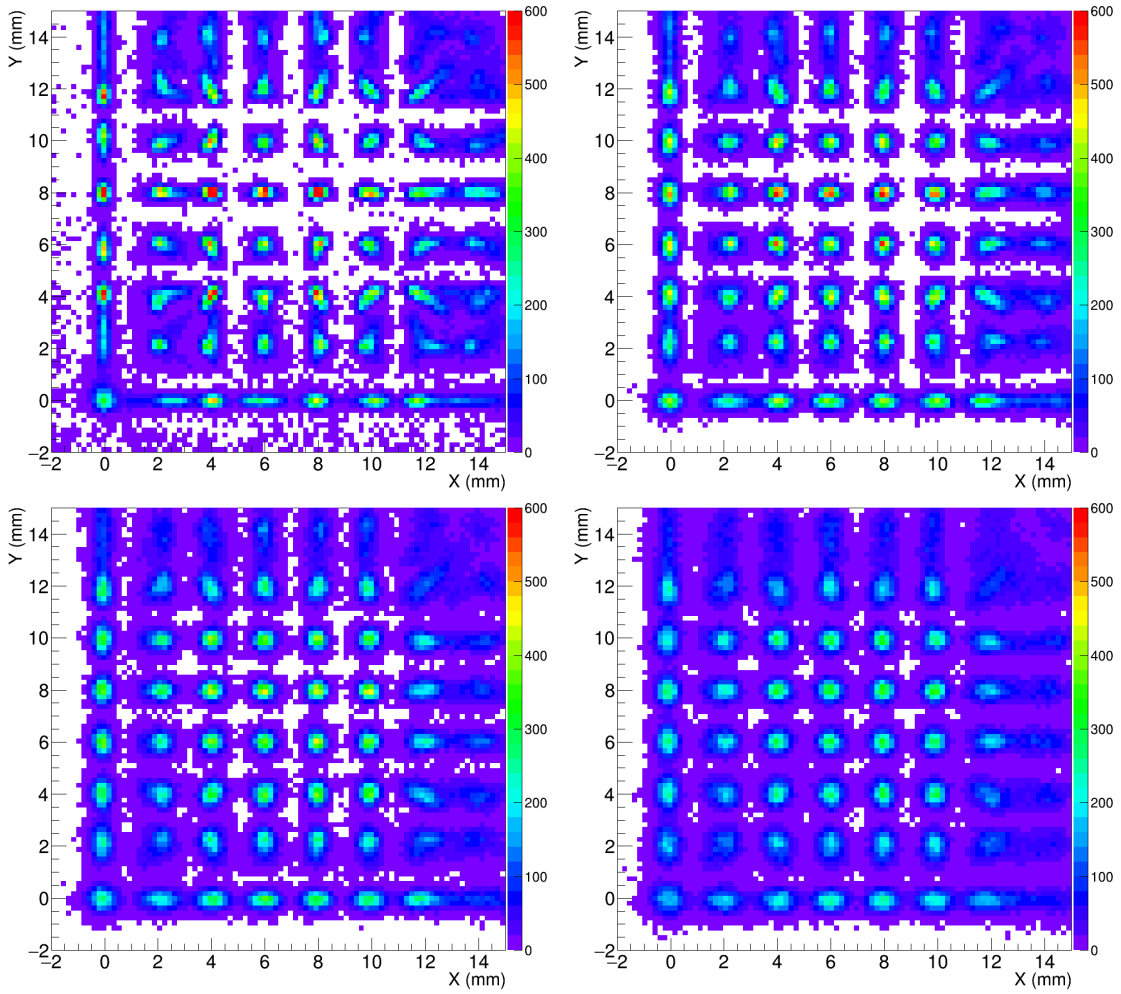


Figure 6.10: Event density maps for detectors with different lightguide thicknesses. **Top-left**: 0.00 mm; **Top-right**: 0.50 mm; **Bottom-left**: 1.00 mm; **Bottom-right**: 1.50 mm.

| Position | | Offset | | FWHM | |
|---|---|---|---|---|---|
| X/mm | Y/mm | X/mm | Y/mm | X/mm | Y/mm |
| 0.00 | 0.00 | −0.0345 | −0.0342 | 0.6352 | 0.5851 |
| 2.00 | 0.00 | +0.2052 | −0.0463 | 1.2137 | 0.4700 |
| 2.00 | 2.00 | +0.1550 | +0.1591 | 0.9430 | 1.0018 |
| 4.00 | 0.00 | +0.0401 | −0.0543 | 0.7577 | 0.4438 |
| 8.00 | 8.00 | −0.0298 | −0.0243 | 0.4358 | 0.3942 |
| 8.00 | 10.00 | −0.0414 | −0.0602 | 0.4182 | 0.5099 |
| 8.00 | 12.00 | −0.0009 | −0.0458 | 0.4668 | 0.7673 |

Table 6.7: Resolution of the detector with scintillator and lightguide covered in optical grease, for a 0.5 mm lightguide.

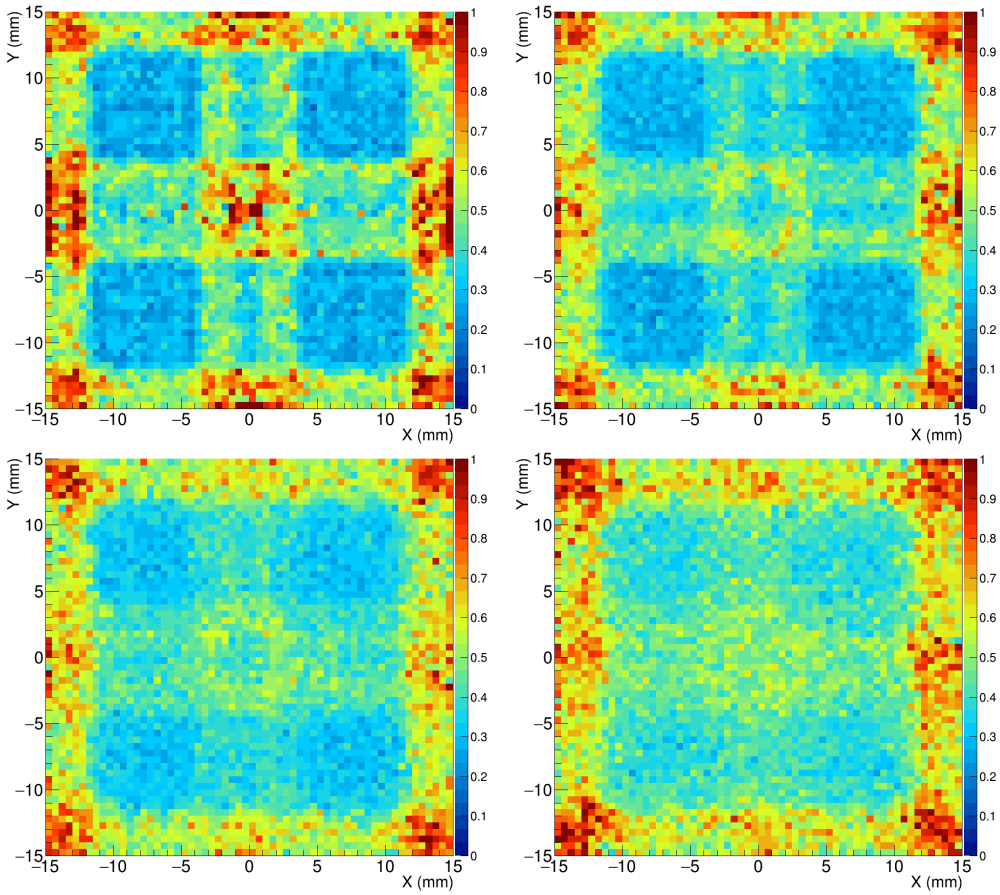


Figure 6.11: Distance between reconstructed and scintillation positions, for different lightguide thicknesses (from **Top** to **Bottom**): 0.00 mm, 0.50 mm, 1.00 mm, and 1.50 mm.

| Position | | Offset | | FWHM | |
|---|---|---|---|---|---|
| X/mm | Y/mm | X/mm | Y/mm | X/mm | Y/mm |
| 0.00 | 0.00 | −0.0587 | −0.0377 | 0.7764 | 0.7149 |
| 2.00 | 0.00 | +0.0924 | −0.0593 | 1.1421 | 0.5768 |
| 2.00 | 2.00 | +0.0395 | +0.0638 | 0.9695 | 1.0704 |
| 4.00 | 0.00 | +0.0468 | −0.0716 | 0.8728 | 0.5303 |
| 8.00 | 8.00 | −0.0406 | −0.0261 | 0.5255 | 0.4893 |
| 8.00 | 10.00 | −0.0401 | −0.0686 | 0.5140 | 0.5564 |
| 8.00 | 12.00 | −0.0110 | −0.0758 | 0.5701 | 0.8423 |

Table 6.8: Resolution of the detector with scintillator and lightguide covered in optical grease, for a 1.0 mm lightguide.

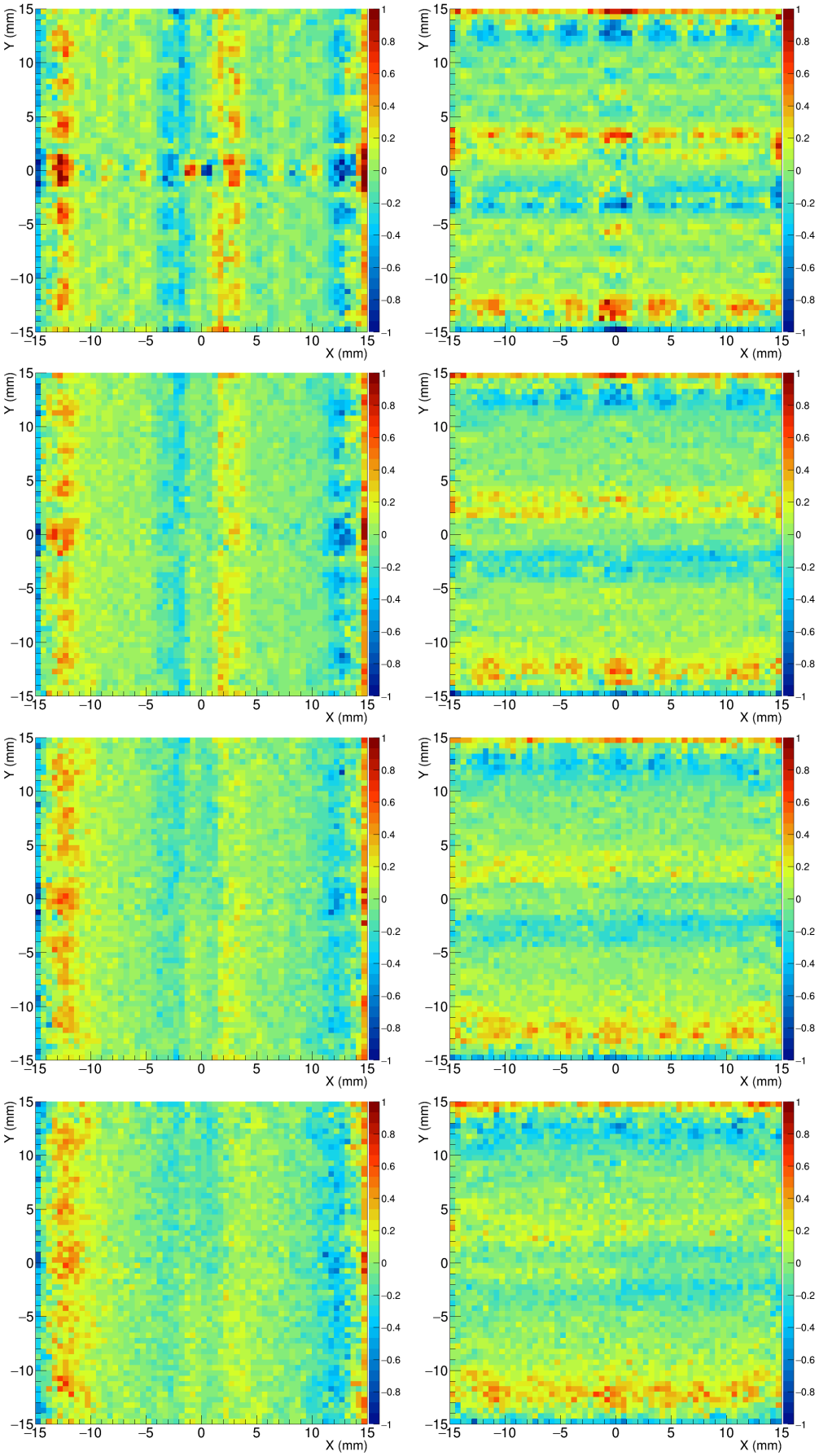


Figure 6.12: Difference between reconstructed and scintillation positions, for different lightguide thicknesses (from **Top** to **Bottom**): 0.00 mm, 0.50 mm, 1.00 mm, and 1.50 mm. **Left**: in X axis; **Right**: in Y axis.

| Position | | Offset | | FWHM | |
|---|---|---|---|---|---|
| X/mm | Y/mm | X/mm | Y/mm | X/mm | Y/mm |
| 0.00 | 0.00 | −0.0639 | −0.0457 | 0.9279 | 0.8698 |
| 2.00 | 0.00 | +0.0074 | −0.0973 | 1.1483 | 0.7176 |
| 2.00 | 2.00 | −0.0449 | −0.0071 | 1.0539 | 1.0937 |
| 4.00 | 0.00 | +0.0570 | −0.0986 | 0.9986 | 0.6560 |
| 8.00 | 8.00 | −0.0403 | −0.0283 | 0.6166 | 0.6219 |
| 8.00 | 10.00 | −0.0640 | −0.0909 | 0.6167 | 0.6478 |
| 8.00 | 12.00 | −0.0275 | −0.1185 | 0.7251 | 0.9895 |

Table 6.9: Resolution of the detector with scintillator and lightguide covered in optical grease, for a 1.5 mm lightguide.

## 6.4 PTFE backplate

In the previous section, covering the scintillator and lightguide with optical grease improved the image reconstruction near the sides, while slightly increasing distortions in the central area. Since the optical grease effect is to allow light to escape the detector, instead of redoing the simulations without optical grease on the lower side of the scintillator, the opposite effect is introduced: the addition of a backplate of a material with a very high diffusive reflectivity (PTFE). The material was placed on the lower side of the scintillator crystal, coupled with optical grease. It reflects 95 % of incident light according to Lambert's law.

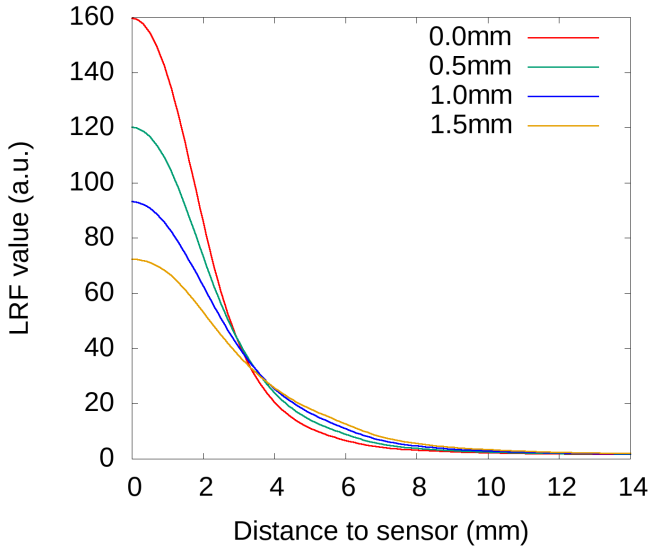


Figure 6.13: LRFs of SiPM #14 for detectors with lightguides of 0.0 mm, 0.5 mm, 1.0 mm, 1.5 mm, and 2.0 mm.

This reflection should improve statistics. A scintillation event emits light isotropically in $4\pi$, which means a significant amount of emitted light illuminates the PTFE backplate. In turn, the backplate will diffusely reflect 95 % of incident light, which

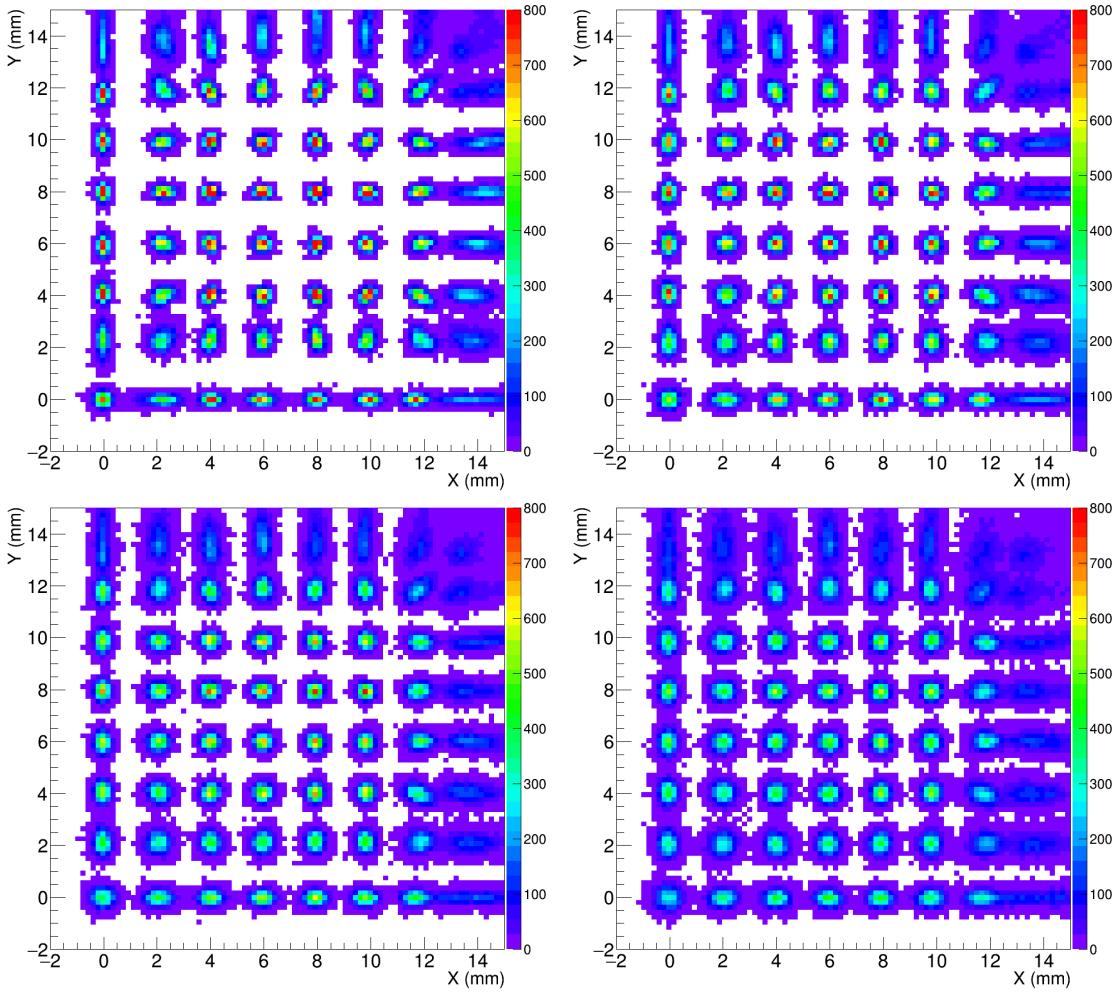


Figure 6.14: Event density maps for detectors with different lightguide thicknesses. **Top-left**: 0.00 mm; **Top-right**: 0.50 mm; **Bottom-left**: 1.00 mm; **Bottom-right**: 1.50 mm.

will appear to the sensors as a scintillation (not necessarily a point source one) occurring on the lower side of the scintillator, with peak intensity in the same projected position as the original scintillation, but illuminating more sensors. This should both increase the peak and extend the useful range of the LRFs, which figure 6.13 confirms.

Figure 6.17 shows that the bump is nearly unnoticeable, so an extended useful field of view, comparing to a detector without the PTFE backplate, is expected. Furthermore, from the higher LRF peak and extended useful range, an improved spatial resolution, and less distortions are also expected, which is confirmed by both figures 6.14 and 6.16[2].

[2]Note the change of scale of figure 6.16 compared to similar ones, earlier in this chapter.

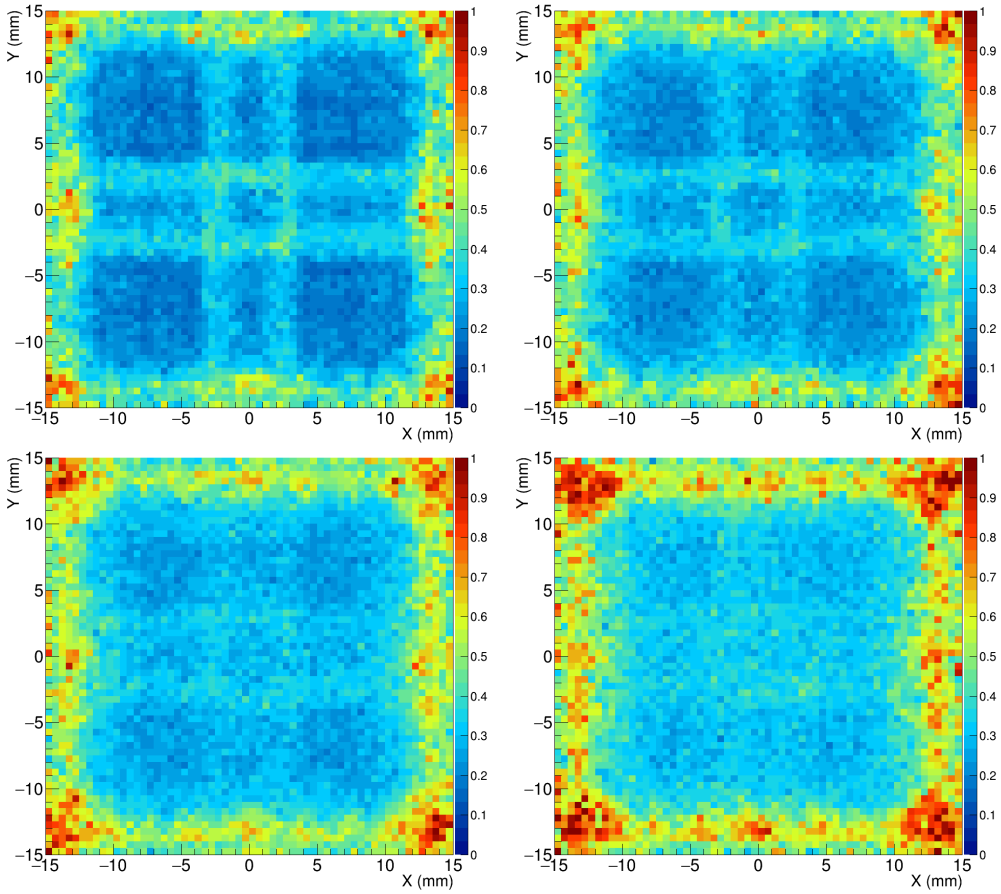


Figure 6.15: Distance between reconstructed and scintillation positions, for different lightguide thicknesses (from **Top** to **Bottom**): 0.00 mm, 0.50 mm, 1.00 mm, and 1.50 mm.

The effect of changing the lightguide thickness is significantly reduced, as shown in figure 6.14. Nevertheless, figure 6.16 shows that a lightguide thickness of 1.0 mm is still the optimum choice, with a **resolution** of 0.6 mm, and a **useful field of view** of 24 mm × 24 mm. Unlike surrounding the detector in optical grease, the addition a PTFE backplate provides significant improvements for all optimization parameters, with no downsides.

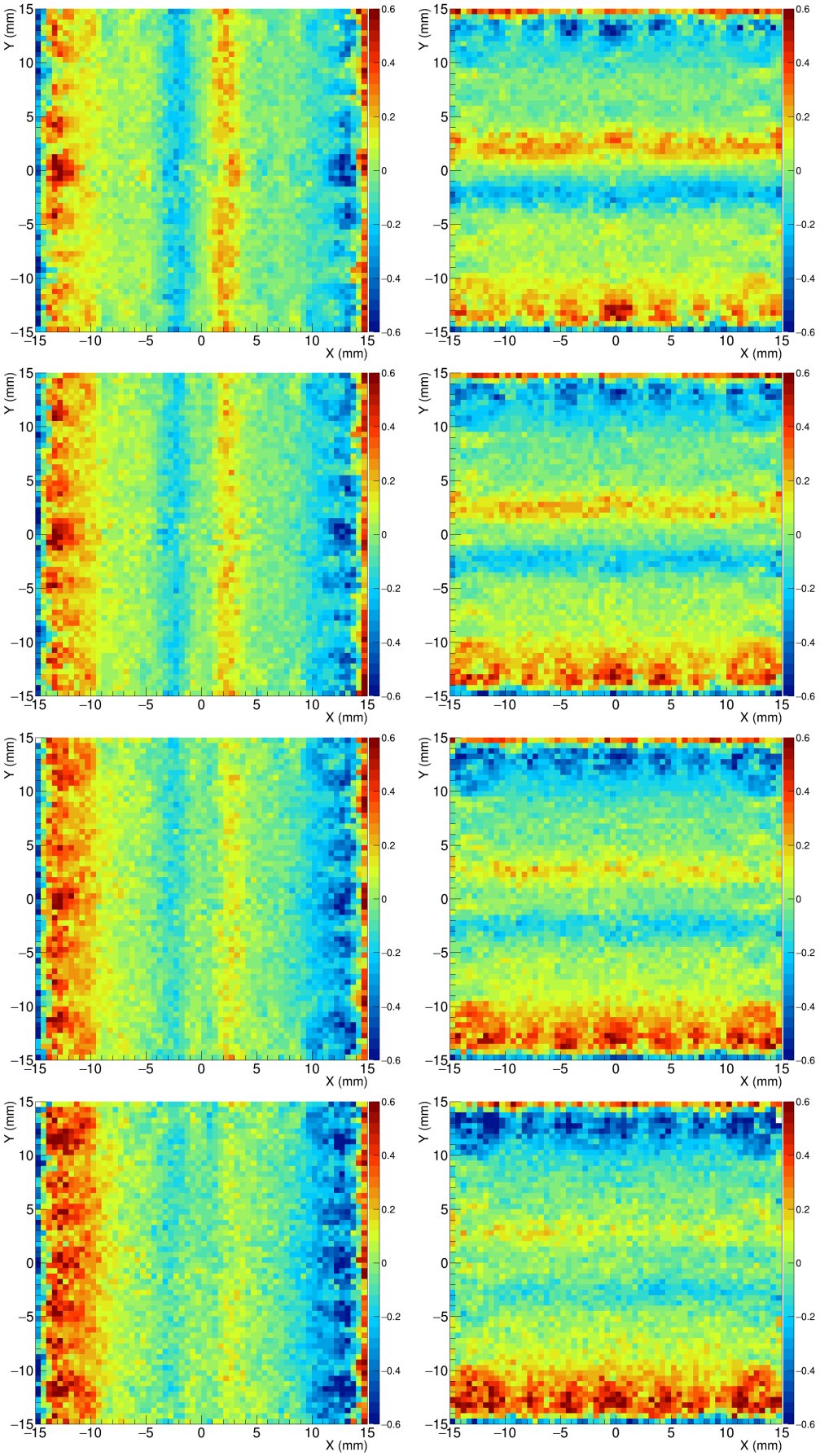


Figure 6.16: Difference between reconstructed and scintillation positions, for different lightguide thicknesses (from **Top** to **Bottom**): 0.00 mm, 0.50 mm, 1.00 mm, and 1.50 mm. **Left**: in X axis; **Right**: in Y axis. Note the scale reduction, from 1 to 0.6, when comparing to previous figures.

| Position | | Offset | | FWHM | |
|---|---|---|---|---|---|
| X/mm | Y/mm | X/mm | Y/mm | X/mm | Y/mm |
| 0.00 | 0.00 | −0.0157 | −0.0155 | 0.4506 | 0.4122 |
| 2.00 | 0.00 | +0.1749 | −0.0173 | 0.9810 | 0.3133 |
| 2.00 | 2.00 | +0.2196 | +0.2667 | 0.5925 | 0.6045 |
| 4.00 | 0.00 | +0.0460 | −0.0136 | 0.5102 | 0.2995 |
| 8.00 | 8.00 | −0.0349 | −0.0265 | 0.2942 | 0.2614 |
| 8.00 | 10.00 | −0.0406 | −0.0864 | 0.2882 | 0.3473 |
| 8.00 | 12.00 | −0.0063 | −0.1291 | 0.3245 | 0.4485 |

Table 6.10: Resolution of the detector with PTFE backplate, for a 0.0 mm lightguide.

| Position | | Offset | | FWHM | |
|---|---|---|---|---|---|
| X/mm | Y/mm | X/mm | Y/mm | X/mm | Y/mm |
| 0.00 | 0.00 | −0.0110 | −0.0147 | 0.5113 | 0.4722 |
| 2.00 | 0.00 | +0.1220 | −0.0249 | 0.7122 | 0.3638 |
| 2.00 | 2.00 | +0.1252 | +0.1716 | 0.5725 | 0.5976 |
| 4.00 | 0.00 | +0.0509 | −0.0219 | 0.5528 | 0.3525 |
| 8.00 | 8.00 | −0.0608 | −0.0370 | 0.3409 | 0.3259 |
| 8.00 | 10.00 | −0.0705 | −0.1019 | 0.3378 | 0.3727 |
| 8.00 | 12.00 | −0.0390 | −0.1435 | 0.3705 | 0.5176 |

Table 6.11: Resolution of the detector with PTFE backplate, for a 0.5 mm lightguide.

| Position | | Offset | | FWHM | |
|---|---|---|---|---|---|
| X/mm | Y/mm | X/mm | Y/mm | X/mm | Y/mm |
| 0.00 | 0.00 | −0.0224 | −0.0174 | 0.6159 | 0.5621 |
| 2.00 | 0.00 | +0.0765 | −0.0318 | 0.7363 | 0.4429 |
| 2.00 | 2.00 | +0.0622 | +0.1066 | 0.6201 | 0.6372 |
| 4.00 | 0.00 | +0.0193 | −0.0326 | 0.6158 | 0.4165 |
| 8.00 | 8.00 | −0.0814 | −0.0633 | 0.4004 | 0.4098 |
| 8.00 | 10.00 | −0.0874 | −0.1392 | 0.4175 | 0.4301 |
| 8.00 | 12.00 | −0.0674 | −0.1581 | 0.4431 | 0.6107 |

Table 6.12: Resolution of the detector with PTFE backplate, for a 1.0 mm lightguide.

| Position | | Offset | | FWHM | |
|---|---|---|---|---|---|
| X/mm | Y/mm | X/mm | Y/mm | X/mm | Y/mm |
| 0.00 | 0.00 | −0.0323 | −0.0324 | 0.7070 | 0.6565 |
| 2.00 | 0.00 | +0.0131 | −0.0470 | 0.7550 | 0.5149 |
| 2.00 | 2.00 | +0.0019 | +0.0329 | 0.6879 | 0.6878 |
| 4.00 | 0.00 | +0.0106 | −0.0553 | 0.6928 | 0.4880 |
| 8.00 | 8.00 | −0.0990 | −0.0900 | 0.4698 | 0.4755 |
| 8.00 | 10.00 | −0.0983 | −0.1526 | 0.4771 | 0.4941 |
| 8.00 | 12.00 | −0.0784 | −0.1602 | 0.5426 | 0.7314 |

Table 6.13: Resolution of the detector with PTFE backplate, for a 1.5 mm lightguide.

## 6.5 Scintillator and lightguide covered with optical grease, with PTFE backplate

Covering the scintillator and lightguide with optical grease also presented disadvantages, but they could be counter-balanced by placing a PTFE backplate on the lower side of the scintillator. On the other hand, just by placing the backplate the detector performance dramatically improved. This section intends to verify that the effect is cumulative.

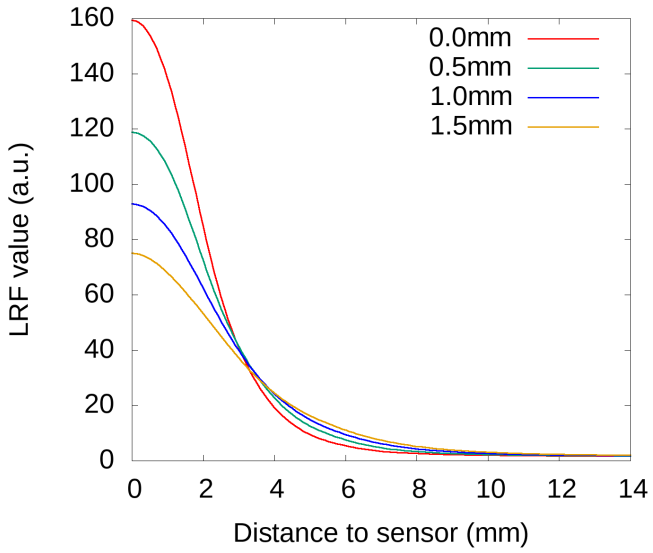


Figure 6.17: LRFs of SiPM #14 for detectors with lightguides of 0.0 mm, 0.5 mm, 1.0 mm, 1.5 mm, and 2.0 mm.

As figure 6.17 shows, the LRFs of this model are very similar to the ones of the model with just the PTFE backplate. Closer inspection of figure 6.21 shows that there is no trace of the (already small) bump that was present in the PTFE model. There are no other significant differences. As such, this is expected to slightly improve spatial resolution and reduce distortions near the borders, without

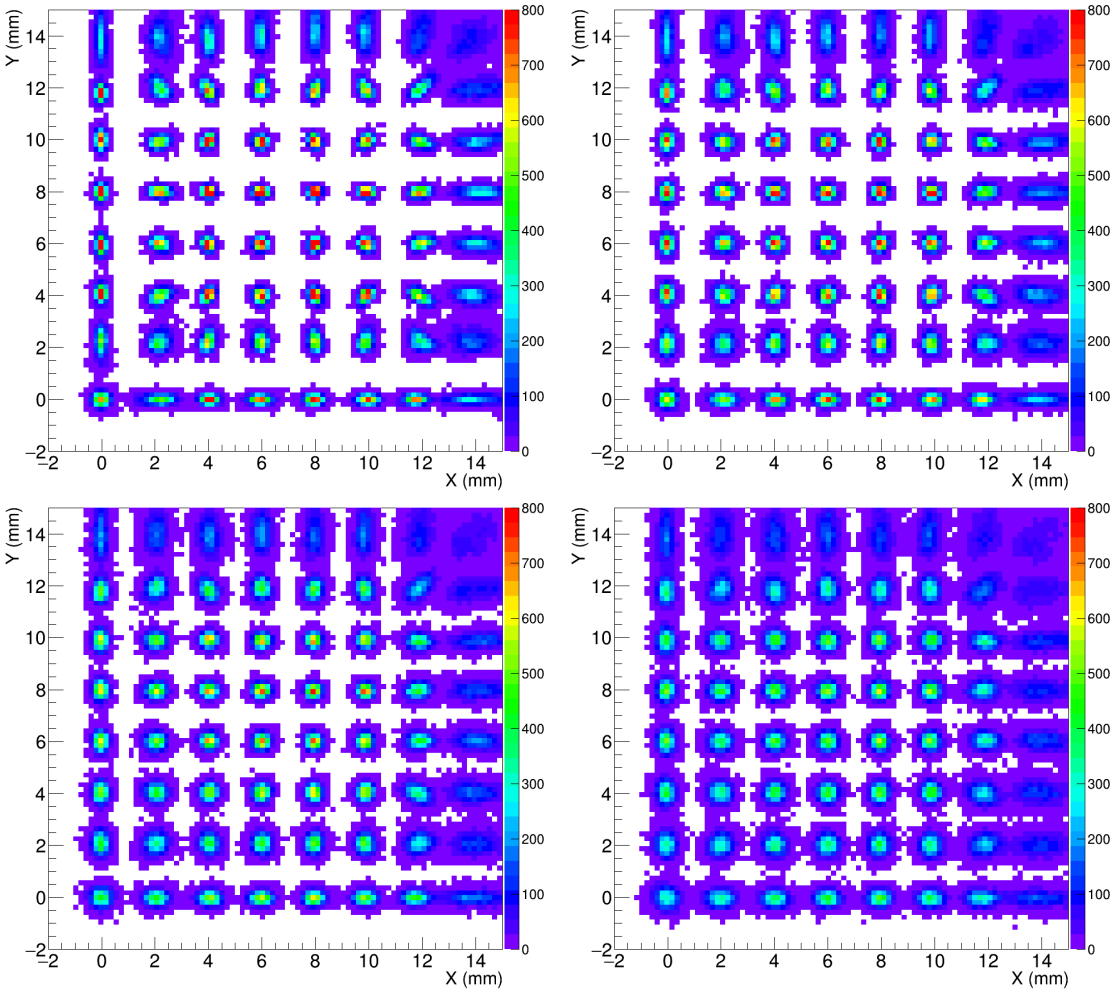


Figure 6.18: Event density maps for detectors with different lightguide thicknesses. **Top-left**: 0.00 mm; **Top-right**: 0.50 mm; **Bottom-left**: 1.00 mm; **Bottom-right**: 1.50 mm.

any compromise in the central area. Figures 6.18 and 6.20 confirm the expectations, especially in the corners.

In this case, the optimum lightguide thickness is 0.5 mm, with a **resolution** of 0.5 mm, and a **useful field of view** of 28 mm × 28 mm.

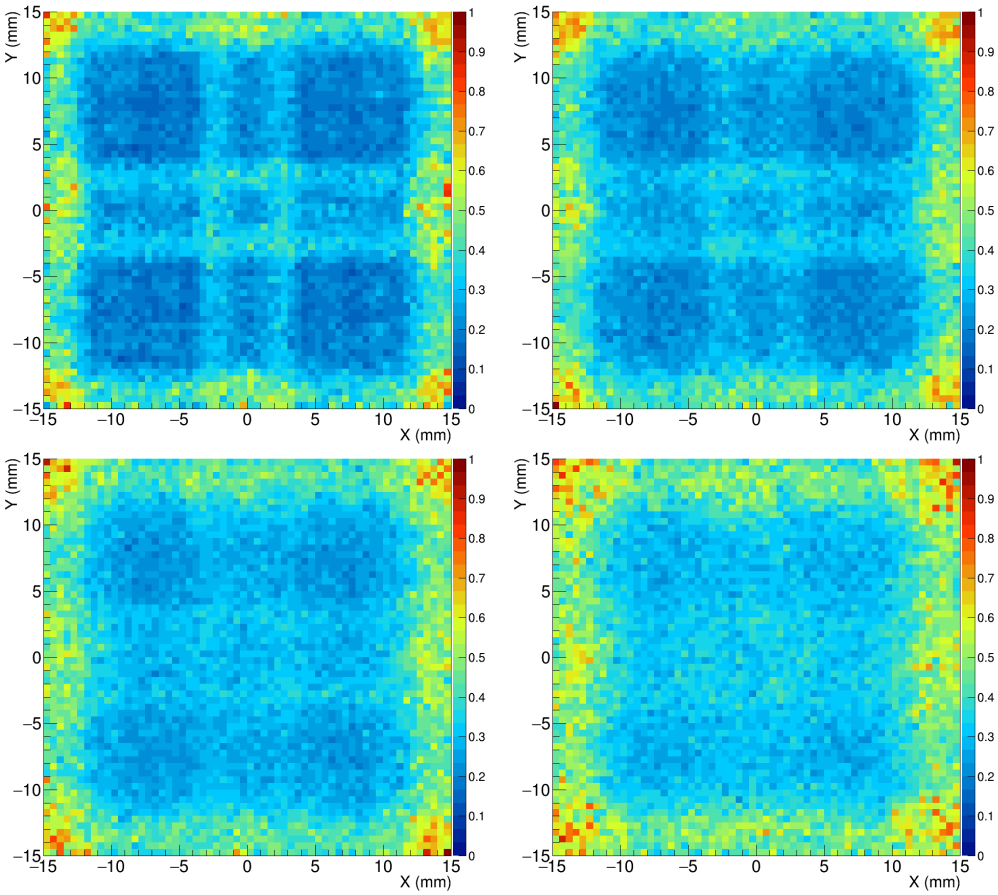


Figure 6.19: Distance between reconstructed and scintillation positions, for different lightguide thicknesses (from **Top** to **Bottom**): 0.00 mm, 0.50 mm, 1.00 mm, and 1.50 mm.

| Position | | Offset | | FWHM | |
|---|---|---|---|---|---|
| X/mm | Y/mm | X/mm | Y/mm | X/mm | Y/mm |
| 0.00 | 0.00 | −0.0080 | −0.0117 | 0.4628 | 0.4228 |
| 2.00 | 0.00 | +0.1651 | −0.0141 | 0.9100 | 0.3066 |
| 2.00 | 2.00 | +0.1849 | +0.2193 | 0.5644 | 0.5922 |
| 4.00 | 0.00 | +0.0392 | −0.0134 | 0.5018 | 0.2894 |
| 8.00 | 8.00 | −0.0180 | −0.0207 | 0.2896 | 0.2586 |
| 8.00 | 10.00 | −0.0168 | −0.0592 | 0.2981 | 0.3688 |
| 8.00 | 12.00 | +0.0034 | −0.0794 | 0.3228 | 0.4689 |

Table 6.14: Resolution of the detector with scintillator and lightguide covered in optical grease, with a PTFE backplate, for a 0.0 mm lightguide.

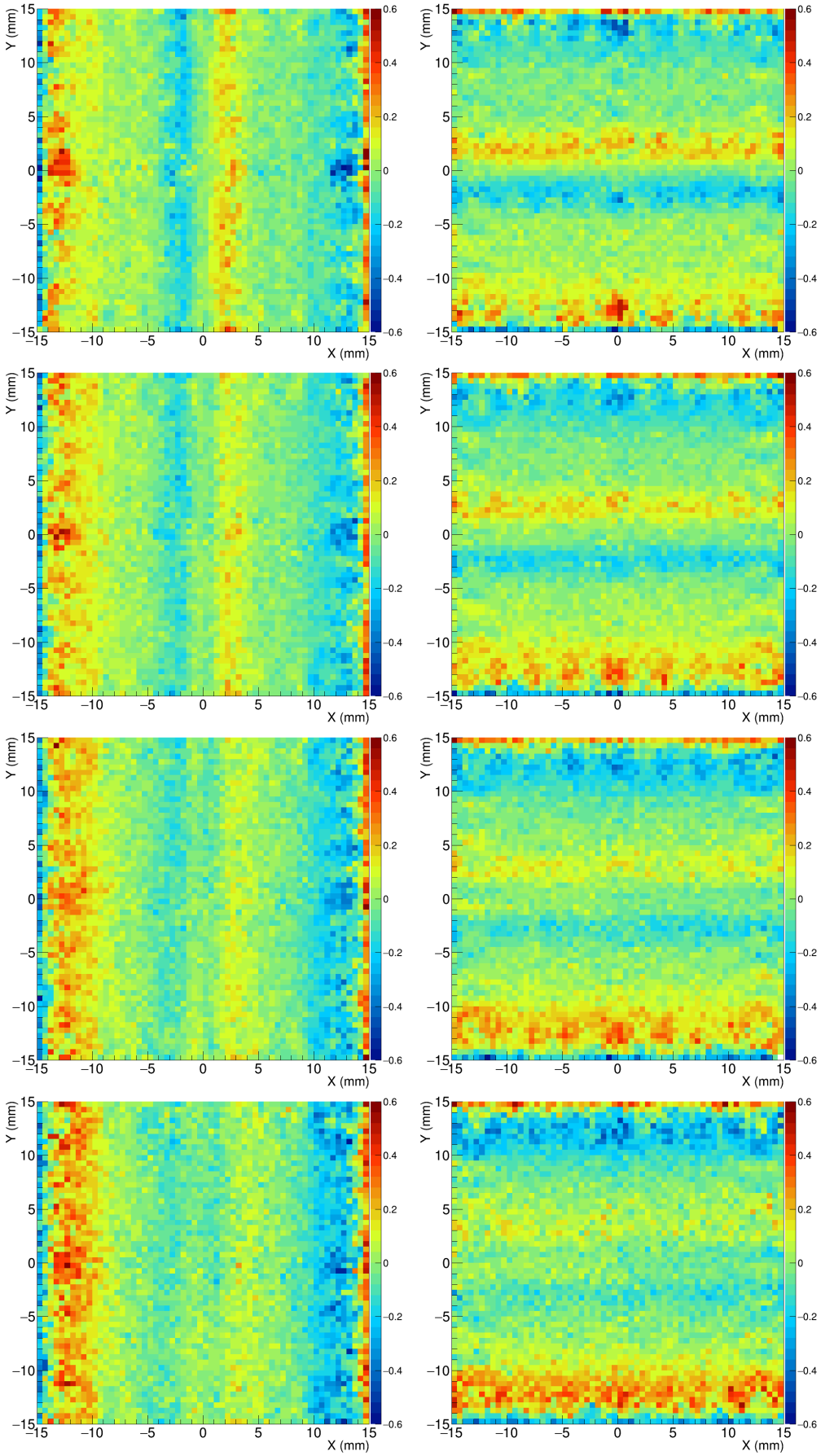


Figure 6.20: Difference between reconstructed and scintillation positions, for different lightguide thicknesses (from **Top** to **Bottom**): 0.00 mm, 0.50 mm, 1.00 mm, and 1.50 mm. **Left**: in X axis; **Right**: in Y axis. Note the scale reduction, from 1 to 0.6, when comparing to previous figures.

| Position | | Offset | | FWHM | |
|---|---|---|---|---|---|
| X/mm | Y/mm | X/mm | Y/mm | X/mm | Y/mm |
| 0.00 | 0.00 | −0.0144 | −0.0114 | 0.4813 | 0.4422 |
| 2.00 | 0.00 | +0.1192 | −0.0189 | 0.7017 | 0.3715 |
| 2.00 | 2.00 | +0.1051 | +0.1406 | 0.5683 | 0.6087 |
| 4.00 | 0.00 | +0.0502 | −0.0246 | 0.5440 | 0.3483 |
| 8.00 | 8.00 | −0.0403 | −0.0289 | 0.3402 | 0.3211 |
| 8.00 | 10.00 | −0.0525 | −0.0890 | 0.3323 | 0.3754 |
| 8.00 | 12.00 | −0.0248 | −0.1231 | 0.3752 | 0.5329 |

Table 6.15: Resolution of the detector with scintillator and lightguide covered in optical grease, with a PTFE backplate, for a 0.5 mm lightguide.

| Position | | Offset | | FWHM | |
|---|---|---|---|---|---|
| X/mm | Y/mm | X/mm | Y/mm | X/mm | Y/mm |
| 0.00 | 0.00 | −0.0158 | −0.0199 | 0.5801 | 0.5404 |
| 2.00 | 0.00 | +0.0505 | −0.0417 | 0.6742 | 0.4456 |
| 2.00 | 2.00 | +0.0340 | +0.0738 | 0.6462 | 0.6391 |
| 4.00 | 0.00 | +0.0592 | −0.0329 | 0.6178 | 0.4094 |
| 8.00 | 8.00 | −0.0585 | −0.0499 | 0.4058 | 0.3955 |
| 8.00 | 10.00 | −0.0557 | −0.1061 | 0.4043 | 0.4204 |
| 8.00 | 12.00 | −0.0389 | −0.1472 | 0.4497 | 0.5980 |

Table 6.16: Resolution of the detector with scintillator and lightguide covered in optical grease, with a PTFE backplate, for a 1.0 mm lightguide.

| Position | | Offset | | FWHM | |
|---|---|---|---|---|---|
| X/mm | Y/mm | X/mm | Y/mm | X/mm | Y/mm |
| 0.00 | 0.00 | −0.0349 | −0.0338 | 0.6757 | 0.6546 |
| 2.00 | 0.00 | −0.0085 | −0.0460 | 0.7377 | 0.5303 |
| 2.00 | 2.00 | −0.0194 | +0.0020 | 0.6604 | 0.6870 |
| 4.00 | 0.00 | +0.0279 | −0.0575 | 0.7176 | 0.4948 |
| 8.00 | 8.00 | −0.0529 | −0.0481 | 0.4638 | 0.4685 |
| 8.00 | 10.00 | −0.0638 | −0.1135 | 0.4874 | 0.5104 |
| 8.00 | 12.00 | −0.0273 | −0.1727 | 0.5459 | 0.7209 |

Table 6.17: Resolution of the detector with scintillator and lightguide covered in optical grease, with a PTFE backplate, for a 1.5 mm lightguide.

## 6.6 Summary

Previous sections show how considerations on the physics inside the detector, along with analysis of LRFs, may give helpful insight on how to improve the detector. The optimization expectations given by such insights were confirmed by means of simulations.

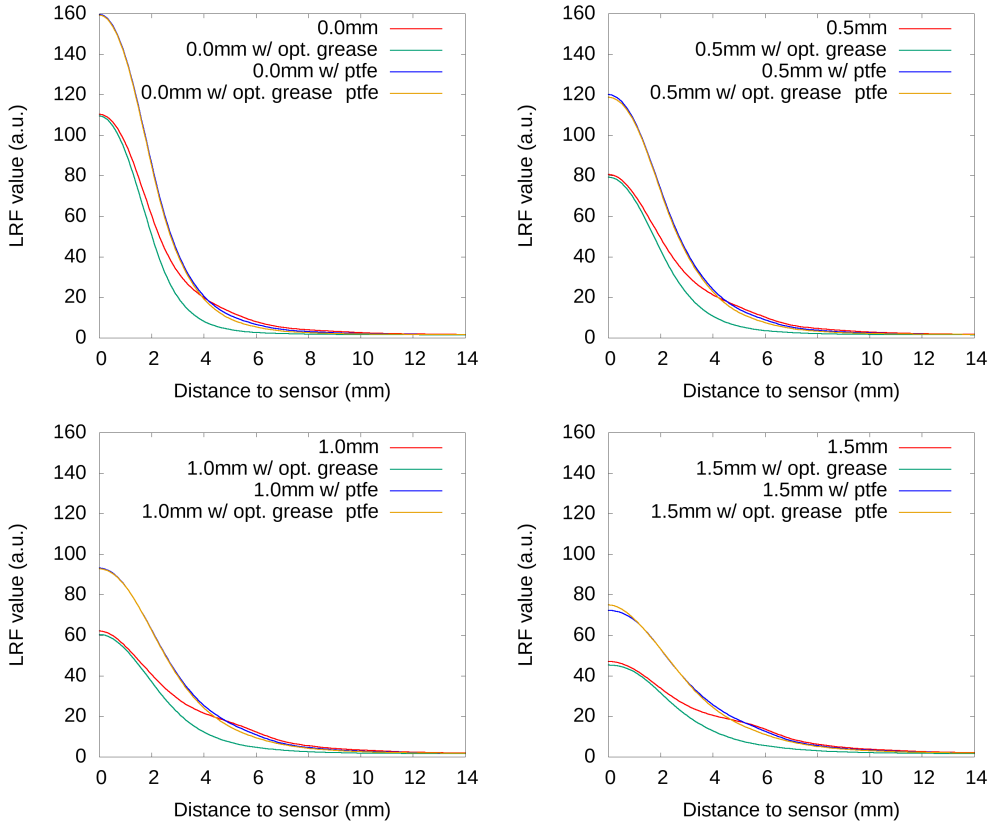


Figure 6.21: LRFs of SiPM #14 for detectors with lightguide thickness of: **Left**: 0.0 mm; **Right**: 1.0 mm.

Figure 6.21 presents a comparison of the LRF of sensor #14 for the studied models.

It was shown that the choice of the lightguide thickness is important for the detector performance. Reducing full internal reflections inside the scintillator, while returning part of the light escaping the lower side of the crystal, by means of a diffuse reflector, greatly improves spatial resolution and useful field of view, as well as significantly reduces distortions.

For this case, inserting the PTFE backplate, covering the detector with optical grease, and using a lightguide with 0.5 mm thickness produced the best results, with a **resolution** of 0.5 mm, and a **useful field of view** of 28 mm × 28 mm.

# Chapter 7

# Conclusions

In the course of my master studies I have developed a detailed model of the compact gamma camera using the ANTS2 simulation package. The predictive power of this model was demonstrated by simulating a prototype of the camera which was already built: the simulated and the corresponding experimental results (both the LRFs of the photosensors and the reconstructed images) were very similar.

Then, an optimization study was performed on the lightguide thickness for several configurations. I have found the optimal configuration of the detector to have a diffuse reflector coupled to the back plane of the scintillator. It was also shown that it is beneficial to cover the side walls of the scintillator and the lightguide with optical grease and a light absorbing layer. For this configuration, the optimal thickness of the lightguide was found to be 0.5 mm. The optimized camera spatial resolution was shown to be close to 0.5 mm, the maximum position reconstruction bias of 0.5 mm and the useful field of view of 28 mm × 28 mm (87 % of the crystal area).

As an unexpected side-result of the study was a demonstration of a surprisingly accurate reconstruction of the experimental event positions using the LRFs calculated from simulation data. We are currently considering a possibility to prepare a publication dedicated to this fact.

Besides the comparison and the optimization study reported here, I have also made the following contributions to the work of the group:

- Introduced the first scripting tool in ANTS2.
- Developed a complete set of optimization scripts, which simplify, and in some cases even allow fully automatic optimization of the detector geometry. Note that these scripts will be very useful in future optimizations of the detector.
- Converted the simulation module of ANTS2 to be able to run in the multi-threaded mode, which significantly reduced the time needed for the simulations (by a factor of four on a computer with Intel i7 4770K CPU).

In previous work, performed as a research student, I have contributed to the experimental branch, by writing the data acquisition software (LULAS), and implementing an automatic gain equalization algorithm, which is optimized for uniformity.

I have also contributed to three publications: [20], [21], and [24].

# Appendix A

# Script to generate simulation data used in model validation

```
function merge()
{
    var merged = {}
    var args = arguments
    if(args.length == 1 && Array.isArray(args[0]))
        args = args[0]
    for(var i = 0; i < args.length; i++)
    {
        var obj = args[i]
        if(Array.isArray(obj)) {
            obj.unshift(merged)
            merged = merge(obj)
        } else {
            for(var key in obj)
                merged[key] = obj[key]
        }
    }
    return merged
}

config.Merge = function(key) {
    var args = Array.prototype.slice.call(arguments, config.Merge.length);
    config.Replace(key, merge(config.GetKeyValue(key), args))
}

function Transform(angle, xoff, yoff) {
    var c = math.cos(angle)
    var s = math.sin(angle)
    return function(x, y) { return {x: xoff + c*x + s*y, y: yoff - s*x +
 ↪  c*y } }
}

function forEachWorldElement(predicate, callback) {
    var tree = config.GetKeyValue(".WorldTree")

    function recurser(container) {
```

```
        for(var i in tree) {
            if(tree[i].Name == container) {
                if(callback(tree[i], i, tree) && tree[i].Container != "")
                    recurser(tree[i].Container)
            }
        }
    }

    for(var i in tree) {
        var pred = predicate === undefined ? true : predicate(tree[i], i,
 ↪  tree)
        if((pred.sel === undefined && pred) || pred.sel) {
            if(callback(tree[i], i, tree))
                recurser(tree[i].Container)
        }
    }

    config.Replace(".WorldTree", tree)
}

function MatchName(name) { return function(el) { return
 ↪  el.Name.indexOf(name) >= 0 } }
function ActivateElement(enable, recursive) {
    return function(el) { el.fActive = enable ? true : false; return
 ↪  recursive }
}

function RunSim(saveName, overwrite) {
    if(!overwrite && core.isFileExists(saveName)) {
        core.print("File '"+saveName+"' already exists.")
        return false
    }

    config.UpdateAllConfig()
    if(!sim.RunParticleSources()) {
        core.print("Failed to run simulate ParticleSources for file
 ↪  "+saveName)
        return false
    }
    sim.SaveAsTree(saveName)
    return true
}

var Grid = (function () {
    var cls = function(xlim, ylim, point) {
        this.forEach = function(callback) {
            for(var xi = xlim.min; xi < xlim.max; xi++)
                for(var yi = ylim.min; yi < ylim.max; yi++) {
                    callback(point(xi, yi), { xi:xi, yi:yi,
 ↪  name:"XY_"+xi*12+"X_"+yi*12+"Y" })
                }
```

```
        }
    };

    cls.prototype = {
        manifest: function(fileName, header) {
            core.deleteFile(fileName)
            core.createFile(fileName)
            for(var h in header)
                core.save(fileName, "#"+h+" "+header[h]+"\n")
            this.forEach(function(pos, args) {
                core.save(fileName, "FastScan"+args.name+"_10kevt.dat
↪   "+pos.x+" "+pos.y+"\n")
            })
        },
        simulate: function(savePath, kevt, overwrite) {
            if(!kevt) kevt = 10
            config.Replace(".ParticleSourcesConfig..EventsToDo",
↪   kevt*1000)
            config.Merge(source99mTc, { Z:-100, Spread:1 })
            forEachWorldElement(MatchName("Hole"), ActivateElement(true,
↪   true))

            this.forEach(function(pos, args) {
                var fileName = savePath+args.name+"_"+kevt+"kevt.root"
                if(!overwrite && core.isFileExists(fileName)) return

                forEachWorldElement(MatchName("Hole"),
↪   function(el){el.X=pos.x;el.Y=pos.y})
                config.Merge(source99mTc, { X: pos.x, Y: pos.y })

                core.print("Simulating grid point ("+pos.x+"; "+pos.y+")")
                RunSim(fileName)
            })

            forEachWorldElement(MatchName("Hole"), ActivateElement(false,
↪   true))
        }
    };

    return cls;
})()

function simFGS(savePath) {
    core.print("Running simulations for "+savePath)
    core.createDir(savePath)
    var kevt = { flood: 500, slit: 400, grid: 10 }
    var sim_gains = Array(pms.CountPM())
    var fForceRedo = false
    var lrf_opts = {Nodes_x:10, UseGroupping:false, DataSelector:0,
↪   LRF_type:0, LRF_3D:false,
```

```
        UseGrid:true, UseEnergy:true, ForceZeroDeriv:true,
↪   StoreError:false,
        Compression_k:5, Compression_r0:7, Compression_lam:6 }

    config.Replace(".FilterOptions", {})

    function getFilenames(postfix) {
        var postfixflood = postfix+"_"+kevt.flood+"kevt"
        return { flood: savePath+"flood"+postfixflood+".root",
            lrfs: savePath+"lrfs"+postfixflood+".json",
            gains: savePath+"gains"+postfixflood+".dat",
            slit: savePath+"slit"+postfix+"_"+kevt.slit+"kevt.root",
            grid: function(gridname) { return
↪   savePath+gridname+postfix+"/" }
        }
    }

    function doSim(files) {
        if(fForceRedo || !core.isFileExists(files.slit)) {
            config.Replace(".ParticleSourcesConfig..EventsToDo",
↪   kevt.slit*1000)
            config.Merge(source99mTc, {X:0, Y:0, Z:-150, Spread:15})
            forEachWorldElement(MatchName("Slit"), ActivateElement(true,
↪   true))
            RunSim(files.slit)
            forEachWorldElement(MatchName("Slit"), ActivateElement(false,
↪   true))
        }

        for(var g in grids) {
            var dirname = files.grid(g)
            core.createDir(dirname)
            grids[g].simulate(dirname, kevt.grid, fForceRedo)
        }

        config.Replace(".ParticleSourcesConfig..EventsToDo",
↪   kevt.flood*1000)
        config.Merge(source99mTc, {X:0, Y:0, Z:-1000, Spread:1})

        if(fForceRedo || !core.isFileExists(files.flood)) {
            if(!RunSim(files.flood))
                return false
            fForceRedo = true
        } else events.LoadEventsTree(files.flood)

        if(fForceRedo || !core.isFileExists(files.lrfs)) {
            var msg = lrf.Make(lrf_opts)
            if(msg != "") {
                core.print("lrf.Make failed: "+msg)
                return false
            }
```

```
            lrf.Save(files.lrfs)
            fForceRedo = true
        } else lrf.Load(files.lrfs)

        if(fForceRedo || !core.isFileExists(files.gains)) {
            core.deleteFile(files.gains)
            core.createFile(files.gains)
            for(var i = 0; i < pms.CountPM(); i++) {
                lrf.ShowVsXY(i)
                var g = grwin.GetAxis().maxZ
                core.save(files.gains, g+"\n")
                sim_gains[i] = g
            }
        } else sim_gains = core.loadColumn(files.gains)
        return true
    }

    var files = getFilenames("")
    if(!doSim(files)) {
        core.print("Fatal error, not doing "+savePath+" anymore.")
        return false
    }

    core.print("Running simulations for "+savePath+" with fixed gains")

    var max = 0
    for(var i = 0; i < pms.CountPM(); i++) {
        sim_gains[i] = exp_gains[i] / sim_gains[i]
        if(sim_gains[i] > max) max = sim_gains[i]
    }
    for(var i = 0; i < pms.CountPM(); i++) config.SetElGain(i,
↪   sim_gains[i] / max)

    doSim(getFilenames("_gainfix"))
}

var grids = {
    //-14.45217897, -13.24204514  0.67582642  (+2.1, +2.1)
    grid: new Grid({ min:0, max:14 }, { min:0, max:14 }, (function() {
        var t = Transform(0.59 * math.pi/180, 12.73, -13.54)
        return function(xi, yi) { return t(-2.1*xi, +2.1*yi) }
    })()),
    //(13 -> -14.3, -13.4 -> 13.9) 0.0°
    /*grid0: new Grid({ min:0, max:14 }, { min:0, max:14 }, (function() {
        var t = Transform(0, 13.0, -13.4)
        return function(xi, yi) { return t(-2.1*xi, +2.1*yi) }
    })())*/
}

var rootPath = "/home/raimundo/projects/masterthesis/11 experimental
↪   compare/"
```

```
//var rootPath = "C:/Users/raimundo/projects/masterthesis/11 experimental
 ↪  compare/"

//grids.grid.manifest(rootPath+"manifest_fixed.txt", { type: "hole",
 ↪  Diameter: 1.0 })

var exp_gains = core.loadColumn(rootPath+"exp_raw_gains.dat")
config.Load(rootPath+"config.json")

var source99mTc = (function() {
    var sources = config.GetKeyValue(".ParticleSources")
    for(var i in sources) {
        if(sources[i].Name === "99mTc")
            return ".ParticleSources["+i+"]"
    }
    core.abort("Could not find 99mTc source")
})()

config.Load(rootPath+"config.json")
//config.Replace(".WaveResolved", true)
simFGS(rootPath+"ideal/")
/*
config.Load(rootPath+"config.json")
config.Replace(".Slabs[2].height", 1.0)
simFGS(rootPath+"LG10/")

config.Load(rootPath+"config.json")
config.Replace(".Slabs[6].fActive", false)
simFGS(rootPath+"noTeflon/")
*/
```

# Appendix B

# Script to generate simulation data used in optimization

```
function merge()
{
    var merged = {}
    for(var i = 0; i < arguments.length; i++)
    {
        var obj = arguments[i]
        for(key in obj)
            merged[key] = obj[key]
    }
    return merged
}

function setCustomNodes(runs, nodes)
{
  Ants.Config.set("/SimulationConfig", { Mode:"PointSim",
 ↪  PointSourcesConfig: {
        ControlOptions: { Single_Scan_Flood:3, MultipleRunsNumber:runs,
 ↪  MultipleRuns:true, },
        CustomNodesOptions: { Nodes:nodes, NumberNodes:nodes.length },
  }})
}

function setFlood(nodeCount)
{
  Ants.Config.set("/SimulationConfig", { Mode:"PointSim",
 ↪  PointSourcesConfig: {
        ControlOptions: { Single_Scan_Flood:2, MultipleRuns:false, },
        FloodOptions: { Nodes:nodeCount, Shape:0,
            Xfrom: -15,      Xto: 15,
            Yfrom: -15,      Yto: 15,
            Zfrom: -0.99,    Zto: 0.99, Zoption: 1,
        },
  }})
}
```

```
Lrf = {

    Nodes : function(nodes) {
        var nod = {}
             if('x' in nodes) nod.Nodes_x = nodes.x
        else if('r' in nodes) nod.Nodes_x = nodes.r
             if('y' in nodes) nod.Nodes_y = nodes.y
        else if('z' in nodes) nod.Nodes_y = nodes.z
        return nod
    },

    Type : {
        Axial     : { LRF_type : 0, LRF_3D : false },
        XY        : { LRF_type : 1, LRF_3D : false },
        Polar     : { LRF_type : 2, LRF_3D : false },
        Composite : { LRF_type : 3, LRF_3D : false },
        AxialZ    : { LRF_type : 0, LRF_3D : true  },
        XYZ       : { LRF_type : 1, LRF_3D : true  },
    },
    //Default: Simulation
    Source : {
        Simulation     : { DataSelector : 0 },
        Reconstruction : { DataSelector : 1 }
    },
    //Default: Individual
    Group : {
        Individual : { UseGroupping : false,
↪   GroupingOption : "Individual" },
        Common     : { UseGroupping : true,  GrouppingType : 0,
↪   GroupingOption : "One LRF for all PMs" },
        Radial     : { UseGroupping : true,  GrouppingType : 1,
↪   GroupingOption : "Group PMs by radius from center" },
        SquarePack : { UseGroupping : true,  GrouppingType : 2,
↪   GroupingOption : "Assume square packing" },
        HexPack    : { UseGroupping : true,  GrouppingType : 3,
↪   GroupingOption : "Assume hexagonal packing" },
    },
    //Default: No Compression
    Compression : function(compression) {
        if(typeof compression == "undefined")
            return { LRF_compress : false }
        else if(Object.prototype.toString.call(compression) === "[object
↪   Array]")
            return { LRF_compress : true,
                Compression_k   : compression[0],
                Compression_r0  : compression[1],
                Compression_lam : compression[2],
            }
        else
            return { LRF_compress : true,
                Compression_k   : compression.k,
```

```
                Compression_r0  : compression.r0,
                Compression_lam : compression.lam,
            }
    },
}

Lrf.Default = merge(
    {
        ANTS2build   : 1105,
        StoreError : false,
        UseGrid : true,
        UseEnergy : true,
        AdjustGains : true,
    },
    Lrf.Source.Simulation,
    Lrf.Group.Individual,
    Lrf.Compression() )

var lrfConfig = {
//    "cAxial" : merge( Lrf.Default, Lrf.Nodes({r : 8         }),
 ↪  Lrf.Group.SquarePack, Lrf.Type.Axial, Lrf.Compression([50, 8, 3]) ),
    "Axial"  : merge( Lrf.Default, Lrf.Nodes({r : 30        }),
 ↪  Lrf.Group.SquarePack, Lrf.Type.Axial),
//    "xy13"   : merge( Lrf.Default, Lrf.Nodes({x : 13, y : 13}),
 ↪  Lrf.Group.Individual, Lrf.Type.XY ),
}

gridNodes = []
for(var z = -0.9; z <= 0.9; z += 0.45)
    for(var x = .0; x <= 14.0; x += 2)
        for(var y = .0; y <= 14.0; y += 2)
            gridNodes.push([x, y, z])

//Ants.setSaveSimWithRecon(false)
Config.loadFile("config.json")
//Config.set("/SimulationConfig", { Mode:"SourceSim" })
Config.set("/SimulationConfig/PointSourcesConfig/PhotPerNodeOptions/PhotPerNodeConstant",
 ↪  3500)

function optimLg(namenote, lgts)
{
    for(lgt in lgts)
    {
        var basename = lgt+"mm-"+namenote

        var layers =
 ↪  JSON.parse(Ants.Config.get("/DetectorConfig/SandwichSettings/Layers"))
        layers[2].Active = lgts[lgt] != 0.0
        layers[2].Height = lgts[lgt]
        Ants.Config.set("/DetectorConfig/SandwichSettings/Layers", layers)
```

```
        setFlood(100000)
        for(var i = 0; i < 10; i++)
        {
            Ants.simulate(8)
            saveSimulation("flood/"+basename+" 100k-0"+i+".root")
        }
        Ants.clearEvents()

        for(var i = 0; i < 10; i++)
            loadSimulation("flood/"+basename+" 100k-0"+i+".root")

        for(lrf in lrfConfig)
        {
            makeLRFs(lrfConfig[lrf])
            saveLRFs("lrfs/"+basename+" "+lrf+".json", 0)
            if(Ants.reconstruct() === true)
                saveReconstruction("flood/"+basename+" "+lrf+".root")
        }

        setCustomNodes(1000, gridNodes)
        Ants.simulate(8)
        saveSimulation("grid/"+basename+".root")
        for(lrf in lrfConfig)
        {
            loadLRFs("lrfs/"+basename+" "+lrf+".json")
            if(Ants.reconstruct() === true)
                saveReconstruction("grid/"+basename+" "+lrf+".root")
        }
    }
}

var thicknesses = {
    "0.00" :  0.00,
    "0.25" :  0.25,
    "0.50" :  0.50,
    "0.75" :  0.75,
    "1.00" :  1.00,
    "1.50" :  1.50,
    "2.00" :  2.00,
}

//Teflon layers
//var layers =
 ↪  JSON.parse(Ants.Config.get("/DetectorConfig/SandwichSettings/Layers"))
//layers[6] = { "Active": true, "Angle": 0, "Height": 0.1, "Material": 4,
 ↪  "Shape": 0, "Sides": 6, "Size1": 30, "Size2": 30 }
//layers[7] = { "Active": true, "Angle": 0, "Height": 0.5, "Material": 8,
 ↪  "Shape": 0, "Sides": 6, "Size1": 30, "Size2": 30 }
//Ants.Config.set("/DetectorConfig/SandwichSettings/Layers", layers)
```

```
Config.set("/SimulationConfig/GeneralSimConfig/WaveConfig/WaveResolved",
 ↪  true)
optimLg("wave", { "0.00" : 0.00, "1.00" : 1.00, })
Config.set("/SimulationConfig/GeneralSimConfig/WaveConfig/WaveResolved",
 ↪  false)
optimLg("noWave", thicknesses)
```

# Bibliography


[1] Optical constants of $(C_5O_2H_8)_n$ (Poly(methyl methacrylate), PMMA). http://refractiveindex.info/?shelf=organic&book=poly%28methyl_methacrylate%29&page=Sultanova. [Online; accessed 20-Jun-2016].

[2] Ants2 source code and user manual. http://coimbra.lip.pt/ants/ants2.html. [Online; accessed 15-Jun-2016].

[3] M. J. Berger, J. H. Hubbell, S. M. Seltzer, J. Chang, J. S. Coursey, R. Sukumar, D. Zucker, and K. Olsen. Xcom: Photon cross sections database (version 1.5). http://physics.nist.gov/xcom, 2010. [Online; accessed 15-Jun-2016].

[4] R. Brun and F. Rademakers. Root - an object oriented data analysis framework. *Nucl. Intrum. Methods*, 389:81, 1997.

[5] ROOT manual: Geometry package. https://root.cern.ch/root/htmldoc/guides/users-guide/ROOTUsersGuide.html#the-geometry-package. [Online; accessed 15-Jun-2016].

[6] R. Chytracek, J. Mccormick, W. Pokorski, and G. Santin. Geometry description markup language for physics simulation and analysis applications. *IEEE Transactions on Nuclear Science*, 53(5):2892–2896, Oct 2006. See also GDML user's guide: http://gdml.web.cern.ch/GDML/doc/GDMLmanual.pdf.

[7] C. L. Corkhill et al. Real-time gamma imaging of technetium transport through natural and engineered porous materials for radioactive waste disposal. *Environ. Sci. Technol.*, 47(23):13857–13864, 2013.

[8] C. M. Davisson. *Interactions of gamma-radiation with matter*. North-Holland Publishing Company, 1965.

[9] D. Ding, J. Yang, G. Ren, M. Nikl, S. Wang, Y. Wu, and Z. Mao. Effects of anisotropy on structural and optical characteristics of LYSO:Ce crystal. *Physica Status Solidi (B)*, 251(6):1202–1211, 2014.

[10] General properties of LYSO(Ce) scintillator. http://www.epic-crystal.com/shop_reviews/lyso-scintillator/. [Online; accessed 20-Jun-2016].

[11] G. Erdei, N. Berze, Ágnes Péter, B. Játékos, and E. Lorincz. Refractive index measurement of cerium-doped $Lu_xY_{2-x}SiO_5$ single crystal. *Optical Materials*, 34:781–785, 2012.

[12] R. M. Gray and A. Macovski. Maximum a posteriori estimation of position in scintillation cameras. *IEEE Transactions on Nuclear Science*, 23:849–852, Feb 1976.

[13] E. Hecht. *Optics*. Adelphi University, 4th edition, 2003.

[14] J. Y. Hesterman, L. Caucci, M. A. Kupinski, H. H. Barrett, and L. R. Furenlid. Maximum-likelihood estimation with a contracting-grid search algorithm. *IEEE Transactions on Nuclear Science*, 57(3):1077–1084, Jun 2010.

[15] G. F. Knoll. *Radiation Detection and Measurements*. John Wiley and Sons, 2000.

[16] W. R. Leo. *Techniques for Nuclear and Particle Physics Experiments*. Springer, 1994.

[17] A. B. Makokha, M. H. Moys, and M. D. T. Vangu. Application of gamma emission imaging in mineral processing industry: case study of slurry transport in a wet laboratory ball mill. *Measurement Science and Technology*, 22(4):045706, 2011.

[18] R. Mao, L. Zhang, and R.-Y. Zhu. Emission spectra of LSO and LYSO crystals excited by uv light, x-ray and $\gamma$-ray. *IEEE Transactions on Nuclear Science*, 55(3), Jun 2008.

[19] L. Moneta and F. James. Minuit2 minimization package, 2010.

[20] A. Morozov, V. Solovov, F. Alves, V. Domingos, R. Martins, F. Neves, and V. Chepel. Iterative reconstruction of detector response of an anger gamma camera. *Physics of Medicine and Biology*, 60:4169–4184, 2015.

[21] A. Morozov, V. Solovov, R. Martins, F. Neves, V. Domingos, and V. Chepel. Ants2 package: simulation and experimental data processing for anger camera type detectors. *Journal of Instrumentation*, 11:P04022, 2016.

[22] M. Moszyński et al. Energy resolution of scintillation detectors. *Nucl. Instrum. Meth. A*, 805:25–35, Jan 2016.

[23] B-series fast, blue-sensitive silicon photomultiplier sensors datasheet. `http://www.sensl.com/downloads/ds/DS-MicroBseries.pdf`. [Online; accessed 20-Jun-2016].

[24] V. Solovov, A. Morozov, V. Chepel, V. Domingos, and R. Martins. B-spline parameterization of spatial response in a monolithic scintillation camera. 2016.

[25] V. N. Solovov et al. Position reconstruction in a dual phase xenon scintillation detector. *IEEE Transactions on Nuclear Science*, 59(6):3286–3293, Dec 2012.

[26] E. Storm and H. I. Israel. Photon cross sections from 1 keV to 100 MeV for elements $Z = 1$ to $Z = 100$. *Atomic Data and Nuclear Data Tables*, 5(6):565–688, 1970.

[27] N. Sultanova, S. Kasarova, and I. Nikolov. Dispersion properties of optical polymers. *Acta Physica Polonica A*, 116:585–587, 2009.

[28] R. J. Wilson. Collimator technology and advancements. *J. Nucl. Med. Technol.*, 16:198–203, 1988.